ABSTRACT

Title of Dissertation:	FABRICATION AND CHARACTERIZATION OF PEROVSKITE SOLAR CELL AND CHALLENGES TO THE INTERMEDIATE BAND CONCEPT IN INAS/GAAS QUANTUM DOT SOLAR CELL
	Yangyi Yao, Doctor of Philosophy, 2019
Dissertation Directed By:	Professor Mario Dagenais, Department of Electrical and Computer Engineering

Metal-organic perovskite materials have outstanding properties in photovoltaic applications, the perovskite based solar cells have already demonstrated remarkable power conversion efficiency enhancement from 3.8% in 2009 to 23.7% in late 2018. In our work, we focused on the simple PTAA-based planar perovskite solar cell without using a complicated surface passivation technique. We proposed a sequential method to dope the PTAA thin film in order to reduce the solar cell's series resistance. We also modified the inter-diffusion method to grow high quality perovskite thin film, we can easily grow the perovskite thin film layer with thicknesses over 400 nm and grain sizes over 2 μm. Compared to our conventional PEDOT:PSS-based perovskite solar cell, we observed an improvement in both the open-circuit-voltage and the short-circuit-current, resulting in a power conversion efficiency enhancement from 12.7% to 15.3%. Other applications of perovskite

material such as perovskite-based tandem cell and perovskite-based laser cavity are also investigated.

The concept of intermediate band solar cell was proposed by Luque and Marti in 1990 and has been extensively studied for decades. Previously we have reported high optical saturation intensity of the quantum dot resonance at room temperature for a self-ensemble of un-doped quantum dots (QDs). Operating at cryogenic temperatures leads to a reduction of the saturation intensity. We acquired a liquid-helium cryo-cooler system to support the on-resonance measurement of the quantum dot solar cell (QDSC) at cryogenic temperatures. We measured the photoluminescence of the QDSC to extract the QD energy from 293K to 8K. We modified the on-resonance z-scan set-up with the cryo-cooler to evaluate the saturation effects of the QDs. We studied the photocurrent response and extracted the saturation intensity of the QD ground state from 293K to 170K. We observed a substantial decrease of the saturation intensity as the temperature is decreased, but this intensity is still much higher than one-sun intensity. The intermediate band two photon absorption contribution to the photocurrent enhancement is extremely small even at 170K. By cooling all the way down to liquid helium temperature, it should be possible to further reduce the saturation intensity.

FABRICATION AND CHARACTERIZATION OF PEROVSKITE SOLAR CELL AND CHALLENGES TO THE INTERMEDIATE BAND CONCEPT IN INAS/GAAS QUANTUM DOT SOLAR CELL

by

Yangyi Yao

Dissertation submitted to the Faculty of the Graduate School of the
University of Maryland, College Park, in partial fulfillment
of the requirements for the degree of
Doctor of Philosophy
2019

Advisory Committee:
Professor Mario Dagenais, Chair
Professor Edo Waks,
Professor Martin Peckerar,
Assistant Professor Kevin Daniels
Assistant Professor Marina Leite
Professor Lourdes G. Salamanca-Riba

Acknowledgements

Pursuing a PhD degree is a long journey filled with difficulties, challenges, and struggles as well as joy, sense of fulfillment and satisfactory. This unforgettable experience has taught me how to toughly face challenges and technically solve problems, how to efficiently coordinate teams and effectively realize goals. Here, I would like to give my greatest appreciation to my advisor, Prof. Mario Dagenais, for his thorough guidance and constant motivation to my research work and for having the right attitude towards life. He brought me into the real scientific world and showed me the path to be a professional researcher.

I am grateful to the members of my dissertation committees for their time and supports, namely Prof. Mario Dagenais, Prof. Edo Waks, Prof. Martin Peckerar, Prof. Kevin Daniels, Prof. Marina Leite and Prof. Lourdes G. Salamanca-Riba.

I would like to thank the engineers in the Fablab for their supports and guidance in the fabrication and characterization of precious samples in the clean room, namely Tom Loughran, John Abrahams, Jonathan A. Hummel, Mark Lecates and Jim O'Connor. And, I would like to give my appreciation to the staff in the Aimlab and Surface Analyze Center for their guidance with SEM and AFM, namely Prof. Wen-An Chiou, Dr Sz-Chian Liou and Dr Karen Gaskell.

And last, I'm extremely grateful to my beloved family who has always supported and encouraged me in my endeavors and challengers.

Table of Contents

List of Tables

List of Figure

List of Publications

- Y. Yao, M. Dagenais "Intermediate Band Challenge in InAs/GaAs Quantum Dot Solar Cell at Cryogenic Temperatures", 46th IEEE Photovoltaic Specialist Conference, 2019, Accepted.
- Y. Yao, W. Hsu, M. Dagenais "High Efficiency Perovskite Solar Cells with Sequentially Doped PTAA", IEEE Journal of Photovoltaics, 2019, Accepted.
- Y. Yao, W. Hsu, M. Dagenais "High Efficiency Perovskite Solar Cells by a Modified Low-Temperature Solution Process Inter-Diffusion Method", 44th IEEE Photovoltaic Specialist Conference, 2017.
- Y. Liang, Y. Yao, M. Dagenais and I. Takeuchi, "Fabrication of organic-inorganic perovskite thin films for planar solar cells via pulsed laser deposition", AIP Advances, vol. 6, no. 1, p. 015001, 2016.
- Y. Yao, W. Hsu, M. Dagenais, Entrepreneurship Award on 2016 NanoDay Conference Poster Presentation in University of Maryland

Chapter 1 Abstract and Dissertation Outline

1. 1 Abstract

Metal-organic perovskite materials have outstanding properties in photovoltaic applications, such as long diffusion length, large carrier mobility, tunable bandgap and low-temperature solution process-ability. Perovskite based solar cells have already demonstrated remarkable power conversion efficiency (PCE) enhancement from 3.8% in 2009 to 23.7% in late 2018. In our work, we first modified the inter-diffusion growth method to grow high quality perovskite thin films. In this modified approach, we can easily grow the perovskite thin film layer with thicknesses over 400 nm and grain sizes over 2 μm by the controlled solvent-assist annealing (SAA) technique. We used an inverted solar cell planar structure and selected PEDOT:PSS as the hole-transport material (HTM) at the beginning. Then we focused on the simple PTAA-based planar perovskite solar cell without using a complicated surface passivation technique. We proposed a sequential method to dope the PTAA thin film in order to reduce the solar cell's series resistance. The impact of PTAA's doping concentration on the solar cell's PV performance is investigated. The I-V measurements of the solar cell under 1 sun illumination was conducted to test the performance of the solar cell. The external quantum efficiency (EQE) measurements were performed to investigate the spectral photo-current contribution. The surface and cross-section SEM images of the solar cell device demonstrated the high quality of the grown perovskite films and of the interfaces.

Hysteresis effect of the perovskite solar cell in the I-V characteristics was observed. We were able to significantly reduce it by optimizing the perovskite film quality and by selecting the appropriate electron transport material (ETM). Compared to our conventional PEDOT:PSS based perovskite solar cell, we observed an improvement in both the open-circuit-voltage (V_{oc}) and the short-circuit current (J_{sc}), resulting in a power conversion efficiency enhancement from 12.7% to 15.3%. Further work on realizing the tandem perovskite-CIS solar cell is in process. The aim is to achieve the monolithic integration of perovskite with CIS structure and produce a PCE approaching 30%. Other application of perovskite material such as perovskite-based laser cavity was also investigated. Photoluminescence (PL) measurement of the perovskite thin film was performed and showed a strong spontaneous emission peak around 780 nm. We proposed a Fabry-Perot cavity comprising of a gain medium of perovskite layer and a protecting layer of PMMA and a spacing layer of SiO_2 between a high reflectivity dielectric mirror and a silver metal mirror. A pulsed laser optical pumping configuration was used to minimize thermal effect in the gain material.

Another topic of this thesis is the study of the intermediate band challenges in InAs/GaAs quantum dot solar cell (QDSC) at cryogenic temperatures. Previously we have reported high optical saturation intensity of the quantum dot resonance at room temperature for an ensemble of un-doped quantum dots (QDs). We have proposed a physical model to explain the non-linearity of the light-generated-current under resonant excitation from the valence band to the intermediate band. It was shown to be made up of two components: a background two-photon absorption (2PA) term and a resonant optical saturation term. It is argued that the solar intensity is much lower than

the saturation intensities involved for the first and second transition in the intermediate band solar cell under 1-sun illumination and therefore prevent exciting an appreciable amount of population in the terminal level that can be ionized to the continuum. Operating at cryogenic temperatures leads to a reduction of the saturation intensity but it might not be sufficient for increasing the energy conversion efficiency, unless concentrated sun light, and/or high density of quantum dots and/or quantum dots with a lifetime more comparable to the radiative lifetime, are used. We acquired a closed-cycle liquid-helium cryo-cooler system to support the on-resonance photocurrent measurement of the InAs/GaAs QDSC at cryogenic temperatures. In order to determine the on-resonance excitation energy of our QDSC system, we measured the temperature dependent PL of the QDSC to extract the QD energy at various temperatures from 293K to 8K. We modified the z-scan set-up with the cryo-cooler to measure the on-resonance photocurrent versus temperature to evaluate the saturation effects of the quantum dots. We studied the photocurrent response and extracted the saturation intensity of the QD ground state (GS) from room temperature to 170K. We observe a substantial decrease of the saturation intensity as the temperature is decreased, but this intensity is still much higher than one-sun intensity and is about 0.82 times as the sun intensity at maximum concentration at 170K. The intermediate band two photon absorption contribution to the photocurrent enhancement is extremely small even at 170K, even though it has been claimed to be observable under cryogenic temperature. By cooling all the way down to liquid helium temperatures, it should be possible to further reduce the saturation intensity.

1. 2 Dissertation Outline

In my PhD work, I am involved with two projects. One project is the study of perovskite solar cell, the other is related to understanding the potential of intermediate band solar cells based on InAs/GaAs quantum dots. In the first part of Chapter 2, I will introduce the background of the perovskite material in photovoltaic application. I will review some state-of-art perovskite solar cell structures, the interfacing materials and the fabrication techniques. After that, I will summarize my work on the perovskite solar cell fabrication and characterization. In the second part, I will introduce the basic concept of intermediate band solar cell (IBSC), and then focus on the InAs/GaAs quantum dot solar cell since it has been the most practical way to implement IBSC. I will discuss the physical limitation of this system and the key requirement to achieve the intermediate band functionality. Then I will present some previous findings from our group, such as the physical model that explains the non-linearity of the light-generated-current under resonant excitation from the valence band to the intermediate band. I will then summarize my personal work on the PL measurement and on-resonance z-scan measurement at cryogenic temperatures.

In chapter 3, I will demonstrate my work on the project of perovskite solar cell in five sections. In section 3.1, I will overview the perovskite material properties, such as crystal structure and compositions, the tunable bandgap when changing halide ratio, etc. I will also introduce the two dominant structures of perovskite solar cell and their current status. Different growth techniques of perovskite film are also discussed. Then I will demonstrate our proposed method to grow high efficiency perovskite solar cell.

Section 3.2 shows the fabrication details of our perovskite solar cell in 4 subsections. I will list the chemical materials and equipment used in our fabrication process with their vendor information. Then I will demonstrate the fabrication process flow of our perovskite solar cell, I will try to include all the details, tips and tricks in the fabrication procedure. After that I will discuss some key factors for the device optimization. At the end I will summarize the characterization techniques and tools we used on our completed perovskite solar cell.

In Section 3.3, I will demonstrate the main characterization results from the perovskite solar cell, including the solar cell structure, surface and cross-section SEM images, AFM images on the PTAA surface, the solar cell performance dependence on the PTAA's doping level, solvent-assisted annealing condition, and the external quantum efficiency results. Hysteresis effect of perovskite solar cell is also discussed.

Section 3.4 discusses other applications of perovskite material, one is the perovskite-based tandem cell, we propose the design of 4-terminal and monolithic perovskite/CIS tandem solar cell. The other application is the perovskite material based laser cavity. I will show the design and PL results of the perovskite-based laser cavity, the difficulty of realizing the perovskite laser cavity is also discusses. And lastly, section 3.5 summarize the works I've done in the project of perovskite solar cell.

In Chapter 4, I will focus on my second project, the intermediate band solar cell based on InAs/GaAs quantum dots. In section 4.1, I will demonstrate the basic techniques and the process flow for bulk GaAs solar cell fabrication. The final solar cells are electrically isolated with different size mesa-area on the same wafer.

In section 4.2, I will overview some previous findings in our group on the InAs/GaAs quantum dot solar cell. One is the existence of the extended Urbach tail into the quantum dot energy state region, and the derivation of this tail energy from the below-bandgap external quantum efficiency measurement. Another finding is the ultrahigh quantum dot saturation intensity at room temperature extracted from the non-linear photocurrent responses of on-resonance z-scan measurement, which leads to extremely small transition rates between inter-band states.

In section 4.3, I will emphasize my work on the InAs/GaAs quantum dot solar cell. I will introduce the key equipment in my project, the closed-cycle liquid helium cryocooler system. Then I will show the set-up and results of low-temperature photoluminescence measurement, the quantum dot ground state energies at different temperatures are extracted from the PL data. After that, I will demonstrate the modified on-resonance z-scan measurement set-up implementing the cryocooler system, and show the non-linear photocurrent responses from the low temperature measurements. I will also discuss the feasibility of implementing the IBSC model on InAs/GaAs quantum dot solar cell at cryogenic temperature regions. Section 4.4 will briefly summarize the chapter 4.

Based on all the research and experimental works and results I have achieved, I summarize the main findings in Chapter 5. In the project of perovskite, we have proposed the sequential doping method to fabricate PTAA based perovskite solar cell with simple inverted planar structure. A modified inter-diffusion method is adopted to improve the perovskite film quality. Compared to conventional PEDOT:PSS based perovskite solar cell, we observe an improvement in both the open-circuit voltage and

the short-circuit current, resulting in a power conversion efficiency enhancement from 12.7% to 15.3%. In the project of Intermediate band solar cell, a modified on-resonance z-scan measurement technique is used to extract the quantum dot saturation intensity from room temperature to 170K. The saturation intensity is appreciably decrease with temperature but is still 0.83 times as the sun intensity at maximum concentration. This implies that the energy conversion efficiency of this QDSC, even at 170 K, cannot be enhanced by invoking the concept of an intermediate band solar cell.

Chapter 2 Introduction

2. 1 Background on Perovskite Solar Cell and Current Status

Organolmetalic halide perovskite solar cells have already demonstrated remarkable power conversion efficiency (PCE) enhancement from 3.8% [1] in 2009 to 23.7% [2] in late 2018. The active perovskite material has evolved from methylammonium lead iodide to the complex mixed halide compound $(CsI)_x(FAI)_{1-x}PbBr_yI_{1-y}$ following the discovery of improved light absorption and stability when using formamidinium (FA) based perovskite materials [3]. On the other hand, methylammonium (MA) lead halide is still the dominant material being used today in most perovskite solar cell research since their active layer has remarkable properties, such as long carrier diffusion length [4], large carrier mobility [5], tunable band-gap [6] and low-temperature solution processability. Lead-free perovskite materials such as $CH_3NH_3SnI_3$ [7] have recently attracted attention, but the low power conversion efficiency (< 10%) and poor stability are the main challenges for this material. There are two dominant structures for the perovskite solar cell: the meso-porous (n-i-p) structure and the inverted (p-i-n) planar structure. The meso-porous structure usually requires a high-temperature-annealing condensed base layer to minimize the leakage paths from the perovskite layer to the conducting layer [8-11]. Yang et al. from UNIST achieved 22.1% PCE with the conventional TiO_2 based structure in 2017 [11]. On the other hand, the inverted planar perovskite structure simplifies the fabrication procedure without sacrificing too much

the PCE. Recently, Luo et al. reported 21% PCE with an inverted structure using a mixed-cation lead mixed-halide perovskite material [12]. In contrast with the conventional TiO_2 based mesa-porous perovskite structure, there are many candidates for the base hole-transport material (HTM) in an inverted planar structure. Inorganic materials such as NiO_x [13-14] and CuI [15-16] have been considered as the HTM in planar perovskite solar cell. Recently, doped NiO_x has attracted attention, Chen has focused on the doping technique in NiO_x and has reported ~20% PCE using different dopants such as Cu and Cs [17-19]. Compared with inorganic HTMs, organic HTMs are widely adopted for better film coverage and easier control of doping levels. PEDOT:PSS is a popular HTM for its high conductivity and low cost, but its relatively lower work function, which leads to a band mismatch with the perovskite material, usually results in smaller open-circuit voltages (~0.9V) [20-24]. Various organic HTMs have been extensively studied for better band alignment, however many of them are not compatible with the inverted structure. For example, the Spiro-MeOTAD cannot be used as the base HTM because of its high solubility in DMF and DMSO (general solvent for perovskite). It is easy to be washed away when spin-coating a perovskite precursor solution on it. Conducting polymers like poly [N,N'-bis(4-butylphenyl)-N,N'-bis(phenyl)benzidine] (poly-TPD) [25-27] and poly(triaryl amine) (PTAA) [28-30] are good candidates because of their resistance to DMF and DMSO wash. But the non-wetting nature of their surfaces is the main challenge for top perovskite film growth, resulting in poor perovskite film coverage, increased pin-hole density and relatively small perovskite grain size. It has been demonstrated that the perovskite grain size is highly dependent on the hydrophobicity of the bottom layer surface [28], and

that larger grain size can be obtained on better hydrophilic HTM surfaces. Recently there have been several breakthroughs in the conducting polymer HTM studies. Xu et al. have reported that poly-TPD based inverted planar perovskite solar cell can have a PCE exceeding 18% [27]. They resolved the problem of the non-wetting nature of poly-TPD by using ultraviolet-ozone surface modification. Huang et al. have proposed to use doped PTAA thin film as the base HTM to reduce the series resistance and recently they boosted the efficiency from 17.5% [29] to 20.6% [30]. In their approach, PTAA solution is mixed with F4-TCNQ as the doping material and m-MTDATA is used as the surface modification material.

In our study, we focus on the simple PTAA-based planar perovskite solar cell without using a complicated surface passivation technique. We propose a sequential method to dope PTAA in an easier and more stable way. Considering the conventional polymer:F4-TCNQ blend solution, it is observed that this doping material often results in drastically reduced solubility of polymers. As a result of this, the mixed solutions must be kept at high temperature and diluted concentrations to avoid rapid aggregation [31]. In addition, we observe the rapid degradation of F4-TCNQ in a mixed PTAA solution with an obvious color change within a few days, which definitely induces more uncertainties in device performance and solution preparation. To minimize the above-mentioned drawbacks, we propose a sequential method to dope PTAA by exposing PTAA film to the doping solution in an orthogonal solvent system, i.e. toluene for PTAA and 2-propanol for F4-TCNQ. It is found that the PTAA doping level can be tuned by the concentration of the doping solution. This sequential method improves the device's reproducibility and long-term sustainability. In our work, we have also

modified the inter-diffusion method [32] with a controlled solvent-assisted annealing approach to grow high quality perovskite thin film with large grain size (over 2 μm). The optimized recipe guarantees the successful formation of a perovskite layer with average thickness greater than 400 nm without any PbI_2 residue. In this work, we demonstrate a perovskite solar cell with a simple planar structure of FTO/PTAA/$CH_3NH_3PbI_3$/PCBM/Ag and we achieve a champion PCE of 15.3% based on the sequentially doped PTAA thin film without using a complicated surface passivation technique.

2.2 Background on Intermediate Band Solar Cell and Current Status

The world record for the power conversion efficiency (PCE) of a single-junction GaAs solar cell has now reached 29.1% [33], which is close to the Shockley-Queisser limit of 33.5% for a single-junction solar cell under one-sun illumination [34]. To potentially break the fundamental limit, many new concepts have been proposed and one of the most pursued paths has been to utilize nano-scale structures. More than 20 years ago, Luque and Marti have introduced the concept of intermediate band as a way to enhance the conversion efficiency of solar cells beyond the Shockley-Queisser limit [35]. In this approach, another pathway exists for generating additional photocurrent, beyond what can be generated using single junction solar cells. Lower band gap photons can be used to take electrons from the valence band to the intermediate band and then from the intermediate band to the conduction band. The intermediate band solar cell (IBSC) model suggests taking advantage of a two-step absorption within the

forbidden band with two longer wavelength photons so that a larger photocurrent can be generated at the same time maintaining a high open circuit voltage. Lower energy photons can thus be utilized which will reduce the transmission loss. Quickly after, it was suggested that III-V quantum dots (QDs) could form the intermediate band and enhance the efficiency of the single-junction solar cell. In such a system, it is predicted that, the non-concentrator efficiency can be 30.2%. Under concentration, the intermediate band solar cell efficiency in this material system increases to 51.6%, as compared to 36.7% for bulk GaAs solar cells, under a 1000 sun concentration.

The InAs/GaAs QDs are formed in the self-assembled growth mode. During the epitaxial growth of highly strained material, under the Stranski-Krastanov growth mode, three-dimensional islands are formed following the creation of a two-dimensional wetting layer. The resulting strained nanoscale islands are pyramidal in shape. The intermediate level arises from the confined states of the electrons in the potential well created by the conduction band offset between the dot and the matrix material. The intermediate state forms a band due to the overlapping wavefunctions if the quantum dot spacing is 10 nm or less. But severe line dislocations will appear in such high-density quantum dots system that would degrade the device's performance. Consequently, individual energy levels are formed within the quantum dots instead of a band. In this model, one below-bandgap photons will be absorbed and pump the electron from the valence band to the QD ground states and subsequently another below-bandgap photons will functionally pump the electron from the QD ground states to the conduction band. Therefore, an extra path is allowed for an electron to make the transition from the valence band to the conduction band by absorbing two lower energy

photons. The photocurrent should be enhanced, and the voltage given by the conduction and valence band quasi-Fermi levels at the n- and p-contacts, respectively, is expected to stay the same. There is a key requirement for the operation of the IBSC, no extra photocurrent should be detected in the outside circuit from the single photon absorption process acting alone from the valence band to the intermediate band, which is a very difficult condition to realize in practice.

The intermediate band solar cell based on InAs/GaAs and InGaAs/GaAs quantum dots has been extensively studied in the last 20 years [36-38]. However, no one has demonstrated any efficiency enhancement over the optimized single-junction solar cell. The record for an InAs/GaAs quantum dot solar cell (QDSC) is 18.7% [39], which is still far away from 29.1%. Generally, a slightly enhanced photocurrent is observed in QDSC, at the expense of a much lower V_{oc}, which limits the efficiency. Previously we have reported high optical saturation intensity of the quantum dot resonance at room temperature for an ensemble of un-doped quantum dots (QDs). We have proposed a physical model to explain the non-linearity of the light-generated-current under resonant excitation from the valence band to the intermediate band. It was shown to be made up of two components: a background two-photon absorption (2PA) term and a resonant optical saturation term. It was argued that the solar intensity is much lower than the saturation intensities involved for the first and second transition in the intermediate band solar cell under 1-sun illumination and therefore prevent exciting an appreciable amount of population in the terminal level that can be ionized to the continuum. Operating at cryogenic temperatures leads to a reduction of the saturation intensity but it might not be sufficient for increasing the energy conversion efficiency,

unless concentrated sun light, and/or high density of quantum dots and/or quantum dots with a lifetime more comparable to the radiative lifetime, are used. We acquired a closed-cycle liquid-helium cryo-cooler system to support the on-resonance photocurrent measurement of the InAs/GaAs QDSC at cryogenic temperatures. In order to determine the on-resonance excitation energy of our QDSC system, we measured the temperature dependent PL of the QDSC to extract the QD energy at various temperatures from 293K to 8K. We modified the z-scan set-up with the cryo-cooler to measure the on-resonance photocurrent versus temperature to evaluate the saturation effects of the quantum dots. We studied the photocurrent response and extracted the saturation intensity of the QD GS from room temperature to 170K. We observe a substantial decrease of the saturation intensity as the temperature is decreased, but this intensity is still much higher than one-sun intensity and is about 0.82 times as the sun intensity at maximum concentration at 170K. The IB 2PA contribution to the photocurrent enhancement is extremely small even at 170K, even though it has been claimed to be observable under cryogenic temperatures [40]. By cooling all the way down to liquid helium temperatures, it should be possible to further reduce the saturation intensity.

Chapter 3 Project of Perovskite Solar Cell

3. 1 Overview of Perovskite Solar Cell Fabrication Techniques

Organometal halide perovskites have emerged as a very promising material system for high-efficiency nanostructured devices. Within the last few years, the perovskite based solar cells have already demonstrated remarkable power conversion efficiency (PCE) enhancement from 3.8% [1] in 2009 to 23.7% [2] in late 2018. What is remarkable is that such performance has been obtained in solution processed materials at temperatures less than 150^{o}C.

A perovskite is any material with the structure of ABX_3 [41] as shown in the Figure 3.1 (a), which is named after the Russian mineralogist Lev Perovski. In the application of thin film photovoltaic devices, A is a polyatomic organic cation, usually methylammonium ($CH_3NH_3^+$), formamidinium ($HC(NH_2)_2^+$)[14], or tetramethylammonium ($(CH_3)_4N)^+$ ） . Formamidinium (FA) has a slightly larger effective ionic radius as compared to methylammonium (MA) and lead to an expansion of the lattice, a reduction of the bandgap, and a red-shift in the absorption onset. B is a metal cation, usually lead, tin or Ge. X is an anion, typically a halide, either chlorine, bromide, iodine, or some combination of the three. A perovskite structure which incorporates two halides (e.g. iodine with bromide, or bromide with chloride) allows for the continuous tuning of the bandgap and the optical absorption to cover almost the whole visible spectrum [42-43]. Figure 3.1 (b) shows the bandgap tuning curve as a

function of the Br- ratio [43]. Interestingly, no band gap change was observed in the case of iodo-chloride mixed perovskites, possibly indicating the difficulty of integrating Cl into the PbI_6 octahedron. The Ge based perovskites show a lower bandgap than the Sn based perovskites and a lower bandgap than the Pb based perovskites. The perovskite materials have mostly a cubic crystal structure. Most precisely, it was found that $CH_3NH_3PbI_3$ ($MAPbI_3$) goes through a phase transition from orthorhombic to tetragonal at 161.4K and from tetragonal to cubic at 330.4K [44]. The methylammonium ions are fully disordered in the cubic and tetragonal phases, and completely ordered in the orthorhombic phase.

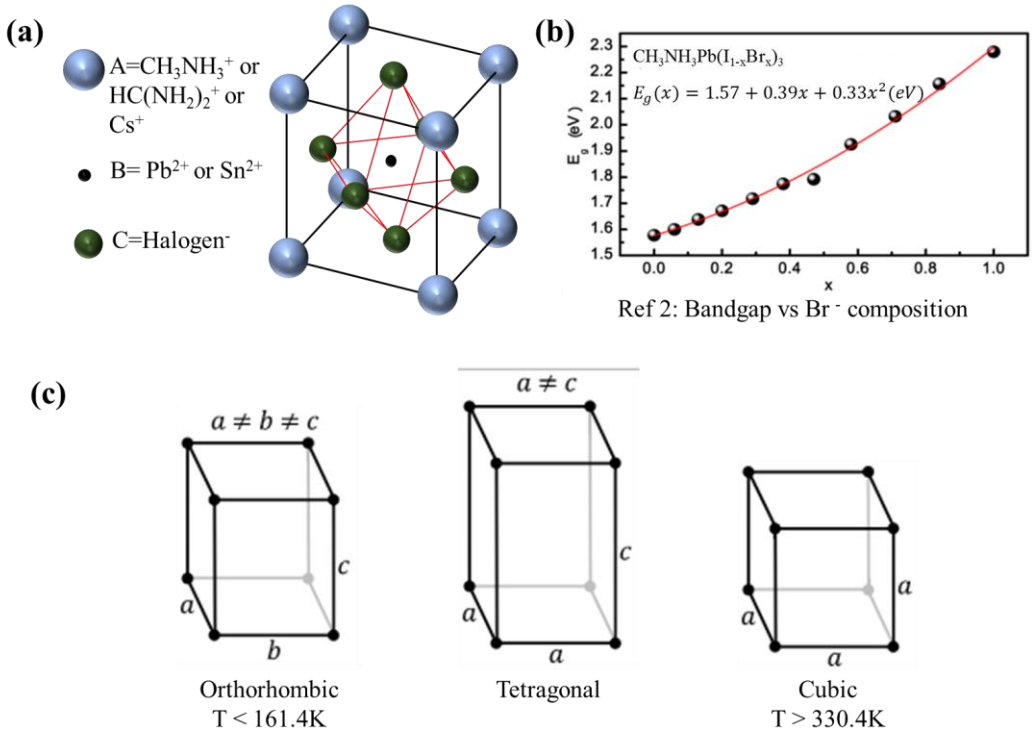

Figure 3.1(a) Perovskite structure of ABX3, (b) band gap energy tuning with I/Br ratio, (c) phase transition of $CH_3NH_3PbI_3$ at different temperatures

Charge transport in perovskites is ambipolar. These materials can work effectively as both an absorber and a hole transporter and an absorber and an electron transporter. Experimental evidences indicate long-range electron-hole diffusion lengths of at least 100 nm in solution processed $CH_3NH_3PbI_3$ and more than 1 μm in mixed halide $CH_3NH_3PbI_{3-x}Cl_x$, [45-48], and more than 150 μm in single crystals. Electron-hole diffusion lengths in perovskites are much longer than those in typical solution processed materials, which are typically 10 nm. The effective mass of both electron and hole in $MAPbI_3$ are small and calculated to be $m_e = 0.23\ m_o$ and $m_h = 0.29\ m_o$ [49], thus providing validation for their long-range ambipolar charge transport property. Recent spectroscopy measurements have indicated low monomolecular (from trap or impurity-assisted recombination) and bimolecular carrier recombination rates (even lower than in GaAs). However, Auger recombination rates were found to be of order 10^{-29} cm^6s^{-1} [49] and comparable to those of strongly confined colloidal quantum dots. For comparison purpose, Auger recombination in GaAs and 1.3 μm InGaAsP is about 7×10^{-30} cm^6s^{-1} and $2\text{-}3 \times 10^{-29}$ $cm^2V^{-1}s^{-1}$, not very different as compared to the perovskites. A lower bound value of carrier mobilities in $CH_3NH_3PbI_{3-x}Cl_x$ and $CH_3NH_3PbI_3$ were determined to be 11.6 $cm^2V^{-1}s^{-1}$ and 8 $cm^2V^{-1}s^{-1}$, respectively [49]. The origin of the long electron-hole diffusion lengths is a result of low charge recombination rates and high charge carrier mobilities in the perovskites. A high absorption coefficient of over 5×10^5 cm^{-1} was observed just above the band gap with a very sharp onset. Below the bandgap, the absorption is exponential over more than four decades with an Urbach energy as small as 15 meV, which suggest a well-ordered

crystal structure [50]. For instance, the Urbach energy in undoped GaAs is about 7 meV and 15 meV in highly doped GaAs material. Very high open circuit voltage (V_{oc}) has been observed in solution processed perovskite solar cells [50]. The V_{oc}/E_g ratio is comparable to the best single-crystal GaAs thin film solar cell and outperforms the ratio obtained in high efficiency polycrystalline thin-film solar cells such as CIGS and CdTe.

Two dominant structures have emerged for perovskite solar cells. In the meso-structure, the perovskite crystal infiltrates a metal oxide scaffold, which is either an n-type TiO_2 layer or an insulating dielectric scaffold, and form an absorptive layer on top of the scaffold. The meso-porous structure usually requires a high-temperature-annealing condensed base layer to minimize the leakage paths from the perovskite layer to the conducting layer [8-11]. Yang et al. from UNIST achieved 22.1% PCE with the conventional TiO_2 based structure in 2017 [11]. The second structure is a planar perovskite film which is sandwiched between n- and p- type interfacial materials. To ensure high performance, the photoactive layer in the planar heterojunction should be a pinhole-free and compact film with uniform coverage and good crystallinity. Several methods have been developed for making thin film perovskites in a planar configuration. As demonstrated in Figure 3.2, they include one-step solution coating, two-step sequential deposition, vapor phase deposition solvent engineering, precursor composition engineering or any combination thereof. Several techniques have been introduced to improve the perovskite thin film morphology by introducing additives to the precursor solution to tune the crystallization kinetics. For example, small ratio of HCl/HI additives in the PbI_2 or mixed perovskite precursors will significantly enhance the solution solubility, thereby greatly improving the uniformity of the perovskite thin

films. The perovskite crystallinity can be finely controlled and optimized with a solvent-assisted annealing technique, the solvent vapor (DMF or IPA) environment will assist the crystallization of the perovskite film during the annealing, result in large perovskite grain sizes.

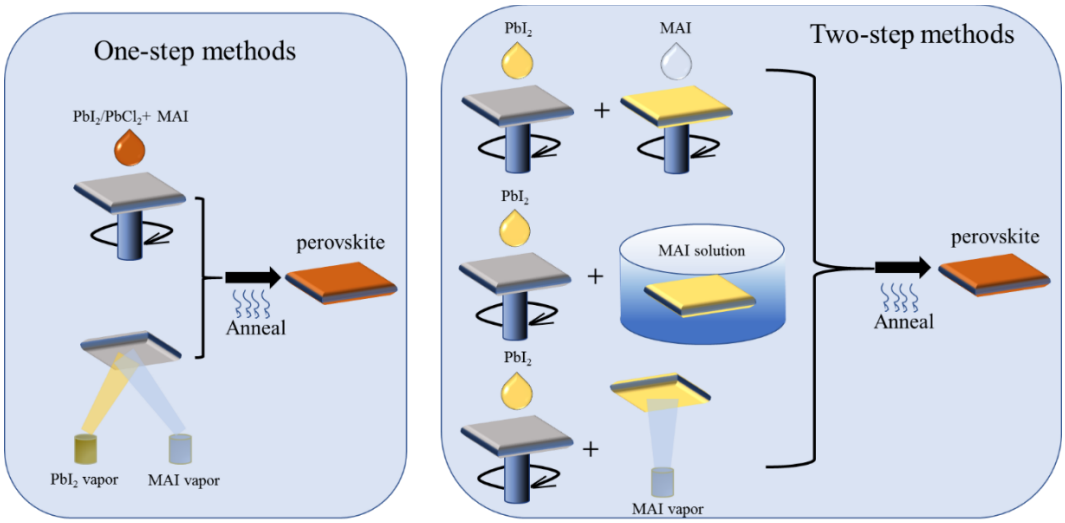

Figure 3.2 Different growing method of perovskite layer, (left) One-step methods, (right) two step methods

The inverted p-i-n structure is dominant in planar perovskite solar cell configuration. This structure simplifies the fabrication procedure without sacrificing too much PCE. Recently, Luo et al. reported 21% PCE with an inverted structure using a mixed-cation lead mixed-halide perovskite material [12]. Unlike conventional TiO_2-based meso-porous structure, there are many candidates for the base p-type material in an inverted planar structure. As mentioned in the Introduction Section, inorganic materials such as doped-NiO_x [13-14] and CuI [15-16], organic material like PEDOT:PSS, PTAA and Poly-TPD have been considered as the hole transport material (HTM) in the planar

perovskite solar cell. PEDOT:PSS is a popular HTM for its high conductivity and low cost, but its relatively lower work function, which leads to a band mismatch with the perovskite material, usually results in smaller open-circuit voltage (~0.9V) [20-24]. Conducting polymers like poly [N,N'-bis(4-butylphenyl)-N,N'-bis(phenyl)benzidine] (poly-TPD) [25-27] and poly(triaryl amine) (PTAA) [28-30] are promising replacement of PEDOT:PSS for better valance band alignment with perovskite material, which in turns expand the quasi-Fermi level difference and increases the Voc. But the non-wetting nature of their surfaces is the main challenge for top perovskite film growth, resulting in poor perovskite film coverage, increased pin-hole density and relatively small perovskite grain size. Recently there have been several breakthroughs in the conducting polymer HTM studies. Xu et al. have reported that poly-TPD based inverted planar perovskite solar cell can have a PCE exceeding 18% [27]. They resolved the problem of the non-wetting nature of poly-TPD by using ultraviolet-ozone surface modification. Huang et al. have proposed to use doped PTAA thin film as the base HTM to reduce the series resistance and recently they boosted the efficiency from 17.5% [29] to 20.6% [30]. In their approach, PTAA solution is mixed with F4-TCNQ as the doping material and m-MTDATA is used as the surface modification material.

In our study, we focus on the simple PTAA-based planar perovskite solar cell without using a complicated surface passivation technique. We propose a sequential method to dope PTAA in an easier and more stable way. Considering the conventional polymer:F4-TCNQ blend solution, it is observed that this doping material often results in drastically reduced solubility of polymers. As a result of this, the mixed solutions must be kept at high temperature and diluted concentrations to avoid rapid aggregation

[31]. In addition, we observe the rapid degradation of F4-TCNQ in a mixed PTAA solution with an obvious color change within a few days, which induces more uncertainties in device performance and solution preparation. To minimize the above-mentioned drawbacks, we propose a sequential method to dope PTAA by exposing PTAA film to the doping solution in an orthogonal solvent system, i.e. toluene for PTAA and 2-propanol for F4-TCNQ. It is found that the PTAA's doping level can be tuned by the concentration of the doping solution. This sequential method improves the device's reproducibility and long-term sustainability. In our work, we have also modified the inter-diffusion method [32] with a controlled solvent-assisted annealing approach to grow high quality perovskite thin film with large grain size (over 2 μm). The optimized recipe guarantees the successful formation of a perovskite layer with average thickness greater than 400 nm without any PbI_2 residue. In this work, we demonstrate a perovskite solar cell with a simple planar structure of FTO/PTAA/$CH_3NH_3PbI_3$/PCBM/Ag and we achieve a champion PCE of 15.3% based on the sequentially doped PTAA thin film without using a complicated surface passivation technique. In the following section, I will demonstrate the fabrication details of the perovskite solar cell.

3.2 Fabrication Details of Perovskite Solar Cell

In this section, I will present the detail recipe of the fabrication of our perovskite solar cell, including the materials and vendor information, process flow and the optimization tips. I hope this section will be helpful as the guideline for the fellow colleagues who work on the same or similar project.

3.2.1 Material, Equipment and Vendors

The raw materials and equipment used in the fabrication procedure of perovskite solar cell are listed in the table 1.

TABLE I
MATERIAL, EQUIPMENT AND VENDORS IN PEROVSKITE SOLAR CELL FABRICATION

Name	Vendor	Purity/Specification
FTO-coated glass	Sigma Aldrich	7 ohm/sq sheet resistance
PEDOT:PSS	Heraeus	Clevios Al 4083
PTAA	Lumtec, tw	Molecule weight ~20K-30K
F4-TCNQ,	Lumtec, tw	Sublimed, >99%
m-MTDATA	Lumtec, tw	Sublimed, >99%
PbI_2 (1)	Sigma Aldrich	>99,99%
PbI_2 (2)	Lumtec, tw	Anhydrous, perovskite grade
Methylammonium-iodide (MAI)	Lumtec, tw	>99.5%
Formamidinium-iodide (FAI)	Lumtec, tw	>99%
Formamidinium-bromide (FABr)	Lumtec, tw	>99%
Methylammonium-bromide (MABr)	Sigma Aldrich	0.18M in 2-propanal

(6,6)-phenyl-C61-butyric acid methyl ester (PCBM)	Lumtec, tw	>99.99%
N,N-Dimethylformamide (DMF)	Alfa Aesar	99.7+%, spec grade
2-propanal	Alfa Aesar	99.7+%, spec grade
Chlorobenzene	Alfa Aesar	99.9%, spec grade
Toluene	Alfa Aesar	99%, spec grade
Dimethyl Sulfoxide	Alfa Aesar	99.9+%, spec grade
SCK-300 Spin Coater Kit	Instras Scientific	500-6000 rpm
Neoprene dry-box gloves (1-pair)	Sigma Aldrich	size 9, port size 6 inch
Compact Glove Box	Changshu Willfo, CHN	Size:550Wx440Dx410Hmm

3.2.2 Fabrication Process Flow

The perovskite solar cell fabrication procedure is shown in Figure 3.3 (a). FTO glass substrate is first cleaned in succession with acetone, methanol, isopropanol (IPA) and deionized water in an ultra-sonicated bath in a clean room. It is critical to have an ultra-clean surface for the substrate FTO, otherwise any dust or grease on it will cause a non-reversible patterned area after spin coating the next layer. Prior to any device

fabrication, the cleaned substrates undergo an ultraviolet-ozone (UVO) exposure treatment for 20 minutes to remove any organic residues.

In the case of preparing PEDOT:PSS based solar cell, the dried FTO substrate is pre-heated on a 120^{o}C hot plate for 10 minutes. It is observed and proved that hot substrate surface will lead to better coverage of PEDOT:PSS layer. The pure PEDOT:PSS was mixed with IPA to improve the interface between PEDOT:PSS and FTO surface, the best performing device is obtained by using a 1:0.5 volume ratio PEDOT:PSS/IPA solution with a spin rate of 3750 rpm for 35s. Then the substrate is annealed on the 120^{o}C hot plate for 15 minutes. After that, it is transferred into a nitrogen filled glove box with precaution to avoid any surface contamination [51].

In the case of preparing PTAA-based perovskite solar cell, the substrate is transferred into the nitrogen filled glove box after the UVO treatment and preheated at 100^{o}C on a hot plate. 20μL hot PTAA solution (2 mg/mL in toluene with 10wt% ratio of m-MTDATA additive) is spin-coated on the hot substrate at 3250 rpm for 45s, followed with 10 minutes drying at 100^{o}C. After cooling down the substrate to room temperature, the F4-TCNQ solution (1 mg/mL in 2-propanol) is dropped on the PTAA surface and left for 30s before spin-drying at 4500 rpm for 45s. The doped PTAA film preparation is completed after 10 minutes annealing at 100^{o}C.

The modified inter-diffusion method is utilized here to grow the perovskite layer. Specifically, high-concentrated PbI_2 solution (550 mg/mL in DMF) is pre-heated on an 85^{o}C hot plate along with the substrate for 10 minutes. Hot PbI_2 solution (~53^{o}C) is spin coated at 3000 rpm on the hot substrate for 35s, a 10-minute post annealing at 85^{o}C is required to dry out the DMF solvent and form a smooth PbI_2 crystal film. Then

a hot MAI solution (75 mg/mL in 2-propanal, ~58°C) is sequentially spin-coated on the PbI_2 layer at 2000 rpm for 2 minutes. The color changes from shiny yellow to dark brown immediately when MAI reaches the PbI_2 surface. Due to the high concentration and low spin-rate of MAI solution, plenty of MAI residue is found to deteriorate the perovskite surface which is detrimental to the formation of the next layer, 30μL Toluene is dropped for the last 30s of the MAI spin-coating period to wash away the MAI residue and passivate the perovskite surface. The pre-crystallized perovskite layer is then moved into a self-built vapor environment for solvent-assisted annealing at 150°C for 1 hour. The same amount of solvent (DMF) is dropped on the 4 coverslips and the solvent vapor stays inside the larger beaker. The small beaker is located on the 4 coverslips which leave some space at the bottom to allow vapor exchange. The precisely controlled amount of solvent vapor which could be DMF or IPA will infiltrate the perovskite film and assist the formation of pin-hole less crystal with large grain size. Considering the 1 cm^2 size of substrate, the optimized solvent amount is 10μL, noting that an oversupply of solvent will generate more pin-holes which will be discussed in the following result analysis.

After 1 hour of solvent-assist annealing, the diluted methylammonium bromide (MABr) solution (4 mg/mL in 2-propanal) is dropped on the room temperature perovskite surface for 30s post passivation treatment, before spin-drying at 3500 rpm. During another 10min annealing at 150°C, this extra thin MABr layer will penetrate the perovskite film and will reduce the defects inside. To grow the electron-transport layer, a 20μL hot PCBM solution (20 mg/mL in chlorobenzene) is spin-coated at 4000 rpm for 30s, followed by 10 minutes annealing at 100°C. The last step is to deposit

patterned contacts to build the cathode and anode. Before transferring the sample to the Angstrom e-beam deposition machine, a corner of the perovskite layer is wiped out to reveal the bottom FTO layer. The cathode contact will be deposited directly on the exposed FTO layer, while the anode contact will be deposited on the PCBM with a chosen pattern. 150 nm Ag contact is deposited at a vacuum pressure of $3x10^{-6}$ torr. The effective device area is defined by the anode contact area which could be varied from 0.01 cm^2 to 0.8 cm^2. The Figure 3.3 (b) shows the completed perovskite layer and the completed perovskite solar cell with a device area of 0.6 cm^2.

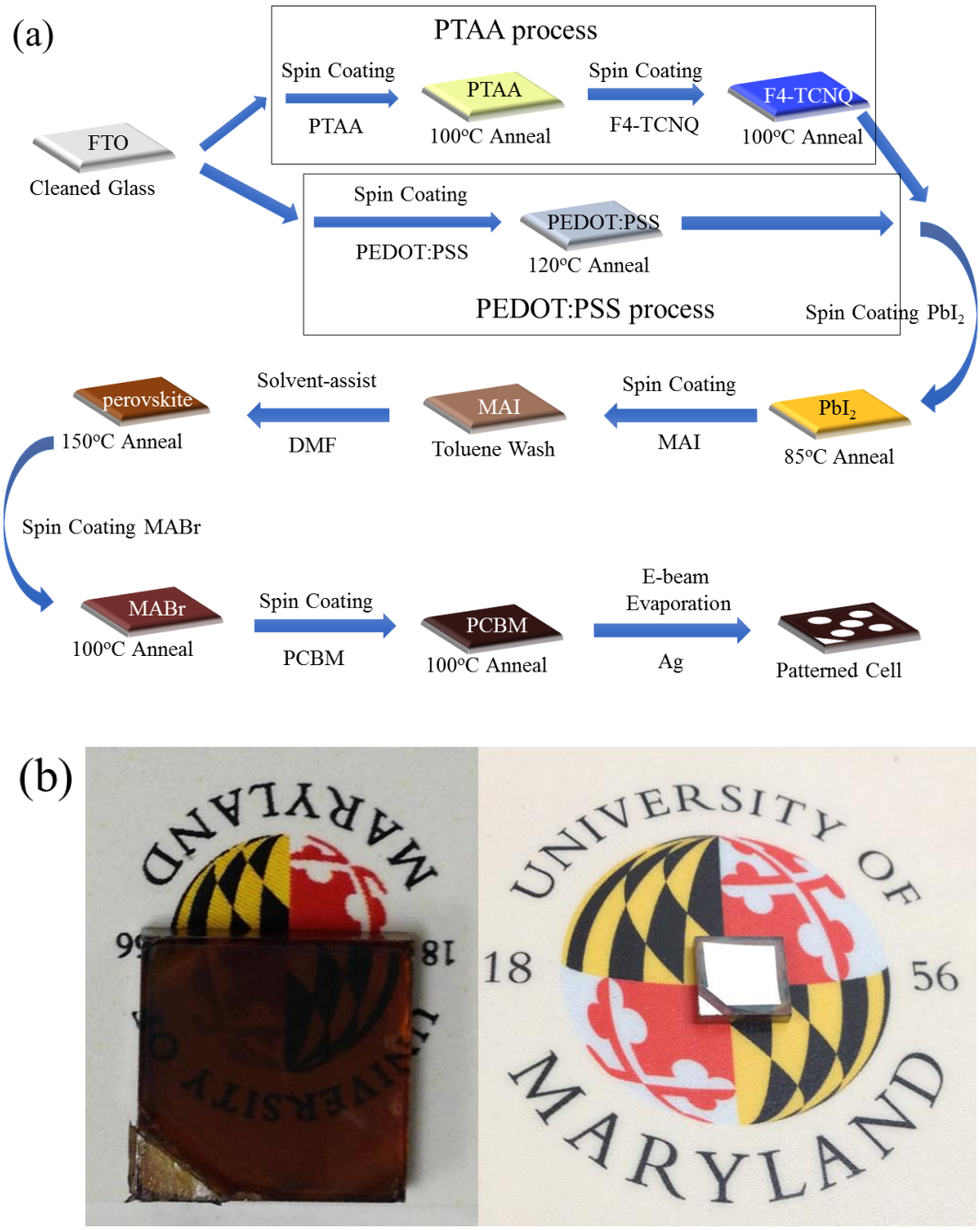

Figure 3.3 (a) The process flow chart of perovskite solar cell fabrication, including the PTAA process and PEDOT:PSS process, (b) The completed perovskite layer and solar cell

3.2.3 Optimization Techniques

There are several optimization techniques in the fabrication of high-performance perovskite solar cell. Here I will summarize some worth-to-know tips based on my experience.

First of all, our glove box is a simple compact dry-box, which has no pressure control system. Manually adjusting the chamber pressure is required to take on/off the gloves. It is crucial to maintain a dry N_2 environment. I suggest every 5 days to routinely evacuate and refill the main chamber. Most of the precursor solutions such as PbI_2, MAI, PTAA are sensitive to air and light, it is suggested to store all the chemical solutions in the glove-box to minimize the natural degradation. We use high concentration PbI_2 and MAI solution in our fabrication recipe, the saturated solutions are suggested to be kept warm at 50^oC on a hotplate in order to avoid recrystallization and precipitation. Some organic materials will degrade naturally in solution within days, such as PTAA and F4-TCNQ, the degrading nature of these organic materials is a struggling issue in our recipe optimization works, I suggest preparing small amount of these solutions (1-2 mL) each time and refresh the solution every 5-7 days.

The optimization of the fabrication recipe follows the controlled-parameter rules. We only change one or two parameters and keep the rest the same for each batch of samples. For example, when tuning PTAA's doping level, we select the best growth recipe of perovskite layer and PCBM, and keep the base PTAA thickness the same for each sample, the only tuning factor is the concentration of the doping solution, while the exposure time and the spin-rate for the doping solutions are kept the same for all the samples. The optimization work of the whole device fabrication is complicated and

time consuming, here I will summarize some key tuning factors in Table 2 that play significant roles in the device fabrication procedure.

TABLE II
OPTIMIZATION PARAMETERS IN PEROVSKITE SOLAR CELL FABRICATION

Name	Tuning Range	Effect
PEDOT:PSS spin rate	3000 – 5000 rpm	Film thickness and coverage
PTAA spin rate	3500 – 5000 rpm	Film thickness and uniformity
F4-TCNQ concentration	0.1 – 2.5 mg/mL	PTAA's doping level
PbI_2 concentration	450 – 550 mg/mL	PbI2 film thickness
PbI_2 spin-rate	3000 – 4000 rpm	Film thickness and roughness
PbI_2 solution temperature	50 – 55 ^oC	Film roughness and coverage
PbI_2 stacks	1 – 3 layers	Film thickness
MAI concentration	75 – 85 mg/mL	Perovskite film quality
MAI spin-rate	1750-2500 rpm	Perovskite film quality
MAI solution temperature	55 – 60 ^oC	Perovskite film quality
Perovskite annealing temperature	140 -150 ^oC	Perovskite film quality
Solvent Amount in SAA	4 – 24 mL	Perovskite grain sizes
MABr exposure time	0 – 30s	Perovskite film passivation
PCBM concentration	15 – 20 mg/mL	PCBM film thickness and coverage

PCBM spin rate	2500- 4500 rpm	PCBM film thickness and coverage
Carbon coating on PCBM	1 – 3 stacks	Perovskite film passivation
Metal contact material	Ag, Au, Ti/Al	Work function alignment

We also made several attempts to replace the organic interfacial layers with more stable inorganic materials. We tried to use ZnO nanoparticles as the n-type material in the perovskite solar cell structure, but the results are negative since we fail to control the ZnO particle sizes during the synthesis procedure. We tried to use sputtering system and ALD to deposit thin film ZnO on the FTO substrate as the n-type base material. We applied the best perovskite recipe on this conventional n-i-p structure. It works as a solar cell but performs poorly with low PCE. I think it is mainly due to the poor hole-blocking ability of the ZnO film grown by sputtering or low temperature ALD. More meticulous work to optimize the ZnO recipe is required.

The inorganic material NiO_x is a good candidate to replace the p-type organic material used in our perovskite recipe, i.e. PEDOT:PSS and PTAA. Some great breakthroughs have been reported, Chen has focused on the doping technique in NiO_x and has reported ~20% PCE using different dopants such as Cu and Cs [17-19]. However, we don't have experience of making high quality NiO_x layer within our perovskite solar cell using a solution process. We must learn the state-of-art techniques from the literature or find our own recipe of the physical deposition methods.

3.2.4 Characterization Techniques and Tools

To evaluate the performance of perovskite solar cell, we use the I-V measurement to extract the power conversion efficiency (PCE) of the solar cell. The Newport Model 91159 Full Spectrum 150 W Solar Simulator produces power equivalent to about 1 sun which was calibrated by a KG-5 Si diode, one Air Mass 1.5 filter is included to adjust the light spectrum. I-V characteristics of the perovskite solar cell were measured in ambient with a Keithley 2400 source-meter. To study the hysteresis phenomenon, the device was measured alternatively in the forward scanning direction (0V to 1V, 60 ms per data point) and in the reverse scanning direction consecutively (1V to 0V, 60 ms per data point). To better understand the crystal composition of the perovskite layer after annealing. X-ray diffraction (XRD) measurements were taken on a Bruker D8/C2 Discover Parallel Beam Diffractometer using Cu Kα radiation. The Scanning Electron Microscope (SEM) images were acquired by a Hitachi SU-70 Schottky Field Emission Gun Scanning Electron Microscope. We used the software "ImageJ" to measure the grain sizes of the perovskite crystals from the obtained SEM images .The Atomic Force Microscope (AFM) images were obtained from an MFP-3D Origin™ AFM (Asylum Research). The software "Gywddion" was used to analysis the AFM data. The External Quantum Efficiency was measured with a self-build photo-spectrometer set-up by illuminating the sample area with a modulated monochromatic light beam (Xenon light source), and amplifying the photo-current with a Stanford Research Systems SR570 pre-amplifier connected to a Stanford Research Systems SR830 lock-in amplifier. The Photoluminescence measurement used the similar set-up of EQE measurement, the

pumping laser light hit on the sample with a confocal lens system. The PL is collected by the focal lens and guided in to the spectrometer with two-mirror system.

3.3 Results and Analysis

3.3.1 Solar Cell Structure and Perovskite Crystal Quality

My work on this project has achieved high performance inverted planar perovskite solar cell with the sequentially doped PTAA hole-transport layer. Figure 3.4 (a) shows the solar cell structure of FTO/PTAA:F4-TCNQ/$CH_3NH_3PbI_3$/PCBM/Ag and Figure 3.4 (b) is the corresponding energy band diagram. We choose PTAA as the base HTM instead of PEDOT:PSS (which we previously used) to enhance the solar cell performance mainly by increasing the open-circuit voltage (V_{oc}). PEDOT:PSS is widely used as a high conductivity and low-cost HTM in the inverted planar perovskite solar cell. However these solar cells usually suffer from low V_{oc} (~0.9V) due to energy level mismatch between PEDOT:PSS and perovskite [52]. This issue can be solved by replacing PEDOT:PSS with an appropriate HTM, which has a better energy band alignment such as poly-TPD or PTAA. As can be seen in the band diagram, the valance band (VB) energy level of PTAA (-5.2 eV) is closer to the perovskite VB level (-5.4 eV) compared with that of PEDOT:PSS (-5.0 eV). This results in a larger quasi-Fermi level separation and a smoother pathway for the hole transport, which in turns increase the V_{oc}.

In this project, we also propose a modified inter-diffusion method to grow the perovskite film. The fabrication details can be found in the previous section. We

modified the conventional method by spin-coating hot, high-concentration, MAI solution on PbI_2 to initiate the reaction and this lasts for 2 minutes to pre-crystalize the perovskite film before the solvent-assisted annealing. There is a trade-off between the perovskite layer thickness (over 400 nm) and the thickness of the PbI_2 residue in the conventional method [32]. We have devoted much effort to optimize the recipe of the modified inter-diffusion method in order to overcome the difficulty of fully consuming PbI_2 layer. Fig. 3.4 (c) shows the XRD pattern of the grown $MAPbI_3$ film on an FTO substrate after annealing. The red curve is the XRD pattern of PbI_2 film, which has a strong peak on its (001) plane. The black curve indicates the XRD pattern of the $MAPbI_3$ film. There are no PbI_2 peaks present compared with the red curve, which reveals the full consumption of the PbI_2 layer. We note that there are some common peaks to both PbI_2 and $MAPbI_3$, which belongs to the FTO substrate. Figure 3.4 (d) illustrates the cross-section SEM image of a single perovskite thin film grown on FTO/PTAA surface. The average thickness of the perovskite layer is about 450 nm with clear tight grain boundaries and lateral grain sizes over 1.0 μm.

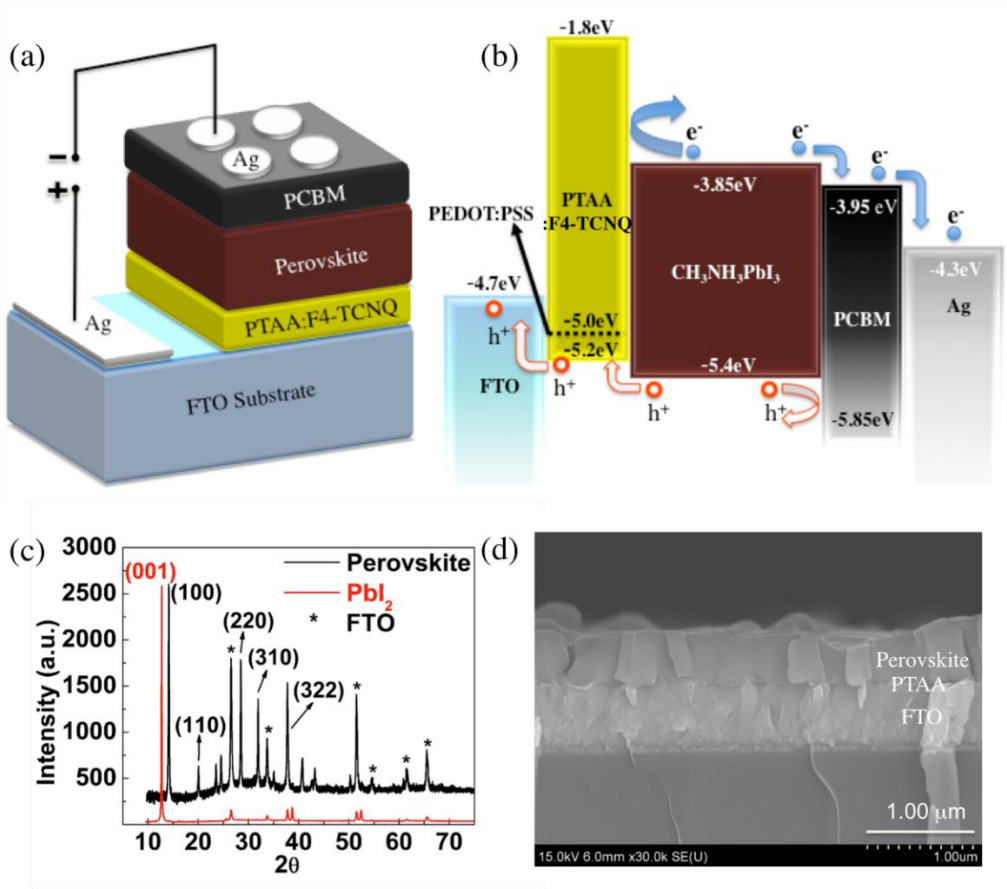

Figure 3.4 (a) Perovskite solar cell planar structure, (b) energy band diagram, (c) XRD pattern of PbI_2 film and annealed perovskite film, (d) cross-section SEM image of FTO/PTAA/perovskite

The perovskite layer is grown directly on the PTAA thin film. The small amount of m-MTDATA additive (10wt% ratio of PTAA) in the PTAA solution plays an important role to modify the non-wetting PTAA surface, enabling full film coverage of the PbI_2 layer. On the other hand, it is found by Huang that the grain size of perovskite is highly dependent on the hydrophobicity of the bottom layer surface [28]. With the help of surface modification by m-MTDATA additive, the PTAA based perovskite grain size is greatly enlarged compared with that of PEDOT:PSS based perovskite. Figure 3.5

shows the SEM images of perovskite crystals grown on PEDOT:PSS and PTAA separately, and their corresponding grain sizes distribution histogram. It can be clearly seen that the perovskite grain sizes in Fig 3.5 (a) are smaller than in Fig 3.5 (b). The average grain size is 528 nm for the PEDOT:PSS based perovskite crystals , and 850 nm for the modified PTAA based perovskite crystals using the same growth conditions.

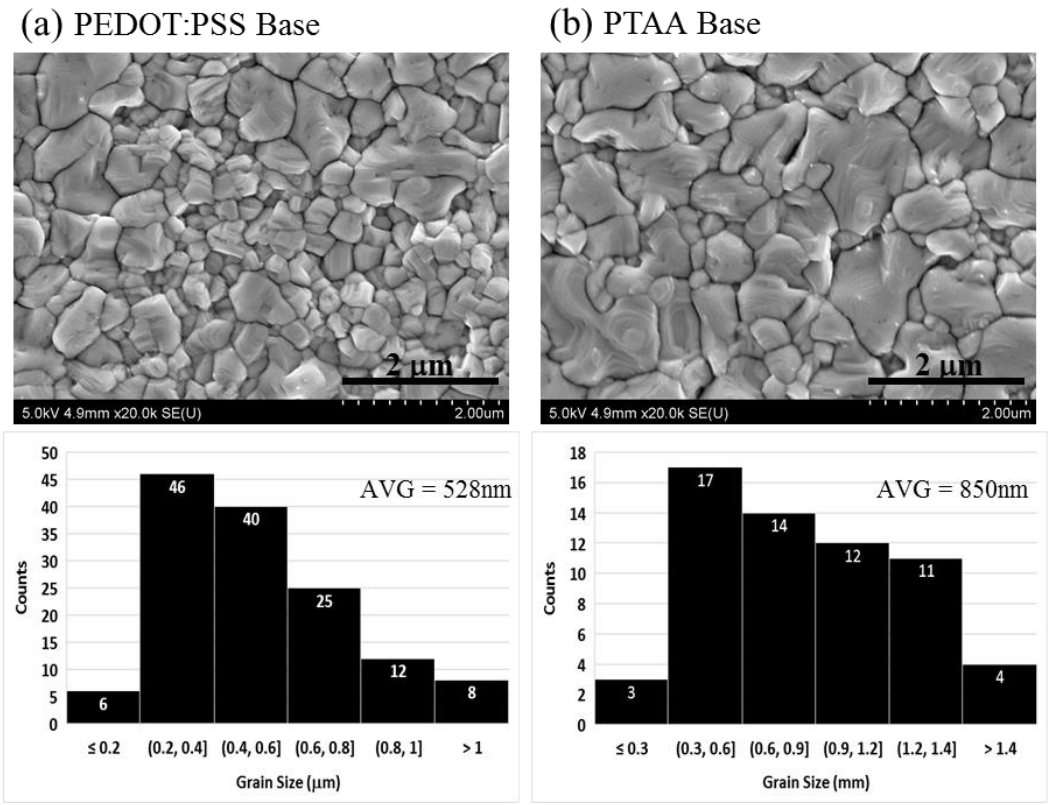

Figure 3.5 (a) SEM image of the perovskite thin film grown on PEDOT:PSS and its grain size distribution histogram (b) SEM image of the perovskite grown on PTAA base and the corresponding grain size distribution histogram

3.3.2 Solar Cell Performance Analysis

Previously we used PEDOT:PSS as the HTM in the perovskite solar cell, and we suffered from the low V_{oc}. The average V_{oc} we observed for PEDOT:PSS based solar cell is ~0.9V, this significantly limit the PCE. The best performance of this solar cell is only 12.7% with 0.92V V_{oc}. Conducting polymers like poly-TPD and PTAA are promising replacement of PEDOT:PSS for better valance band alignment with perovskite material, which in turns expand the quasi-fermi level difference and increases the V_{oc}.

In this project, we replace the PEDOT:PSS with PTAA as the base HTM to enhance the solar cell performance mainly by increasing the V_{oc}. Huang et al. have proposed to use doped PTAA thin film to further reduce the series resistance. They have reported to use a PTAA:F4-TCNQ blend solution with different doping ratios from 0wt% to 10wt%, and claimed that the 1wt% doping ratio performs the best with a lower series resistance [29]. While it has been reported that polymer: F4-TCNQ blend solution requires diluted concentration and high temperature to suppress the doping particle aggregation [31], we also observed the degradation of F4-TCNQ in blend toluene solution. These drawbacks deteriorate the reproducibility and stability of the device performance. It is important to re-prepare the blend solution frequently to avoid using degraded/aggregated solution. Even though we may exclude any uncertainties for each blend solution preparation such as the doping ratio and the solution concentration variation, the dosage of PTAA, m-MTDATA and F4-TCNQ increases remarkably. The cost of solar cell fabrication is greatly raised since the unit prices of PTAA and F4-TCNQ are more than 10 times the price of gold. In our study, we propose a sequential

method to dope PTAA thin films in order to minimize the drawbacks of PTAA:F4-TCNQ blend solutions. We find that F4-TCNQ is soluble in 2-propano but that the PTAA's solubility is very poor. Thus we prepare the PTAA and the m-MTDATA in toluene and the F4-TCNQ in 2-propanol. We then spin-coat the PTAA first and then expose the PTAA thin film in a F4-TCNQ solution for 30 second before spinning the rest of the solution away. The PTAA's doping level can be tuned with the concentration of F4-TCNQ solution. We varied the PTAA's doping level using the sequential doping method and investigated their corresponding solar cell's performance. We also prepared a reference sample based on Huang's best recipe of PTAA blend solution (1wt% doping ratio). Table 3 summarizes the results obtained from five samples with sequentially doped PTAA and the reference sample. The corresponding series resistances are extracted by fitting their I-V curves with the following equation for each sample:

$$\mathrm{I} = \mathrm{I}_L - I_0 \exp\left(\frac{q(V+IR_s)}{nkT}\right) - \frac{V+IR_s}{R_{sh}} \qquad 3.1$$

We can see that the series resistance decreases as the doping concentration increases from 0 to 1 mg/ml. It is attributed to the increased doping level in PTAA thin film, which minimizes the PTAA's sheet resistance. The AFM images of PTAA surface exposed with different doping solutions are shown in Figure 3.6. We can clearly see the aggregated doping dots on the sample surface from Figure 3.6 (c), (d), (e), but the root-mean-square (rms) roughness of the corresponding PTAA films is almost the same and is around 13 nm. The dot size is increasing with the doping concentration. For PTAA doped with 2.5 mg/ml doping solution, enormous doping clusters are observed which result in larger effective sheet resistance of the PTAA film. This explains the

abnormal increase of the series resistance of the solar cell sample exposed with 2.5 mg/mL doping solution. For the reference sample, we observed a slightly smaller V_{oc} of 0.98V but much smaller photocurrent of 18.8 mA/cm^2. While the FF and series resistance are comparable to our best sample with sequential doped PTAA, it turns out the sequential method could also achieve the optimized doping level of PTAA using the pristine blend PTAA solution.

TABLE III
THE PARAMETERS OF PEROVSKITE SOLAR CELL SAMPLES USING PTAA EXPOSED WITH VARIOUS DOPING CONCENTRATIONS

Doping Concentration	V_{oc} (V)	J_{sc} (mA/cm^2)	FF (%)	PCE (%)	R_s (ohm*cm^2)
0	0.91	20.7	52.4	9.9	11.6
0.1 mg/mL	0.97	21.6	67.6	14.2	6.2
0.5 mg/mL	0.96	21.4	70.5	14.5	5.2
1.0 mg/ mL	1.00	22.1	68.8	15.3	4.8
2.5 mg/ mL	0.94	19.7	58.5	10.9	9.8
Reference	0.98	18.8	68.8	12.7	5.1

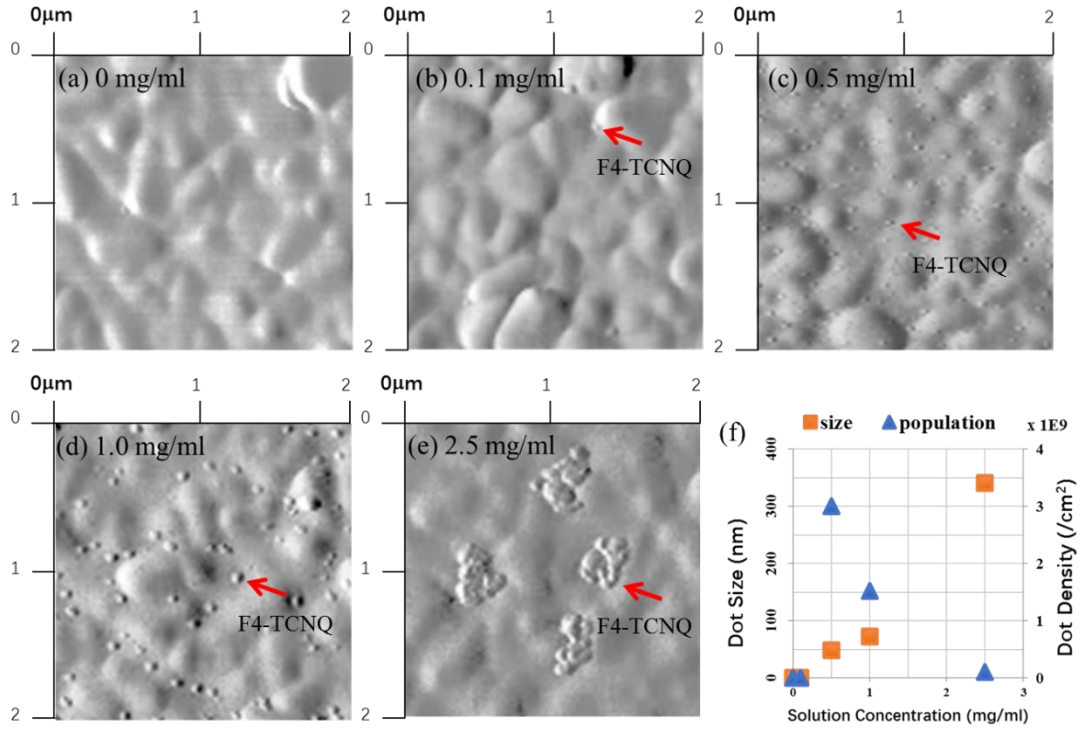

Figure 3.6 AFM image of PTAA surface exposed with (a) 0 mg/mL, (b) 0.1 mg/mL, (c) 0.5 mg/mL, (d) 1.0 mg/mL, (e) 2.5 mg/mL and (f) the summarized doping size and density chart of corresponding PTAA surface.

Larger grain sizes reduce the grain boundaries and the interface traps, and long carrier diffusion lengths of the perovskite material enable better carrier transfer within the perovskite grains. As a result, larger perovskite grain sizes will improve the solar cell performance. In our study, the perovskite grain size and the pin-hole density can be finely controlled by tuning the solvent amount during the solvent-assisted annealing (SAA). Figure 3.7 shows the set-up for the SAA that can precisely control the solvent vapor amount. Specifically, the same amount of solvent (DMF) is dropped on the 4 coverslips inside the large beaker, and the small beaker stands on the coverslips and

leaves some space at the bottom to allow slow vapor exchange. The device is annealed inside the small beaker.

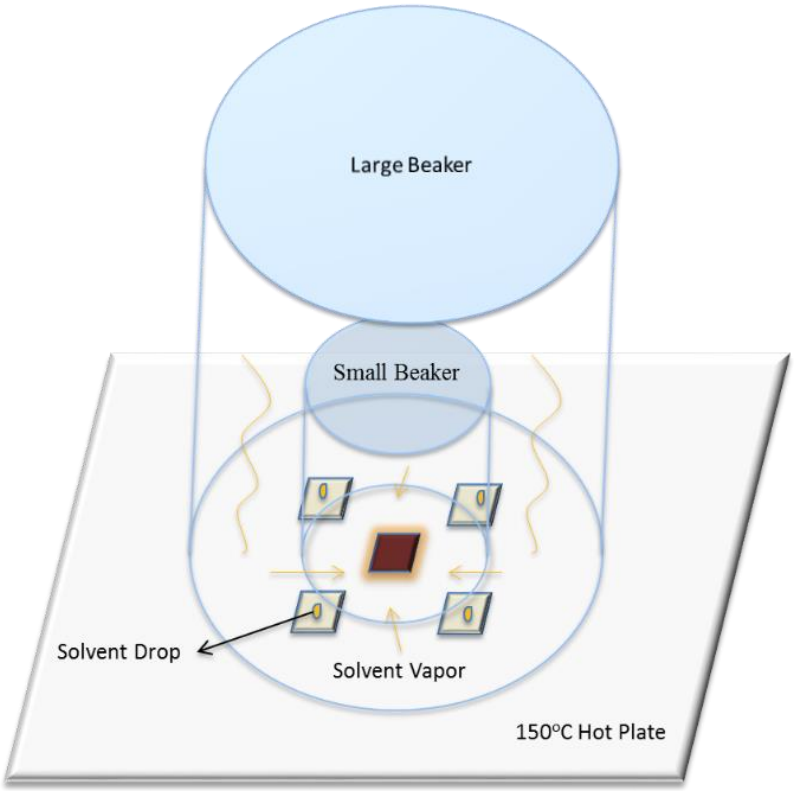

Figure 3.7 The two-beaker set-up of solvent-assisted annealing

It is observed that the solvent amount can affect the grain size of the perovskite crystals. Figure 3.8 (a), (b) demonstrates the SEM images of the perovskite crystals annealed with different SAA conditions. Without solvent vapor, the average grain size of the perovskite crystals is 0.85 μm as previously shown in Fig 3.5(b), while it is enlarged to 1.5 μm with 4 μL DMF SAA condition, and above 2.0 μm with 10 μL DMF SAA condition. We also observed the saturation effect of SAA on the grain size enhancement. Too much solvent during SAA will not improve the perovskite crystal

quality, since the pin-hole density will keep increasing with the solvent amount. The optimization of the SAA condition is required to obtain high quality perovskite crystals with a low pin-hole density and large grain sizes. The dependence of the solar cell performance on the SAA condition was investigated. Figure 3.8 (c) shows the I-V performances of three perovskite samples with 0, 4 μL and 10 μL solvent amount during SAA. The 10 μL SAA sample performs the best and exhibits the largest fill factor (FF) and short circuit current (J_{sc}). Figure 3.8 (d) shows the external quantum efficiency (EQE) of these samples and the integrated photocurrents are consistent with their I-V performances. The better performance of 10 μL SAA sample also corresponds to the observed best perovskite crystal quality. Larger perovskite grain sizes provide better carrier transport within the perovskite layer with less recombination trap states. As a result, a larger photocurrent and EQE are observed in this sample. It is interesting to notice that the FF of the 4 μL SAA samples is even less than that of the 0 ul SAA sample. It is due to the increase of the pin-hole density that trades-off the benefit of grain size enhancement, which provides more shunt-paths within the perovskite layer and reduces the shunt resistance of the device.

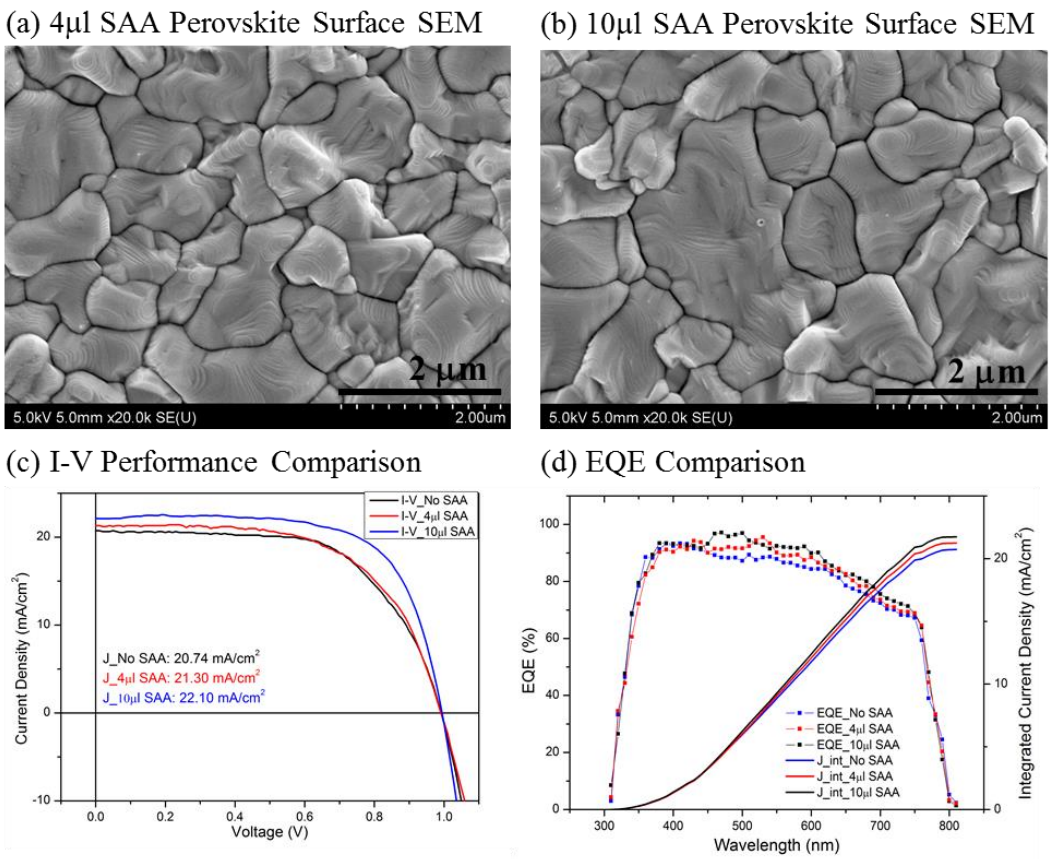

Figure 3.8 SEM images of perovskite grains annealed with (a) 4 μL solvent and (b) 10 μL solvent during solvent-assisted annealing; (c) the I-V performances of solar cells with No SAA, 4 μL SAA and 10 μL SAA; (d) the EQE comparison of the corresponding solar cells.

Figure 3.9 (a) shows the solar cell performance comparison between the PTAA and the PEDOT:PSS based champion cell. The PTAA based solar cell demonstrates an increase of the J_{sc} from 19.8 mA/cm^2 to 22.1 mA/cm^2 and the V_{oc} from 0.91V to 1.0V. Though the FF decreases from 71% to 69%, the PCE of the PTAA based solar cell reaches 15.3% compared with 12.7% from the PEDOT:PSS based solar cell. The improved V_{oc} is still less than the expected 1.1V, which indicates the imperfect energy

band alignment in our solar cell system. We thought that the defects at the PTAA/perovskite interface will introduce some trap states within the energy band, which in turns will lower down the work function of PTAA so that the electron-hole quasi-Fermi level separation decreases and V_{oc} drops as a consequence. Further work is required to investigate this assumption and solve the issue. We also measured the EQE of the champion solar cells based on PTAA and PEDOT:PSS respectively. As shown in Figure 3.9 (b), the EQE of the PTAA based solar cell remains above 90% for the spectral range from 380 nm to 600 nm and then slowly drops to 80% at 680 nm, while the EQE of the PEDOT:PSS based solar cell decays faster to 70% from 400 nm to 680 nm. The integrated photocurrent is 21.7 mA/cm^2 for the PTAA based solar cell and 19.4 mA/cm^2 for the PEDOT:PSS based solar cell, which are in good agreement with their measured short circuit currents. The relatively low EQE in the region from 600 nm to 750 nm indicates the insufficient perovskite thickness for both devices. We should further optimize our recipe to grow a thicker perovskite layer for a larger photocurrent and a higher power conversion efficiency.

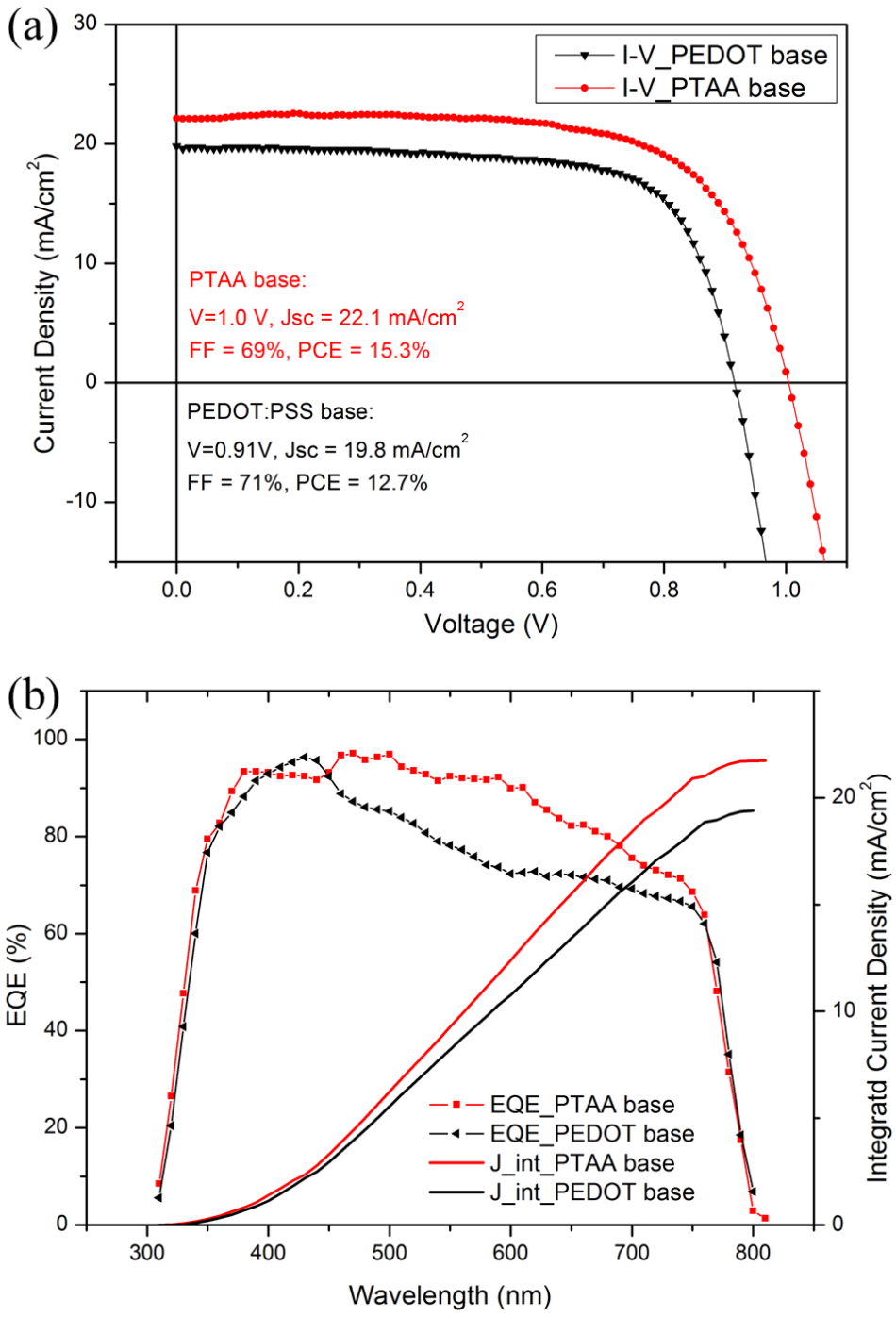

Figure 3.9 (a) the photovoltaic performance comparison between champion cells with PTAA and PEDOT:PSS base, (b) the EQE comparison between PTAA based solar cell and PEDOT:PSS based solar cell

3.3.3 Hysteresis Issue and Solution

Hysteresis effect has been observed in most perovskite devices using metal oxide as the carrier transport layer. As can be seen in Figure 3.10 (a), the I-V curves measured when using opposite scan directions, do not overlap. Recently, the most convincing explanation for hysteresis effects is the ion migration hypothesis [53-54]. Figure 3.10 (b) illustrates the ion migration and energy diagram of the device before and after the light-soaking. The ions within the perovskite will move to the interface with an applied external voltage or photo-voltage. The formed dipoles will affect the carrier extraction then cause hysteresis effect. The favorable solution for hysteresis free perovskite solar cell is to use an inverted structure and use PCBM as the top electron transport layer. Compared with metal oxide material, the PCBM particles can easily diffuse into the perovskite film through grain boundaries. The moving ions will be captured by PCBM particles and form a PCBM halide radical [55], which reduces the density of interface dipoles and suppress the hysteresis. In our studies, the hysteresis effect is suppressed by using PCBM as the top electron transport layer. Figure 3.10 (d) shows the performance of a typical perovskite solar cell with 14.6% PCE in the forward and reverse scanning directions. The hysteresis effect is mostly suppressed. The thickness dependence of the PCBM film to the perovskite solar cell performance was also investigated. Although a thinner PCBM layer is preferred to reduce the series resistance, it will lead to poor coverage and electrode penetration and enable more shunt paths and current leakage.

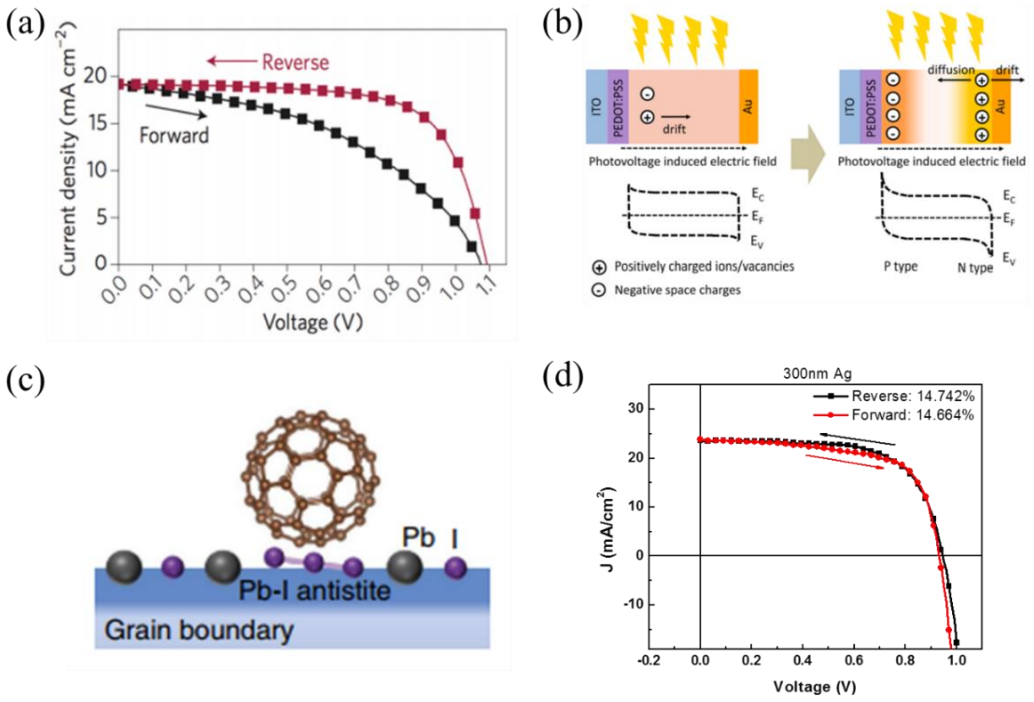

Figure 3.10 (a) The hysteresis effect in the I-V measurement of perovskite solar cell, (b) ion migration and the band diagrams of the perovskite solar cell device before and after the light soaking, (c) PCBM molecule passivates the Pb-I anti-site defects at the perovskite surface to suppress the ion migration, (d) our typical I-V curves without hysteresis after applying PCBM on top of perovskite layer.

3.4 Other Application of Perovskite Material

3.4.1 Perovskite Tandem Cell

The relatively wide and tunable bandgaps make perovskite highly attractive for use in multijunction solar cells on top of narrower bandgap absorbers, such as silicon, copper indium gallium selenide and Sn-containing (CIGS) perovskites [56-58].

Among all the PV technology, silicon (Si) solar cells take the dominant market share due to the high efficiency, excellent stability, and relatively low manufacturing costs at the module level [59]. The construction of perovskite/silicon tandem solar cell is an ideal approach consisting of two or more sub-cells that have the potential to further improve the efficiency of the Si PV without extensive manufacturing cost increase [60]. Qiu, et al. from Peking University reported a perovskite/Si tandem solar cell with 1.69 eV bandgap for the perovskite absorber which delivers a PCE of 22.22% [61]. And Bush, et al. from Stanford improve the efficiency of monolithic perovskite/silicon tandems to 23.6% by combining an infrared-tuned silicon heterojunction bottom cell with the recently developed cesium formamidinium lead halide perovskite [62].

In our group, we have already demonstrated mature techniques of fabricating CIS solar cell and perovskite solar cell. We propose to implement both mechanically stacked and monolithic Perovskite/CIS tandem solar cells. In the mechanically stacked approach, the two sub-cells operate independently with separate sets of terminals, which avoids electrical crosstalk and eliminate constraints associated with current matching and the need for a tunnel junction. A transparent and electrically insulating material serves as the interface layer in the tandem. Fig.3.11 shows the proposed structure with four terminals. The bottom sub cell uses exactly the same structure as the stand-alone CIS cell that we have developed in our laboratory. For the Perovskite top sub cell, we have to use transparent electrodes for both side of it. Here, ITO is chosen. The two sub cells have slightly different size, where the top cell is relatively smaller. This is designed to have the Al/Ni contact recessed. Then, with our excellent

alignment technique and electrical expertise, we will get high performance tandem solar cell by optimizing our existing high-quality Perovskite and CIS solar cells by reducing optical losses in the structure.

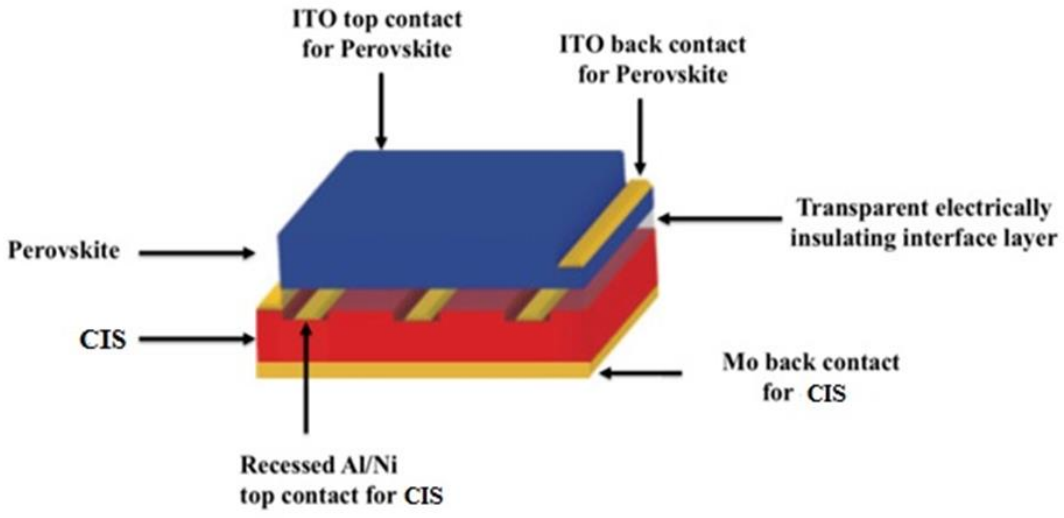

Figure 3.11 Four-terminal mechanically stacked Perovskite/CIGS tandem

Another tandem solar cell design is to adopt a monolithic two-terminal architecture. Sophisticated optimization of a number of elements is required in this architecture, such as current matching, development of an appropriate recombination/tunneling layer. Figure 3.12 shows the band diagram of the proposed monolithic perovskite/CIS tandem cell: transparent conducting electrode (ITO)/PCBM/$CH_3NH_3PbI_3$/PEDOT:PSS/ITO (or AZO)/CdS/CIS/Mo/Soda lime glass. In this case, the tunnel junction consists of a PEDOT:PSS layer as a p recombination layer and an ITO or AZO layer as n recombination layer. In order to make the current matched between both sub cells, we will explore the following approaches. First, we will adjust the $CH_3NH_3PbI_3$ thickness;

second, we will adjust the Perovskite band gap by sweeping from $CH_3NH_3PbI_3$ to $CH_3NH_3PbBr_3$ to include a small proportion of Br in our perovskite structure; third, we will reduce the thickness of ITO, PEDOT:PSS and PCBM to decrease the losses and increase the short circuit current of CIS by letting more photon being absorbed in the bottom cell.

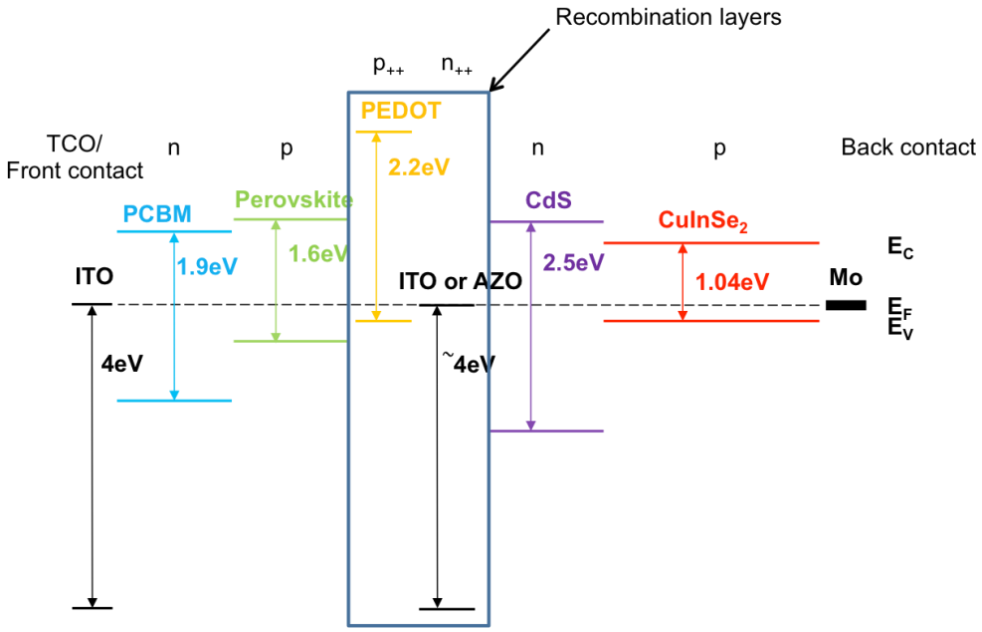

Figure 3.12 Band diagram for monolithically integrated Perovskite/CIS tandem cell

3.4.2 Perovskite Based Laser Cavity

Due to the remarkable property that the bandgap can be adjusted [5], solution-processed, high charge-carrier mobility [4] and high photoluminescence (PL) quantum efficiencies [63], the perovskite materials enable the possibility of realizing low-cost solution-cast tunable laser diode.

We proposed a planar structure for optically pumping a perovskite-based laser cavity. The active material and spacing layer are sandwiched between the two mirrors, forming a Fabry-Perot gain cavity as shown in Figure 3.13. The broadband dielectric mirror is purchased from Thorlabs (BB1-E03). It has a high reflectivity region between 750 nm to 1100 nm, which will cover the PL wavelength region of perovskite. We use the solution process to grow the perovskite layer on top of the mirror. The mirror is cleaned with acetone, methanol, isopropanol and DI water alternatively. The hot PbI_2 solution (400 mg/mL) is spread out on the hot surface of the dielectric mirror with 200 rpm spin-rate, then the spin-rate is rapidly increased up to 5000 rpm in 0.01s. After 10 minutes of 90^{o}C annealing, the high concentrated MAI solution (75 mg/mL) is spin-coated at 3000 rpm for 2 minutes. The perovskite surface is washed by toluene during the last 30s of MAI spin-coating. Then 30 minutes post-annealing at 150^{o}C hot plate is required for perovskite crystallization. A thin layer of A3 PMMA is spin-coated at 4000 rpm to encapsulate the perovskite. This will protect the perovskite film from degradation in ambient and from e-beam damage when depositing SiO_2. The Fabry-Perot cavity length is precisely defined by controlling the SiO_2 layer thickness by e-beam deposition and a thickness monitor. Finally, a 150 nm Ag is deposited on the top surface of the sample as the metal mirror of the cavity.

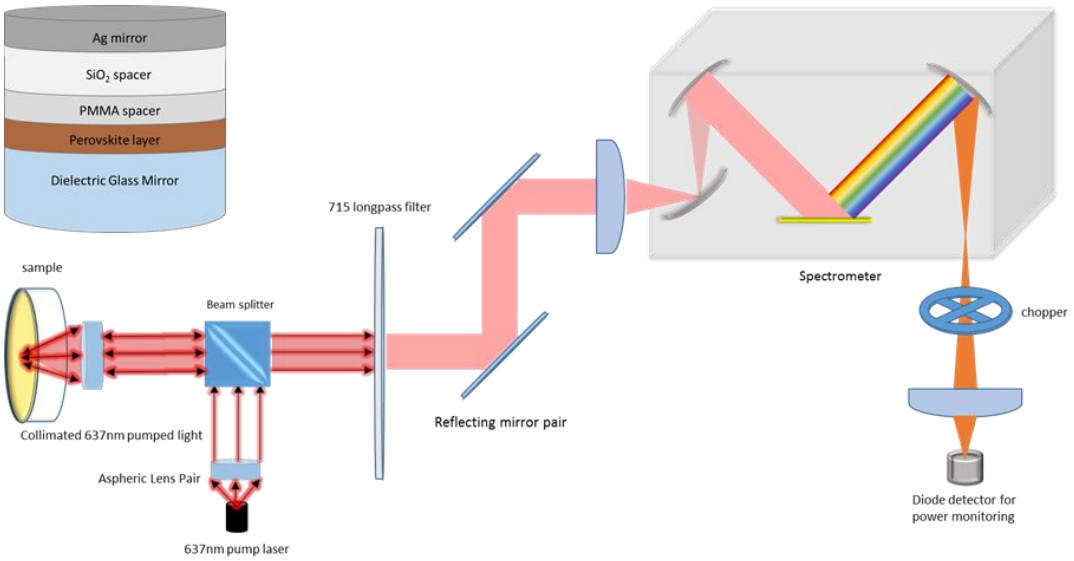

Figure 3.13 Layer structure of perovskite Fabry-Perot Cavity and self-build pulsed laser pumping PL measurement system

We use a self-build system to measure the PL response of the sample, as shown in the Figure 3.13. The pumping source is a 638 nm laser diode in a pulsed current driven mode (25ns pulse width and 0.025% duty cycle). We use a confocal lens to focus the laser beam and collect the PL signal. We measured the PL of perovskite with and without a resonant cavity respectively. As shown in Figure 3.14, the black line represents the PL spectrum of a bare perovskite film on a mirror. It produces a wide spectrum from 730 nm to 810 nm. The yellow line shows the PL spectrum of the perovskite film from a resonant cavity with 5 times magnification. The Fabry-Perot cavity length was designed to excite a resonance peak within the PL spectrum range of the bare perovskite film (730 nm to 810 nm). We observed two peaks from the PL spectrum of the perovskite cavity located at around 750 nm and 790 nm. Previously we thought that these two peaks may be the resonance peaks due to the Fabry-Perot cavity,

but their positions were fixed when we changed the cavity length. Later we convinced ourselves that these two peaks were just the transmitted PL signal through the mirror. We used a halogen light source with a broad-spectrum range to measure the reflectance of the E03 coating mirror. From the reflectance spectrum curve in Figure 3.14, we observed two dips in the high reflecting region (>720 nm) which are at 750 nm and 790 nm. The identical location of the E03 coating mirror reflection dips and the perovskite PL peaks demonstrated to us that the measured PL peaks around 750 nm and 790 nm were not the resonance peaks of the cavity, but were the transmitted PL spectrum of the perovskite film through the E03 coated mirror.

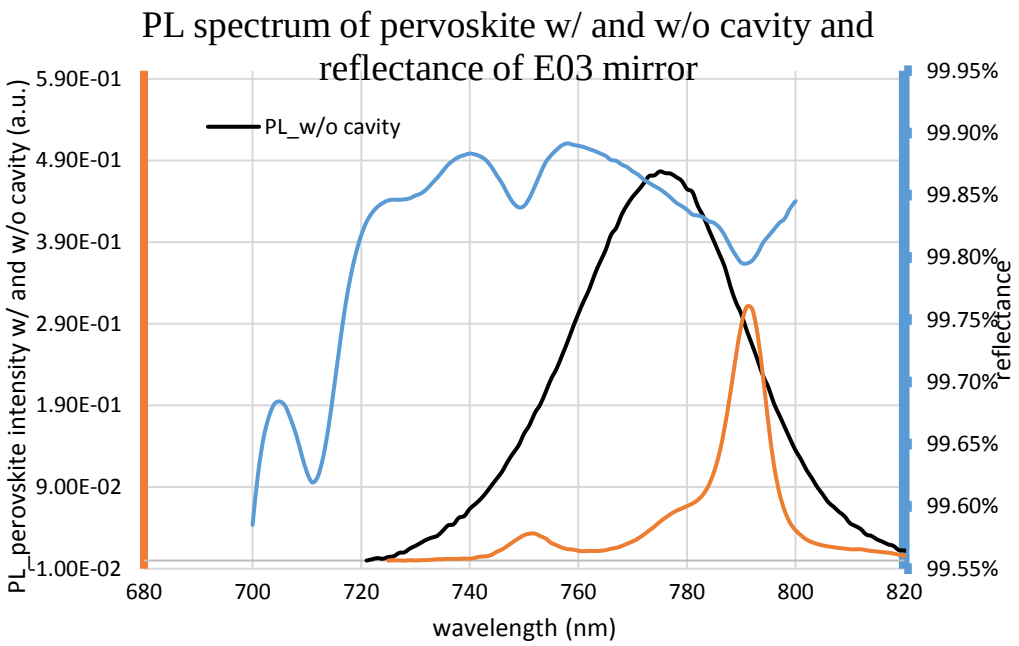

Figure 3.14 PL spectrum of bare perovskite film (black line), and PL spectrum of perovskite Fabry-Perot cavity (orange line, magnitude x 5), and reflectance of E03 coating mirror (blue line)

We believe that the missing excitation peaks of the resonance cavity is due to the lack of optical gain. The resonance peaks are potentially buried in the transmitted PL signal. More optical gain is required to compensate the high loss caused by the high absorption coefficient and surface roughness of the perovskite film. Increasing the pumping power density is an effective way to improve the optical gain. We use a single mode 638 nm diode laser with 170 mW maximum optical power (HL63133DG from Thorlabs) to pump a ~24.5 μm^2 spot on the perovskite film. After a beam splitter and coating on the mirror, the maximum pumping power density on the perovskite film is

$$170mW \times 0.6 \times 0.7 \div 24.5\mu m^2 = 291.4kW / cm^2 \qquad 3.2$$

The factor of 0.6 and 0.7 are due to the beam splitter and coating respectively. We also tried to cool down the perovskite sample to further increase the PL signal intensity. The peak wavelength is red shifted from 775 nm to 782 nm and the integrated PL intensity is increased by a factor of 1.5 when the sample temperature is cooled down from 298K to 250K (the lowest temperature we can reach with our TE cooler system). Figure 3.15 showed the PL spectra from the same spot on the perovskite film inside a resonance cavity with various pumping power at room temperature and 250K respectively. As the pumping power increases at room temperature, we could only see the transmitted PL profile at ~785 nm which is increasing linearly, no other obvious resonance peaks observed. At 250K, the PL intensity is increased by a factor of 1.5 at the same pumping intensity, we potentially observed a resonance peak at 788 nm. However, this peak is very close to the 785 nm transmitted PL peak profile and is not a sharp peak. We need to keep increasing the pumping power or PL intensity equivalently till we observe the laser effect (the intensity of the resonance peak should increase non-linearly, and the

line-width should narrow) before we can confirm that this peak is truly a resonance peak. However, we are reaching our maximum pumping power and the lowest sample temperature that we can reach; we cannot prove the existence of an optically pumped laser using our present perovskite laser cavity. But for many samples that we have measured, we have observed some potential resonance peaks both at room temperature and 250K. What we need to do next is to keep enhancing the optical gain inside the cavity. There are three approaches to obtain more optical gain inside the cavity: utilizing more powerful laser to directly increase the pumping power on the perovskite film; cooling the sample down to lower temperature (160K) to enhance the PL intensity; optimizing the perovskite film with smoother surface and higher PL quantum efficiency. We currently have the cryo-cooler system that can reach 8K. Future work will integrate the current PL measurement system with the cryo-cooler and will measure the low temperature PL from the laser cavity. Potentially we may observe the laser excitation peaks within the appropriate wavelength region.

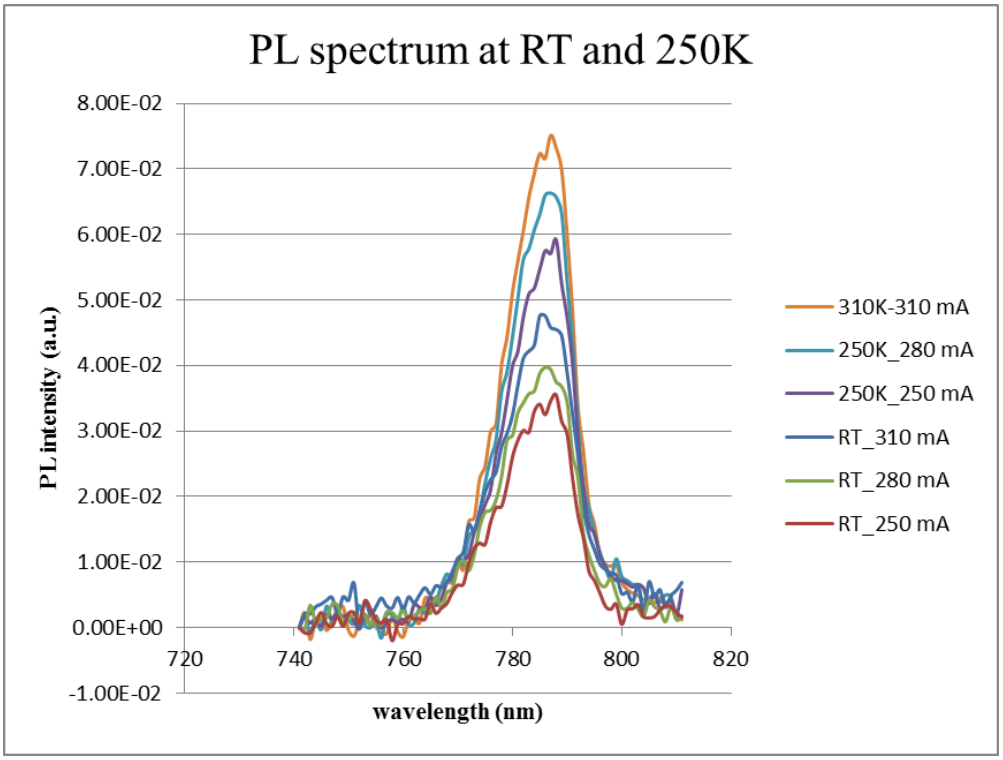

Figure 3.15 PL spectrums from perovskite Fabry-Perot Cavity with various pumping power, measured at room temperature and 250K respectively.

3.5 Summary of the Perovskite Solar Cell Project

In this project, I first summarized the material properties, solar cell structures and fabrication techniques of perovskite solar cell. And I briefly reviewed some state-of-art perovskite solar cell with different features. Then I discussed in detail with the proposed sequential doping method to fabricate PTAA based perovskite solar cell using simple inverted planar structure without any complicated surface passivation techniques. Compared with conventional PEDOT:PSS, PTAA increases the electron-hole quasi-Fermi separation so that the open circuit voltage is remarkably improved. The sequential method provides an easier and more stable way to dope PTAA with F4-

TCNQ in an orthogonal solvent base. The PTAA's doping level is tunable with the doping solution's concentration. It changes the PTAA film's sheet resistance and improves the solar cell's performance. We have modified the inter-diffusion method for perovskite thin film growth in a controllable solvent-assisted-annealing set-up. We are able to grow high quality perovskite crystals with grain sizes over 2 μm and thicknesses around 450 nm. The highest power conversion efficiency of 15.3% is obtained under AM1.5 irradiation. The measured photocurrent is consistent with the integrated photocurrent from the measured EQE data. However, the open-circuit voltage of 1.0 V is still below our expectation. We assume that the interface traps between the PTAA and the perovskite layers are the main cause for low V_{oc}. More optimization is required to further improve the solar cell's performance.

I have also initialed the studying of the perovskite tandem solar cell. Currently people have successfully demonstrated high efficiency monolithic perovskite/Si tandem cell based on mixed-cation perovskite material. Our group has the capability to fabricate high efficiency CIGS solar cell and perovskite solar cell. We propose to implement both mechanically stacked and monolithic Perovskite/CIGS tandem solar cells. Other application of perovskite material such as perovskite-based laser cavity was also investigated. Photoluminescence (PL) measurement of the perovskite thin film was performed and shows a strong spontaneous emission peak around 780 nm. We proposed a Fabry-Perot cavity comprising of a gain medium of perovskite layer and a protecting layer of PMMA and a spacing layer of SiO_2 between a high reflectivity dielectric mirror and a silver metal mirror. A pulsed laser optical pumping configuration was used to minimize thermal effect in the gain material. Currently we

did not observe the laser effect due to the insufficiency optical gain inside the cavity. Pumping the cavity at cryogenic temperature may significantly enhance the photoluminescence and we may potentially observe the excitation peaks with current cavity structure.

Chapter 4 Intermediate Band InAs/GaAs Quantum Dot Solar Cell

4. 1 GaAs Solar Cell Fabrication Techniques

This section will summarize the fabrication techniques used to make GaAs based solar cell.

4.1.1 Cleaning, Etching and Electrode Contacts

The surface of GaAs must be cleaned before any follow up steps like etching in order to achieve a surface free of organic and inorganic contamination. The wafer should be cleaned with boiling acetone, methanol, and isopropanol for 10 minutes respectively to remove any organic grease. To remove the inorganic contamination, the following procedure is recommended: 1) rinse the wafer in diluted HCl (1:10) for 30s, 2) rinse with DI water for 30s, 3) immerse the wafer in diluted NH4OH (1:10) solution for 1 minute, 4) rinse with DI water and dry with N_2 flow. The HCl treatment will result in an As-rich surface, the NHOH solution will restore the Ga/As ratio by removing the excess As atoms on the surface. After the cleaning, the oxide-free GaAs surface should be hydrophobic.

Device patterning is mainly achieved by etching. There are two main etching methods—dry etching and wet etching. Dry etching is much more desirable than wet etching for defining mesa area. We have used a Fluorine-Induced Coupled Plasma (F-ICP) etcher from Oxford to define the Si_3N_4 hard mask. and Chlorine-Induce Coupled

Plasma (Cl-ICP) for the sequential etching into the GaAs. In our recipe, BCl_3/Cl_2 mixture tend to produce smoother surfaces than Cl_2 only plasmas.

While dry etching is preferred over wet etching for its better profile control and etching uniformity, it could seriously degrade the electronic properties of the surface. Wet etching is free of physical bombardment, so it is preferred when surface quality needs to be preserved. In our devices, the top layer of GaAs is generally 20 nm to 50 nm, where high-energy photons are first absorbed due to the high absorption coefficient. An $Al_{0.8}Ga_{0.2}As$ window layer is beneath the GaAs top contact layer. Selective etching can't be used here since $Al_{0.8}Ga_{0.2}As$ will oxidize quickly once exposed to air. To minimize the photon loss, we use wet etching to thin down the top layer to about 5 nm. We have used citric acid etchant with an etching rate or 5 nm/min. The solution is prepared fresh every time for a uniform etching rate.

The electrode contact patterns are usually formed by lift-off technique. In order to achieve a good lift-off film, the surface cleanness is critical, and a good undercut profile sometimes is required. The p-type electrode contact is Ti/Pt/Au (30/80/100 nm). Ti is for adhesion purpose, Pt is to provide an Ohmic contact work function with p-type GaAs. A thick Au layer is for the wire-bonding process. The n-type electrode contact is Au/Ge/Ni/Au (5/30/20/100 nm)., the Au and Ge with the chosen thickness ratio will melt at the eutectic temperature after a 1-minute rapid thermal annealing process at 400^{o}C. The Ni layer is used to provide the right work function. The last layer of Au is to provide a layer for bonding and for packaging purpose.

4.1.2 The Process Flow of GaAs Solar Cell Fabrication

Here I will summarize the standard GaAs solar cell fabrication process flow in the order of Figure 4.1.

1. Clean the wafer with acetone, methanol and isopropanol in an ultra-sonic bath for 10 minutes respectively. Then make sure the n-type GaAs is facing up and immerse the wafer in diluted NH_4OH ($NH_4OH:H_2O$=1:10) for 1 minute. After cleaning, quickly transfer it into the e-beam evaporator to minimize the surface oxidization. Deposit Au/Ge/Ni/Au (5/30/20/100 nm) when the pressure is under $5x10^{-6}$ Torr. After the contact deposition, load the sample in the RTA610 and purge the N_2 for 10 minutes. Anneal the sample in N_2 environment for 1 minute at 400 °C. The backside electrode is completed. .
2. Then we need to generate the hard mask to protect the designed mesa-area from etching. First, clean the sample as mentioned before, then deposit 500 nm Si_3N_4 on p-type side GaAs surface with PECVD. Calibration of the Si_3N_4 film thickness is suggested before the deposition. Then follow the standard AZ5214 photoresist recipe to pattern the wafer with the right mesa areas. After that, load the wafer in the Fluorine-based ICP etcher and use SF_6 gas to etch into Si_3N_4. To avoid PR burning effect during the etching, attach some thermal conducting grease on the backside of the wafer and keep the processing temperature below 5^oC. Aim for a little bit over-etch to remove all the Si_3N_4 without PR protection. After the Si_3N_4 etching, the hard mask is completed by cleaning the residual PR. Follow the basic cleaning process to fully remove the PR.

3. With the protection of a Si_3N_4 hard mask, the mesa-area is protected during the chlorine-based ICP etching. While the Cl-ICP will also etches into Si_3N_4 with a slow etching rate, make sure the hard mask is thick enough to survive through the Cl-etching. Calibration of the etching rate is important in this step, we aim to etch slightly deeper than the active region to electrically isolate each device and minimize the ion bombardment. So for each device, based on the device structure, you need to calculate the etching depth before etching the device. After this step, use the F-CIP to remove the residual Si_3N_4, then the mesa area of each device is defined.
4. The last step is to deposit p-type electrode contact. First, pattern the top mesa area with negative PR, then rinse the device in diluted NH_4OH:DI water (1:10) and DI water for 30s respectively to create a fresh clean p-type GaAs surface. Load the sample into the e-beam evaporator as soon as possible to minimize the surface re-oxidation. When the chamber is pumping down to 10^{-7} Torr, deposit Ti/Pt/Au with 30/80/100 nm thickness. Providing enough cooling time between each metal deposition, especially between Pt and Au, the substrate will be heated up to 60^{o}C. After the metal deposition, follow the basic lift-off process to remove the PR and generate the contact pattern.
5. Package and wire bond the sample on chips for further test.

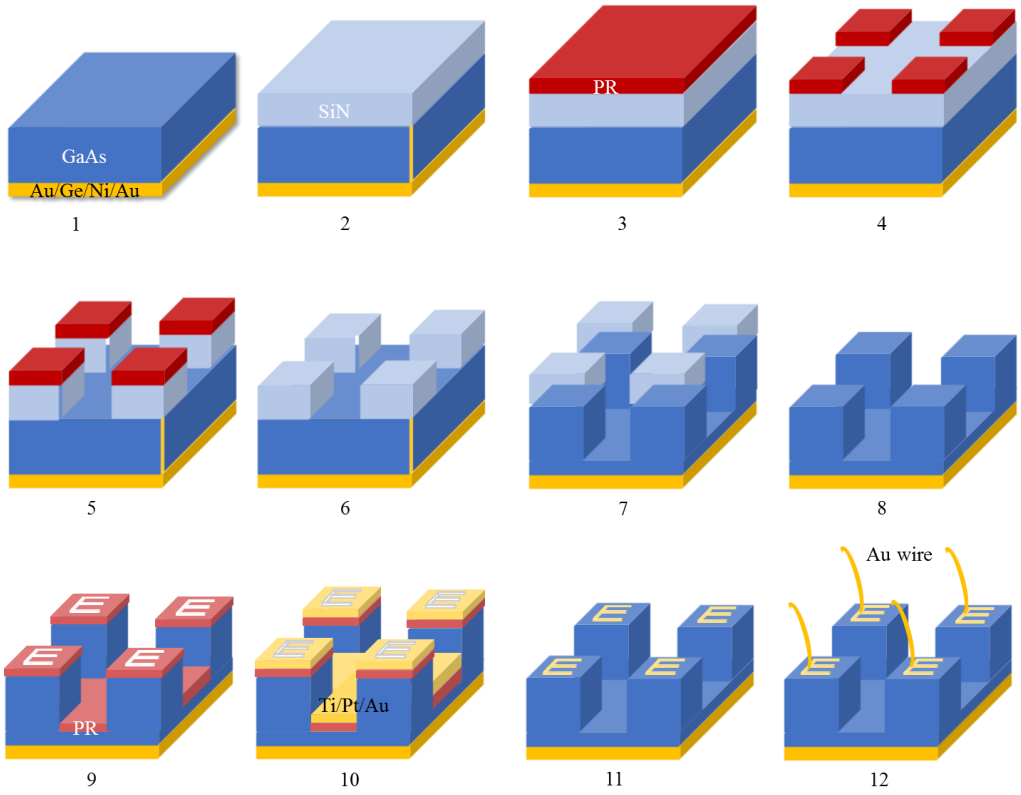

Figure 4.1 Illustration of the process flow of GaAs device: 1. Deposit Back contact Au/Ge/Ni/Au, 2. Grow Si_3N_4 hard mask, 3. Spin-coat photoresist (PR), 4. Develop PR pattern, 5. Etch Si_3N_4 to form mesa area mask, 6. Remove PR, 7. Etch down GaAs below active region, 8. Etch away Si_3N_4 mask, 9. Develop top contact pattern with negative PR, 10. Deposit top contact Ti/Pt/Au, 11. Lift-off top contact, 12. Package and wire bond

4.2 Overview of the Previous Results on InAs/GaAs Quantum Dot Solar Cell

In this section, I will introduce two main research results previously obtained on InAs/GaAs quantum dot solar cell by our group. One is the extraction of the extended

Urbach tail energy in the quantum dot system, another is the ultrahigh quantum dot saturation intensity obtained at room temperature.

4.2.1 Review of the Concept of Intermediate Band Solar Cell

The concept of intermediate band solar cell (IBSC) was introduced by Luque and Marti about 20 years ago [35]. The IBSC model aims to exceed the Shockley–Queisser limit for the energy conversion efficiency of a single junction photovoltaic cell by introducing an intermediate band energy level within the forbidden band, providing the possibility of absorbing sub-band gap photons and at the same time maintaining a high open circuit voltage. This intermediate band process increases the photocurrent and thereby increases the efficiency. In this theory, two sub-bandgap photon absorption is involved so that better coverage of the solar spectrum can be achieved to reduce the optical transmission loss. The limiting efficiency at full concentration in the intermediate band model was calculated to be 63%, which is much larger than the 41% theoretical efficiency limit of single junction solar cell at full concentration in the Shockley-Queisser limit [35].

The essence for the IBSC model is to form a stable intermediate band level to facilitate the two one-photon absorption processes which will contribute to the generation of one free electron-hole pair, and maintain the separation of the quasi-Fermi level of electrons and holes. Figure 4.2 shows the conceptual diagram for the intermediate band and the photon absorption processes involved. Ideally there will exist two ways to realize the photon absorption processes that will take an electron from the valence band and excite it to the conduction band. In one case, photons with above-bandgap energy excite the electrons from the valance band directly to the conduction

band. In the second case, two one-photon absorption processes are required: One sub-bandgap photon excites the electron from the valance band to the intermediate band level and another sub-bandgap photon sequentially excites the electron from the intermediate band level to the conduction band. Theoretically the intermediate band level won't affect the quasi-Fermi level of electrons and holes so that the open-circuit voltage remains unchanged. Though theoretically a huge energy conversion efficiency enhancement can be realized by the IBSC concept, so far no one has been able to demonstrate any efficiency enhancement using the intermediate band concept compared with the optimized solar cell with only one-photon absorption process. There are many limitations for practical application of the IBSC model. The introduced intermediate band greatly increases the non-recombination mechanism [64] and provides a carrier leakage path responsible for the open circuit degradation [65], it also requires partially filling the intermediate band to allow carrier movement to and from the intermediate band.

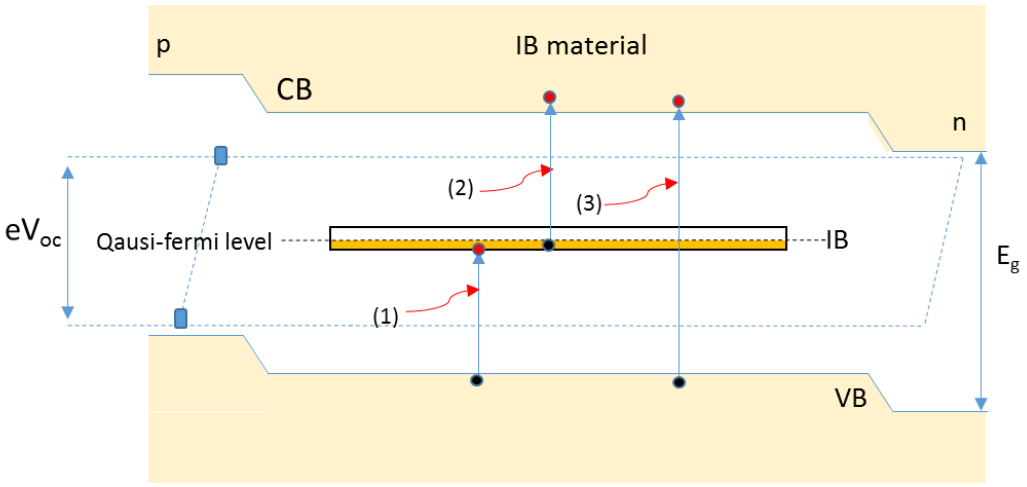

Figure 4.2 Conceptual diagram of the intermediate band model and the photon absorption process

The most frequent approach to implement the IBSC model is to utilize quantum dot (QD) confined states as the intermediate band. In our previous study, we use the InAs/GaAs and InGaAs/GaAs quantum dot systems and achieved 17.8% conversion efficiency [66] which is very close to the record of 18.7% [39], but it's still far from the 29.1% [33] obtained for bulk GaAs solar cell and not even close to the theoretical limit of 34.5% under 1 sun and 47% under concentration [34]. Generally people observe a slight enhancement of the short circuit current but with a much lower open circuit voltage. This phenomenon was successfully explained and proved by us through a model in which a single photon can be absorbed below the band gap due to the existence of an extended Urbach tail of states [65]. As shown in Figure 4.3, the continuum of states within the QDs forms an Urbach tail that allows below band gap photon absorption and provides a carrier escape path to the conduction minimum which equivalently lower the quasi-Fermi level of electron and reduce the open circuit voltage.

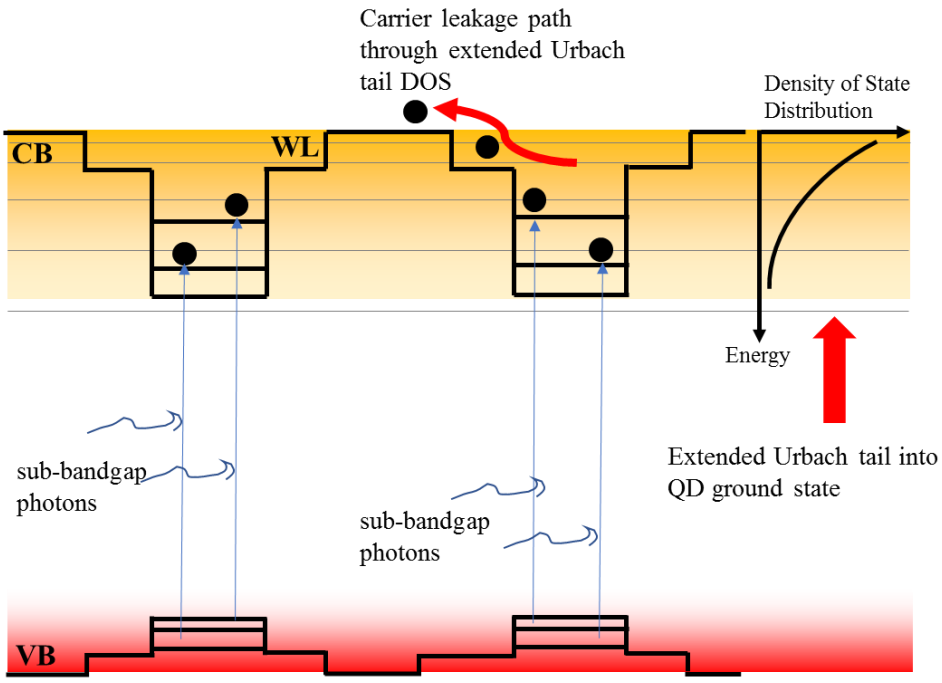

Figure 4.3 Energy diagram illustrating the exponential distribution of tailing density of states in the QDs region, the carriers excited by the sub-bandgap photons can escape through the extended Urbach tail

4.2.2 The Existence of Urbach Tail and the Derivation of the Tail Energy

The wave functions of the states in the quantum dot will overlap if the quantum dots spacing is less than 10 nm, at which case the intermediate states form a band. This is the key requirement of the implementation of intermediate band solar cell in quantum dot solar cell systems. On the other hand, we believe that there is another unfavorable effect that will occur when increasing the quantum dot concentration. The perturbation of the band energy by the deformation potential and the defect centers at QDs interfaces

will generate a tail of states extending from the conduction band edge into the band gap of InAs/GaAs QDs. This extending tailing state is the Urbach tail states[67-68], which is almost inevitable in the real QDs devices. The presence of InAs/GaAs QDs greatly disturb the perfect lattice periodicity of the GaAs, and thus lead to a broadening of the GaAs band edge. The Urbach tail states which superpose with the CB QDs states will provides a leakage pathway for the electrons that are confined in the QD states to the GaAs conduction band. This will in effect lower the CB quasi-Fermi level and lower the open-circuit voltage. This is consistent with the performance of the InAs/GaAs quantum dots solar cells where people observe the increase of the photocurrent together with a large reduction of the open-circuit voltage. Technically the Urbach tails also exist at the Valance Band, but due to the small VB offset between InAs and GaAs, the VB quantum dots states are thermally connected with the GaAs VB edge, which effectively lowered the VB.

In our InAs/GaAs QDSC's system, previously we observed a 5.5% improvement in the photocurrent density in the QDSC compared to a bulk GaAs solar cell. We have proven that this extra enhancement of the photocurrent is attributed to the below-bandgap wavelength photons absorption through the QD and wetting layer energy states and through the Urbach tail states. An external quantum efficiency measurement is performed to verify the sub-bandgap photocurrent generation. The absorption coefficient over a wide wavelength range below the GaAs bandgap is extracted to elucidate the different absorption mechanisms in the InAs/GaAs QDSC, as shown in Figure 4.4.

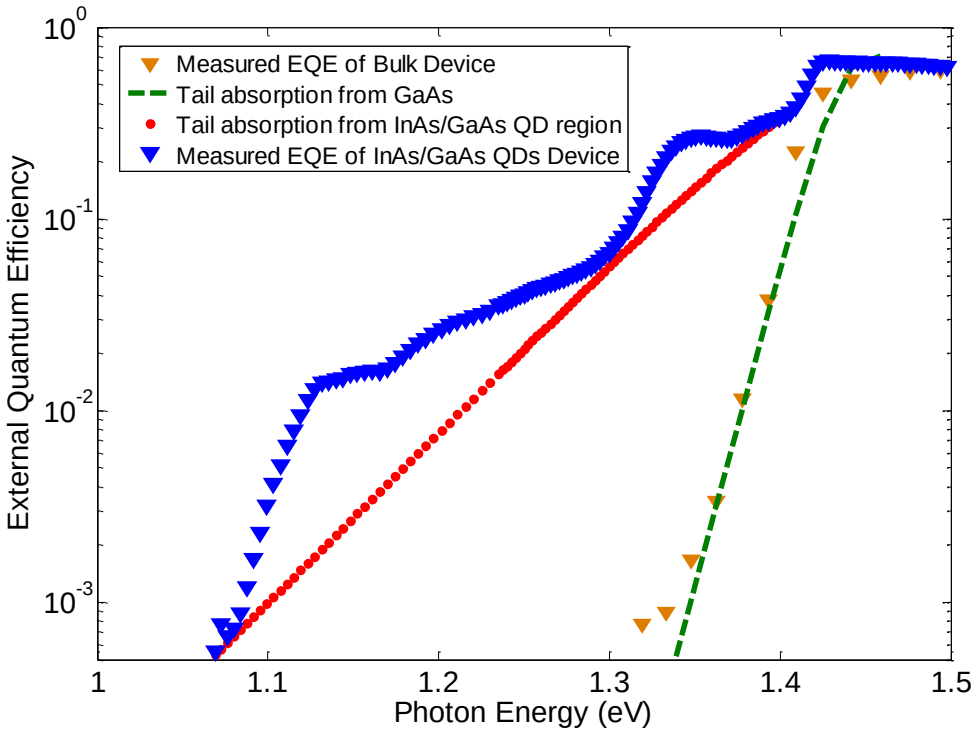

Figure 4.4 External quantum efficiency of GaAs/InAs quantum dot sample. The Urbach tail contributions for both devices are shown by the dotted lines. Note that the Urbach tail arising from the QD region has a much smaller slope than that for the bulk device, meaning a much higher characteristic width E_1 for the absorption edge. Absorption peaks corresponding to different size QDs or QD transition energies are observed.

The exponential distribution of the Urbach tail states lead to an absorption coefficient that varies with energy according to the following expression:

$$\alpha_{\text{Urbach}} = \alpha_0 \, e^{-\frac{E_g - \hbar\omega}{E_U}} \qquad 4.1$$

where E_U is the characteristic width of the Urbach absorption edge, and α_0 is a scaling parameter in units of cm^{-1} which is proportional to the amount of absorption. The relation between the EQE and the absorption coefficient can be derived as:

$$\eta_{ext} = (1 - R)(1 - e^{-\alpha L})\eta_{int} \qquad 4.2$$

where η_{ext} is the external quantum efficiency, η_{int} is the internal quantum efficiency, L is the layer thickness, R is the surface reflectivity, taken to be 0.3. When the absorption coefficient is sufficiently small as in the case of below-bandgap photon absorption, the above equation can be further simplified to:

$$\eta_{ext} = (1 - R)(\alpha L)\eta_{int} \quad 4.3$$

In general, the absorption process of below-bandgap photons occurs throughout the entire solar cell region where L is the film thickness. The linear dependence of the EQE and the below-bandgap absorption coefficient enables the derivation of the width of the absorption tail, assuming that the internal quantum efficiency is wavelength independent within the solar cell region.

In Figure 4.4. for a crystalline GaAs bulk device, the tailing energy states within the band mainly come from the intrinsic lattice disorder introduced by dopants. As shown by a green (color on-line) dashed line in Figure 4.4, the measured data can be fit with:

$$\eta_{ext} = 0.037\exp[-(1.39 - \hbar\omega)/0.013] \quad 4.4$$

An absorption width of 13 meV can be determined, which is consistent with previous measurements for p-type GaAs[69-70]. Typically a p-type GaAs layer has a higher absorption width than that of an intrinsic GaAs (~7 meV).

For a QD device, the absorption coefficient is affected by the QDs and WL energy states along with the Urbach tail energy states. Thus, the below-bandgap photocurrent is generated from three sources: the Urbach tail absorption and both the QD and WL absorption:

$$\eta_t = \eta_{Urbach} + \eta_{QD\&WL} \quad 4.5$$

η_t denotes the total measured EQE, which consists of the EQE contributed via Urbach tail absorption (η_{Urbach}), QDs and WL absorption ($\eta_{QD\&WL}$). When the incident photons have a lower energy than the QD ground state energies, they can only be absorbed via the tailing states that extend further into the mid gap. Therefore Urbach tail is fitted from 1.065 eV to 1.085 eV. The blue (color on-line) dashed curve connecting the reading from 1.085 eV to the band edge denotes the contribution of the Urbach tail in the semi-logarithmic plot of Fig. 4.4. The fitted Urbach tail absorption coefficient is shown below:

$$\alpha_{Urbach}\, L = -0.4 \times e^{-(1.424-\hbar\omega)/0.050} \qquad 4.6$$

The Urbach tail absorption width is found to be 50 meV, which is much larger than that for the bulk GaAs film. It is worthwhile to note that 50 meV is an average value of the local broadening created by InAs QDs, under the condition that the QDs are uniformly distributed in the 2000 nm intrinsic region of the host material.

4.2.3 Room Temperature On-resonance Z-scan Results

To investigate the intermediate band two-photon absorption contribution to the photocurrent enhancement, we have previously demonstrated a method to study the non-linear properties in QDSC for on-resonant excitation which evaluates the 2PA carrier generation efficiency and the absorption saturation effect of the QDs [71]. The evaluated sample has 40 layers of InAs/GaAs self-assembled quantum dots grown by the Stranski-Krastanow method with an inter-dot layer spacing of 50 nm, the in-plane QD density was measured to be 3.8 x 10^{10}/cm^2. The measured absorption profile for the QDs sample shows a Gaussian line-shape with an inhomogeneous linewidth of 25

meV, which we believe is due to the slight size variation and change in the environment of the QDs [65]. As we know, the QDs can play a role as a saturable absorber. In order to evaluate the sub-bandgap photon-carrier transition and account for the QD saturation, we have proposed a precisely controlled characterization method to investigate the QDs absorption saturation effect with an on-resonant excitation condition. The photocurrent of the QD sample comes from both background two-photon absorption (2PA) process and one-photon absorption (1PA). As shown in Figure 4.5, the background 2PA process involves a first transition from a state in valence band to a virtual state below the conduction band minimum and a second transition to a state in the conduction band as a hot carrier. The 1PA process involves one transition from a state in valence band to the ground state of QDs, and then leaks to the conduction band through an extended Urbach tail without a second photon absorption, the QD saturation effect cannot be neglected when the on-resonant excitation intensity is close to the saturation intensity (where the population density in the QD ground state approaches the QD density).

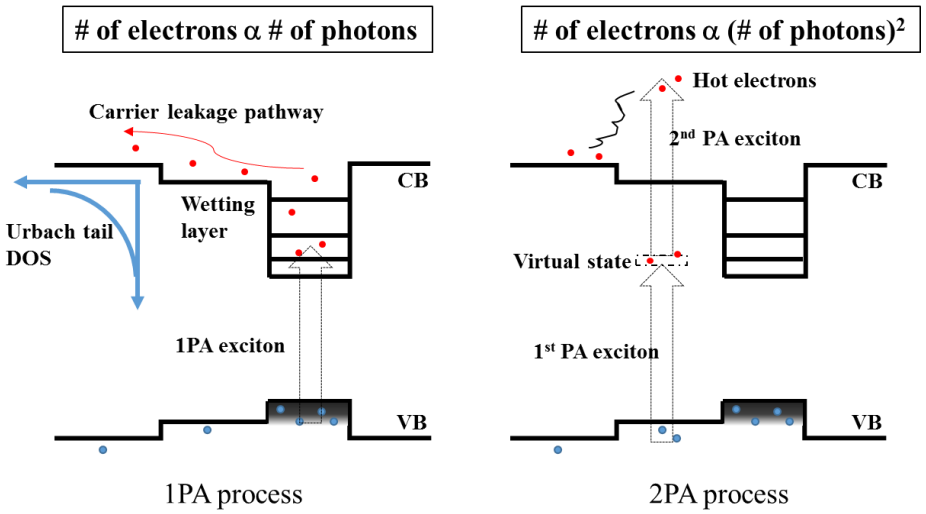

Figure 4.5 A sub-bandgap photon generates an electron on the energy states within the gap. 1PA process (left): the free electron leaks to the matrix via continuum Urbach tailing states. 2PA process (right): the free electron is excited again by a sequential absorption of another sub-bandgap photon becoming a hot carrier above the conduction band

Since the QD ground state transition is measured to be around 1.06 μm, we used a single transverse mode pigtailed laser (Thorlabs LPS-1060-FC) with 1.06 μm wavelength to excite the QD sample. The laser beam was collimated and then focused to a beam waist of 1.0 μm. The output power is calibrated with an unbiased Ge detector. The quantum dot solar cell is mounted perpendicularly to the beam on a three-dimensional stage with motorized actuators from Newport Corporation. The photocurrent is read with a Newport 6487 Pico-ammeter. We introduced the z-scan technique [72] to evaluate the non-linear opto-electronic measurement and we also

constructed a 2PA model to support our measurements. The focused laser beam follows a Gaussian intensity profile:

$$I(r,z) = I_0 \left(\frac{w_0}{w(z)} \right)^2 e^{-\frac{2r^2}{w(z)^2}} \tag{4.7}$$

$$w(z) = w_0 \sqrt{1 + \left(\frac{z}{z_0} \right)^2} \tag{4.8}$$

where I_0 is the intensity at z = z_0, w_0 is the beam waist and z_0 is the Rayleigh range. The measured intensity dependent photocurrent in our experiments is just simply a sum of 1PA current or 1SAT current due to QD saturation effect, and a background 2PA current.

$$i_{total} = i_{1SAT} + i_{2PA} \tag{4.9}$$

As the excitation intensity increases, the QDs act as saturable absorber, the dephasing time of the transition to the ground state quantum dots has previously been measured to be about 200fs at room-temperature [73-74]. This leads to a homogeneous linewidth of about 6 meV, while a linewidth of 25 meV due to the QD size variation was previously derived from our external quantum efficiency measurement of the QD sample [65], we could conclude that the 1PA transition is mostly inhomogeneously broadened. Thus the I_{SAT} term can be expressed as [75]:

$$i_{1SAT} = a \int_0^\infty \frac{I(r,z)}{\sqrt{1 + \frac{I(r,z)}{I_S}}} 2\pi r dr = a \int_0^\infty \frac{I_0 \left[\frac{w_0}{w(z)} \right]^2 e^{-\frac{2r^2}{w(z)^2}}}{\sqrt{1 + \frac{I_0 \left[\frac{w_0}{w(z)} \right]^2 e^{-\frac{2r^2}{w(z)^2}}}{I_S}}} 2\pi r dr \tag{4.10}$$

$$i_{1SAT}(z) = a\pi I_s (w(z))^2 \left(\sqrt{\frac{I_0}{I_s}\left(\frac{w_0}{w(z)}\right)^2 + 1} - 1 \right) \qquad 4.11$$

In equation 4.11, a is a proportionality constant between the generated photocurrent and a low optical power on the sample. I_s is the saturation intensity which is required to excite half of QD population with an electron that occupies the conduction band QD ground state, it can be expressed as [75]:

$$I_s = \left(\frac{4\pi^2 n^2 hc}{T/T_1 \lambda^3} \right) \Delta\upsilon \qquad 4.12$$

where n is the index of refraction of the sample, h is the Planck constant, c is the speed of light, λ is the wavelength of light, $\Delta\upsilon$ is the FWHM of the homogeneous absorption profile and is given by $\Delta\upsilon = 1/\pi T_2$, where T_2 is the dephasing time, T_1 is the radiative lifetime, and T is the quantum dot lifetime. The background 2PA term has a quadratic dependence on the beam power, and can be expressed as [76]:

$$i_{2PA} = b\int_0^\infty \left[I(r,z)\right]^2 2\pi r dr = \frac{\pi}{4} b \frac{z_0^{\,2} I_0^{\,2} W_0^{\,2}}{z_0^{\,2} + z^2} \qquad 4.13$$

where b is a constant to measure the efficiency of 2PA process.

The measured photocurrent vs z-scan direction for 1.06um wavelength on-resonant excitation under different input optical power is shown in Figure 4.6. As stated before, the measured photocurrent consists of a background non-resonant 2PA photocurrent and a 1PA photocurrent due QD absorption saturation on an inhomogeneous broadened transition. We derived the saturation intensity by fitting the measured photocurrent vs z plot with the sum of equation 4.11 and 4.13. This fitting yields a saturation intensity as high as 10 mW/μm2. And by using equation 4.12, taking T_1 = 1ns [77], T_2 = 200fs,

n = 3.5, we could extract the quantum dot lifetime T to be 12.9ps which is much less than the extrapolated value of T at room temperature [78]. We believe this can be explained by the thermal emission of carriers out of the dots through extended wetting layer states or Urbach tails [79-80]. The fitted 2PA constant b as 45 nA·μm^2/mW^2. The 2PA coefficient β_{2PA} can be derived by the following equation:

$$b = \beta_{2PA} \times L \times R \tag{4.14}$$

where L is the effective thickness of the absorption region and R is the responsivity factor for 1.06 μm (1.17 eV), if assuming 100% internal quantum efficiency, R can be calculated as:

$$R = \frac{e}{2 \times 1.17eV} \eta_{\text{int}} = \frac{e}{2 \times 1.17eV} = 4.27 \times 10^5 \frac{nA}{mW} \tag{4.15}$$

$$\beta_{2PA} = \frac{b}{L \times R} = 5.27 \times 10^3 cm/GW \tag{4.16}$$

The factor 2 in the denominator means two 1.06 μm photons generate one electron-hole pair. The background two-photon absorption coefficient of $5.27 \times 10^3 cm/GW$ is about 240 times larger than the reported value for bulk GaAs measured at 1.06 μm [81-82]. In Figure 16, each sub-plots show the original measured photocurrent data with triangle marks and the fitted i_{1SAT} term with green dashed line and i_{2PA} term with pink dashed line based on the derived Is and b respectively. The blue line is the sum of fitted i_{1SAT} and i_{2PA} which perfectly overlaps with the measured photocurrent under different input optical power. This validates the two main non-linear components (saturate effect and 2PA component) in the on-resonant QDSC model.

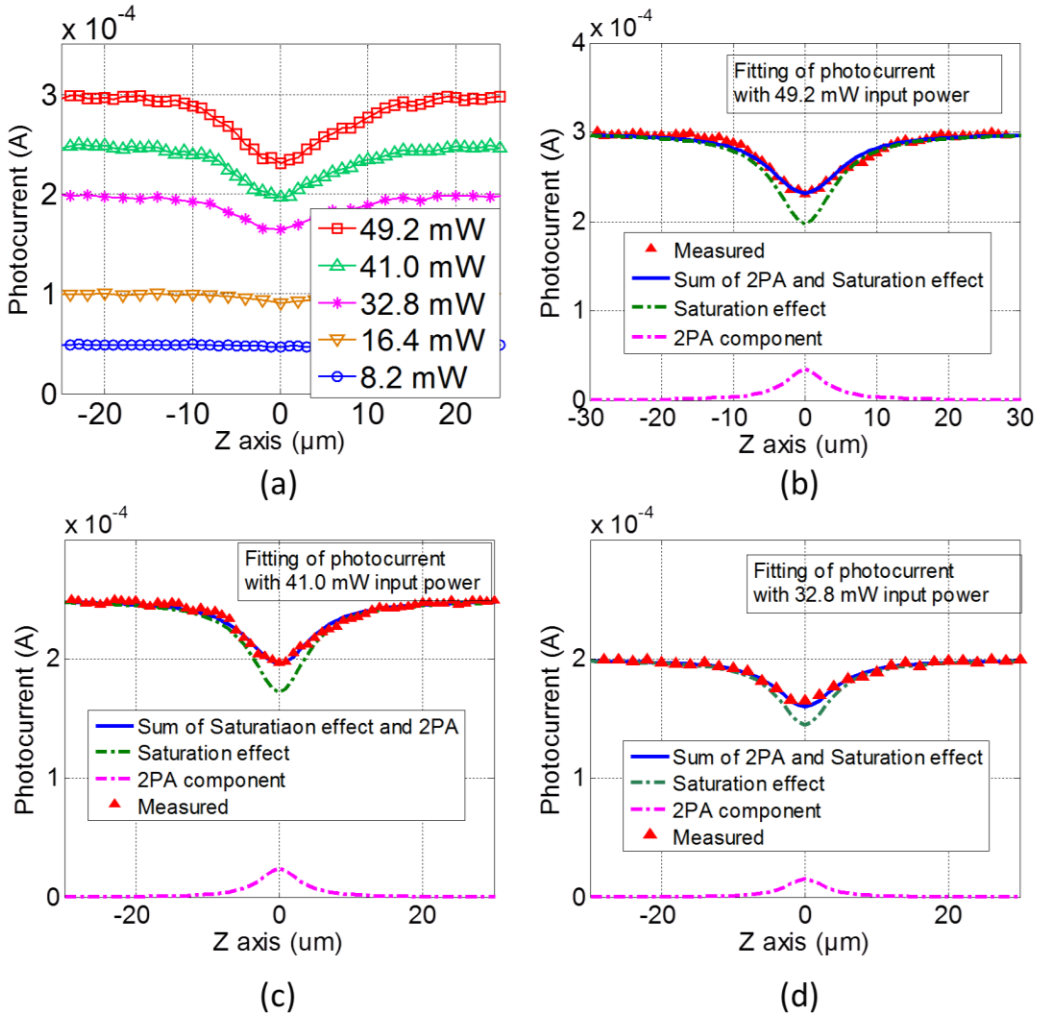

Figure 4.6 (a) Photocurrent vs z-scan direction for 1.06 μm wavelength on-resonant excitation under different input optical power. (b)(c)(d) A comparison between fitted curve and measured data with 49.2 mW, 41.0 mW and 32.8mW input power. A saturation current density of 10 mW/ μm^2 was fitted under all input powers.

The fitted saturation intensity I_s is 10 mW/μm^2 = 10^6 W/cm^2, which is about 10^7 times larger than the unfocused sun intensity (~0.1 W/cm^2) and still much higher than the maximum concentrated sun intensity (×46,000). For intensity much lower than I_s, the amount of excited population in the intermediate state is proportional to I/I_s. This means

that when the solar cell is illuminated under one sun intensity, only 10^{-7} of the quantum dot population is excited over a bandwidth corresponding to the homogeneous absorption linewidth. While the absorption profile is inhomogeneously broadened due to the quantum dot size variation, and the inhomogeneous linewidth (25 meV) is about 4 times larger than homogeneous linewidth (6 meV), so $4x10^{-7}$ of the quantum dot population can be excited to the QD ground state. The saturation intensity for the second transition (quantum dot inter-band transition) has previously been measured to be about $4x10^5$ W/cm^2 ($4x10^6$ times larger than one sun intensity) [83-84], and if we consider similar inhomogeneous broadening ratio, then only $4x10^{-13}$ of the quantum dot population can be excited to the final state. Previously we've evaluated 0.8% of the band-to-band contribution to the photocurrent comes from single photon transition to the GD ground state, then the percentage of the photocurrent generated through the second photon transition through intermediate state compared to the band-to-band photocurrent is $[0.8\% \div (4 \times 10^6)] \times 4 = 8 \times 10^{-7}\%$, which is negligible. Thus we can conclude that at room temperature and one sun illumination, the transition rates between inter-band states are extremely small and will definitely not improve the conversion efficiency significantly. By cooling down to cryogenic temperatures, one can reduce the saturation intensities of both transitions involved with the intermediate state, and the dephasing time can approach two times the intrinsic quantum dot lifetime and might lead to some enhancement of the cell conversion efficiency. The quantum dot lifetime can be made to approach the radiative lifetime by operating at low temperatures.

4.3 Experiments at Cryogenic Temperatures

In this section, I will introduce our closed-cycle liquid helium cryo-cooler system and the corresponding set-up for our experiments and then focus on discussing the on-resonance z-scan measurements of the QDSC sample at different temperatures.

4.3.1 Cryocooler Components and Experimental Set-up

The cryocooler system is from Advanced Research Systems with model number CS204SI-DMX-1-SS. The system includes the following components:

TABLE IV
COMPONENTS OF ARS CRYOCOOLER SYSTEMS

Item Name	Model & Description	Qty
Cryocooler	DE-204SI, 4.2K-350K	1
Helium Compressor	ARS-4HW, water cooled, 208-230 V, 60 Hz	1
CoolPac	CP-4, 3.9 kW of Cooling Capacity	1
Helium Hoses	HH-SF-5-10, 1set, 10feet long	1
Vacuum Shroud	DMX-1-SS, 5 window ports for optical access	1
Radiation Shield	RSD-1-CU, 2 holes, 90 degree apart	1
Radiation Shield	RSD-1-CC, 2 holes, 180 degree apart	1
Sample Holder	SHE-18, 2-56 tapped hole for sample sensor mount	1
Optical Windows	W-X1-CAF, Calcium Fluoride	2
Optical Windows,	W-X1-HPQ, High Purity Quartz	2

Electrical Feedthroughts	W-INST-1, 6 copper wires installed with free length	1
Integrated Lakeshore Temperature Controller	LS-335, Two sensor inputs, 75 W total heater power	1
Vacuum Pumping System	VPS-2(Adixen 2015SD), Two stage mechanical pump	1
Horizontal Stand	Prototype STND-204-1, self-made with Aluminum	1

Here I will briefly introduce the installation of the cryocooler system in our lab:

1. Unpack and inspect the equipment in case of any shipping damages. Check the Tip-N-Tell indicator on rear panel of the compressor to determine if the package was tilted too much.

2. Check the compressor gas supply pressure gauge. The static pressure should be 200-205 psig (1379 -1413 kPa) @ 19-25^{o}C. If the pressure is only slightly low, it may be an indication of shipping damage. In that case, let the unit set at room temperature for an hour and re-check.

3. If the pressure remains low, but is stable, then add gas per the Maintenance. Monitor the gauge for any further pressure loss.

4. If the pressure continues to decrease, contact ARS Inc. for service.

5. Secure the expander on the self-made aluminum stands and lock the stands on the optical table as shown in Figure 4.7.

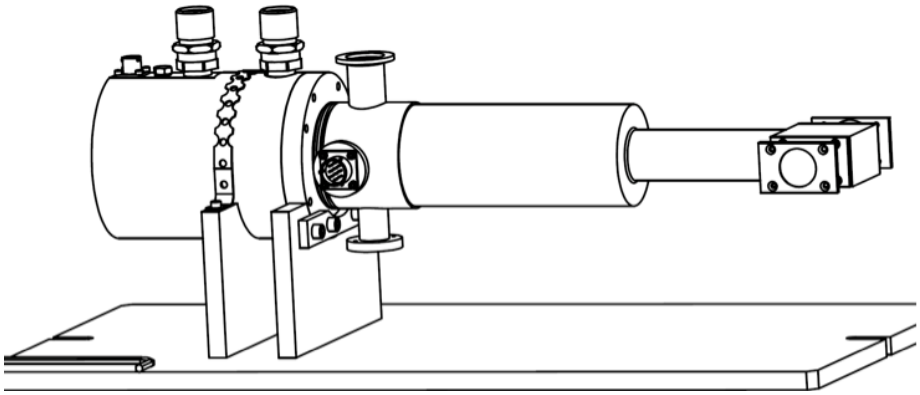

Figure 4.7 Cryocooler expander secured on the stands

6. Attach the accessories to the expander (radiation shrouds, sample holders, vacuum shrouds).

7. Locate the compressor near the expander, leave enough room for the 10 feet long helium hoses.

8. Connect the gas lines to the compressor and expander:

9. Connect one gas line to the supply gas couplings at the compressor and expander (red)

10. Connect the other gas line to the return gas couplings at the compressor and expander (green).

11. Use two wrenches to hold and turn the gas line coupling (female) where shown. Turn until tight.

12. Connect the expander electrical power cable to the compressor and expander receptacles.

13. Install the CoolPac Cooling System as shown in Figure 4.8. Check Appendix for the detail installation guide for the CoolPac.

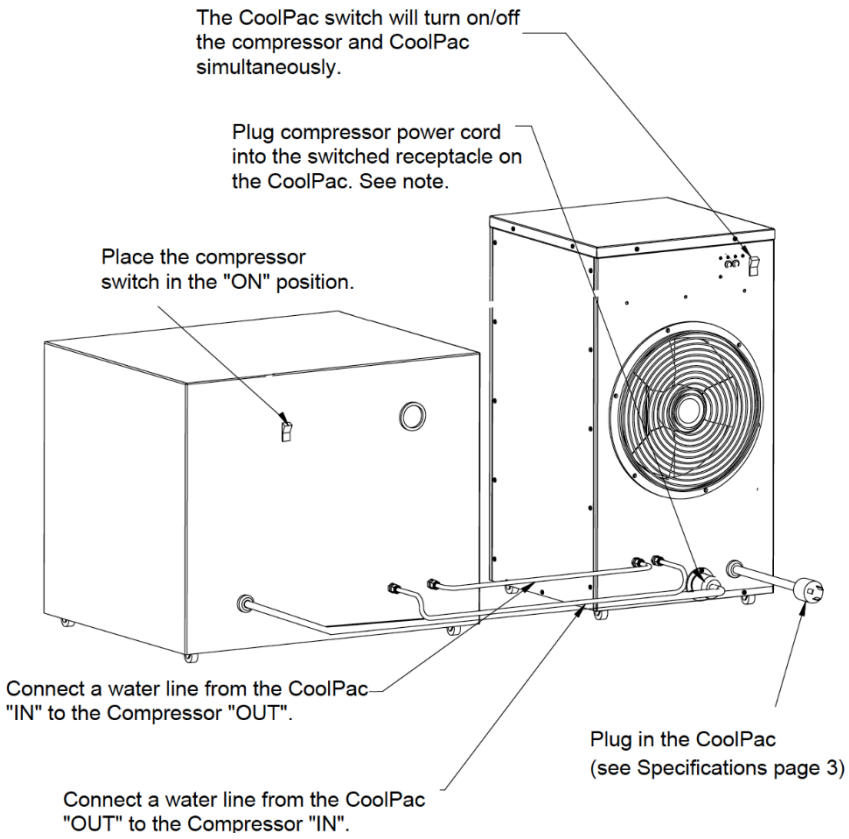

Figure 4.8 CoolPac system connected to the compressor

14. Verify the compressor on/off switch is turned off. Connect the proper electrical power to the compressor power cord via a suitable connector. In our case, plug the compressor power cord into the receptacle on the front of the CoolPac.

15. Connect the vacuum system (capable of achieving < 0.01 torr), isolated by a vacuum valve, to the pump-out port provided on the expander skirt.

16. Figure 4.9(a) shows the schematic of the final set-up of the cryocooler system, and Figure 4.9(b) is the image of the real cryocooler systems installed in our lab.

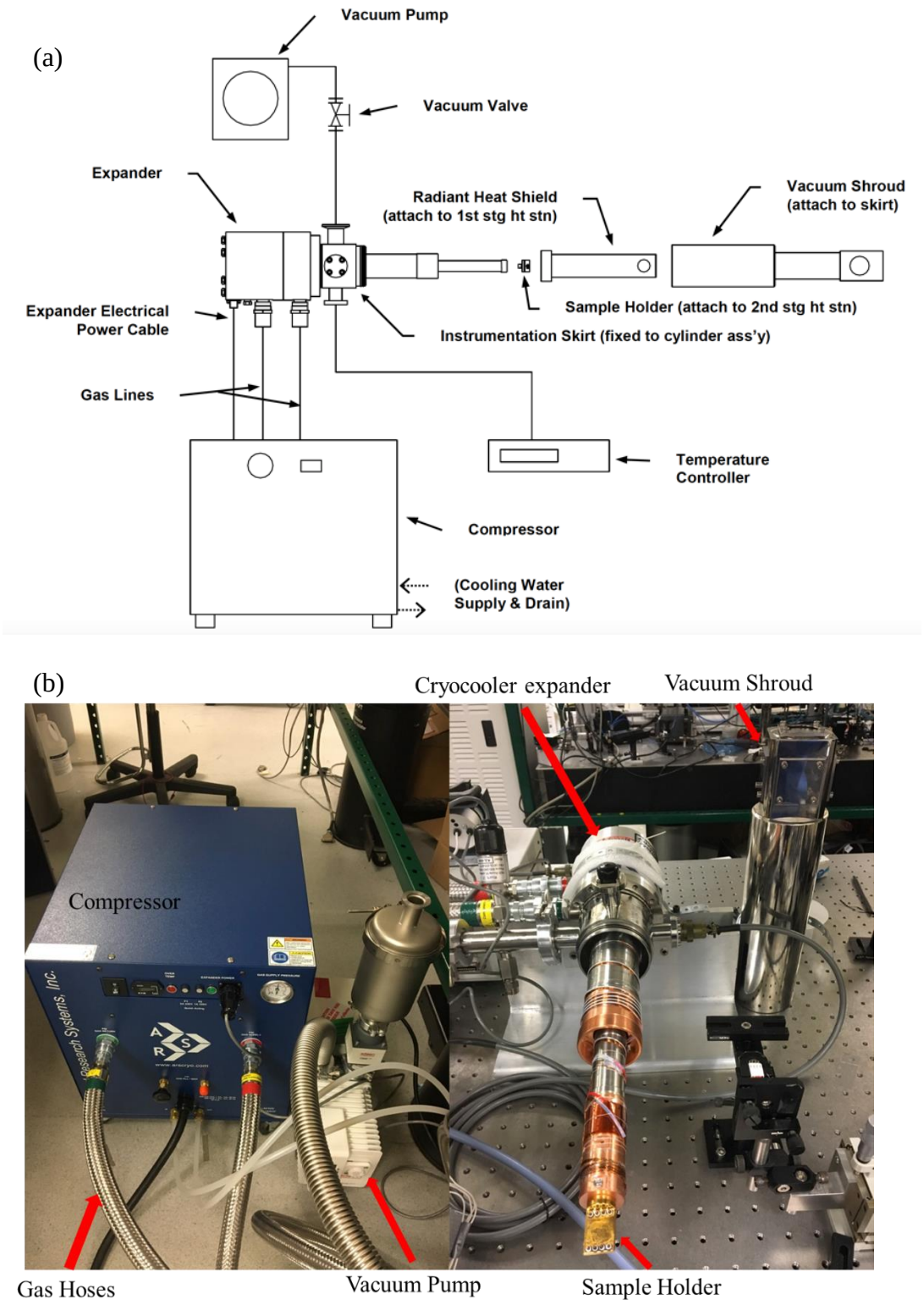

Figure 4.9 (a). The schematic diagram of the final set-up compressor and expander, (b) The LH compressor and vacuum pump (left) and the cryocooler expander secured on the stands (right).

To operate this system, I summarize the standard procedure of operation as follows:

1. Verify that the equalization pressure on the compressor pressure gauge meets the requirement listed on the compressor and/or in the compressor manual. If the pressure is below the minimum, then add helium gas in the manner described in the compressor manual (use only 99.999% ultra-pure helium, dew point < -50^{o}C at 300 psig (2069 kPa)).

2. Evacuate the expander vacuum shroud or enclosure to < 0.1 torr.

3. Close the vacuum valve.

4. Turn on the vacuum pump.

5. Slowly open the vacuum valve.

6. The expander can be started with an insulating vacuum pressure of < 0.1 torr.

7. Turn on the compressor, and turn on the cooling water to the compressor. The expander will begin to cool down. The noise from the expander should be a regular beat at a frequency approximately 2X the frequency of the electrical supply power.

8. Close the vacuum valve when the vacuum pressure remains < 0.01 torr or the expander has cooled to 150 - 200K.

9. After reaching the minimum temperature (7-8K in our case), adjust the required temperature with the Lakeshore Model 335 Temperature Controller.

10. To stop operation, turn off the compressor and turn off the cooling water.

4.3.2 Photoluminescence Measurement at Cryogenic Temperatures

In order to determine the laser wavelength required for on-resonant excitation of the InAs/GaAs QDSC at cryogenic temperatures, we have measured the photoluminescence (PL) of the QDSC to extract the quantum dot energy spectra at various temperatures from 8K to 293K. (The experimental set-up is shown in Figure 4.10. The QD sample is attached in the cryostat expander. A 637 nm laser beam is collimated and hit on the sample surface through a confocal lens system. The collected PL is guided into a spectrometer through a two-mirror system. The output PL signal is phase-locked with a 207 Hz chopper and detected by a Ge photodetector. The photocurrent is amplified with a Stanford Research SR570 pre-amplifier and read with a Stanford Research SR830 lock-in amplifier.

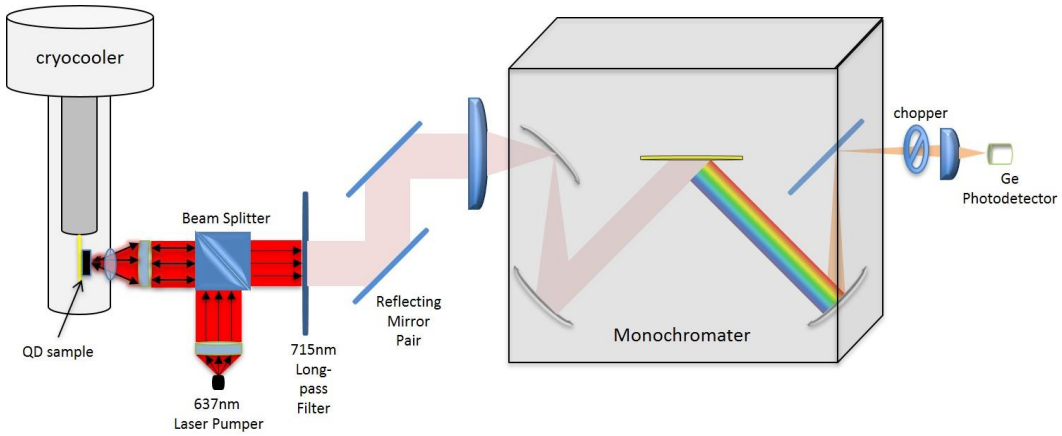

Figure 4.10 The set-up used for measuring the temperature dependent photoluminescence

The measured temperature dependent PL response of the InAs/GaAs QDSC is shown in Figure 4.11 (a), we have normalized all PL spectra and have plotted them on one set of axis. It is important to notice that there are several PL peaks in the PL spectra, which correspond to different carrier relaxation paths, for example from GaAs conduction band to valance band. What we are interested in is the PL peak centered on the QD ground state energy. Thus the PL measurement system is tuned to focus on the lower part of the PL energy range (~1.1 eV to 1.4 eV). We can see from Figure 4.11 (a) that the PL spectrum shifts toward higher energy with decreasing temperature. The PL spectrum almost maintains its shape till below 145K, another obvious peak position is observed at higher energy position. The PL spectra correspond to the carrier relaxation from QDs ground state and also from higher QD energy states within the quantum dots with different sizes. At low temperature, the PL line-shape is determined by the inhomogeneous distribution of QD sizes and the emission of light from higher energy states within a quantum dot. When the temperature is high enough, the effect of electron-LO-phonon scattering is progressively becoming dominant, the carriers in the higher QD energy states can be easily scattered to the QD ground state, thus the second emission peaks is not significant at higher temperature range.

The main PL peak energy position and its FWHM at different temperature are derived after fitting the PL spectrum with two Gaussian shapes. We choose the lower energy one as the main peak since it is dominant at high temperatures, indicating the QDs ground state energy position. Figure 4.11 (b) shows the temperature dependence of QDs PL main peak positions. The temperature-dependent energy shift follows the Varshni's formula:

$$E(T) = E(0) - AT^2/(T + B) \qquad 4.17$$

By fitting this equation, we can derive A = 0.0005386 eVK^{-2}, B = 219.9K, E(0) = 1.206 eV. Figure 4.11 (c) presents the temperature dependence of the main peak's FWHM. It's observed that the FWHM decreases slowly from 8K to 150K, and then start increasing again due to the electron-phonon scattering as the temperature keeps on increasing. Dai and Lin, et al explained this unusual behavior at low temperature qualitatively in 1997 [85]. At low temperature range, the exited carriers will be gradually thermalized in the QDs as the temperature increases. The thermalized carriers can repopulate in the quantum dots, this repopulation process will occur more frequently for predominant quantum dot sizes since the dot sizes follow a Gaussian distribution.

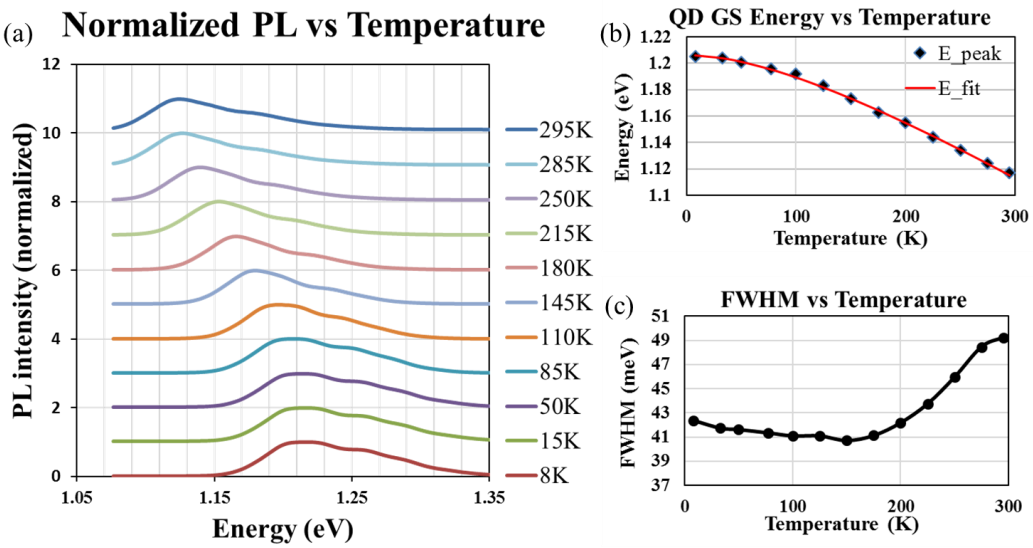

Figure 4.11 (a) Temperature dependent PL spectral of InAs/GaAs QD solar cell, (b) Temperature dependence of Main QD PL peak energy and the fit by Varshni's Equation, (c) Temperature dependence of the main QD PL peak FWHM

4.3.3 On-Resonance Z-scan Measurement at Cryogenic Temperatures and Result Analysis

To investigate the IB 2PA contribution to the photocurrent enhancement, we have previously demonstrated a method to evaluate the 2PA carrier generation efficiency and the absorption saturation effect of the QDs at room temperature [71]. The studied sample has 40 layers of InAs/GaAs self-assembled quantum dots grown by the Stranski-Krastanov method with an inter-dot layer spacing of 50 nm, the in-plane QD density was measured to be 3.8 x 10^{10} cm^{-2}. The wafer was cleaved in to small size (2x2 mm^2) and fabricated with back side n-type Au/Ge/Ni/Au electrode and top p-type Ti/Pt/Au interdigitated figure-shaped electrode. In order to observe the nonlinear optical transitions via the intermediate states, high intensity excitation beams with different wavelengths were used. We assumed that the QDs can be described as a saturable absorber. In order to evaluate the sub-bandgap photon-carrier transition and account for the QD saturation effect at cryogenic temperatures, we upgraded our apparatus for near on-resonance excitation and for the cooling of our sample using an ARS-DE 204 closed-cycle liquid helium cryocooler system. As shown in Figure 4.12 (a), the sample is held on the sample holder inside the vacuum shroud of the cryocooler. The fiber-coupled pigtail laser served as the excitation source and was mounted perpendicular to the sample on a motorized three-dimensional stage. The laser beam is collimated and focused down to a 2 μm spot size ($1/e^2$ diameter) at the focal point. To minimize the local thermal effect of the QD sample, the laser is modulated using Newport LDP-3830 pulsed laser driver with 75ns pulse at 0.01% duty cycle. The detected photocurrent is integrated with an SRS200 series Boxcar Averager and read

by a Keithley 2400 Sourcemeter. When the laser moves along the light propagation direction, the incident intensity profile changes accordingly. This modified z-scan set-up will evaluate the QDSC's photocurrent dependence on beam intensity at different temperatures.

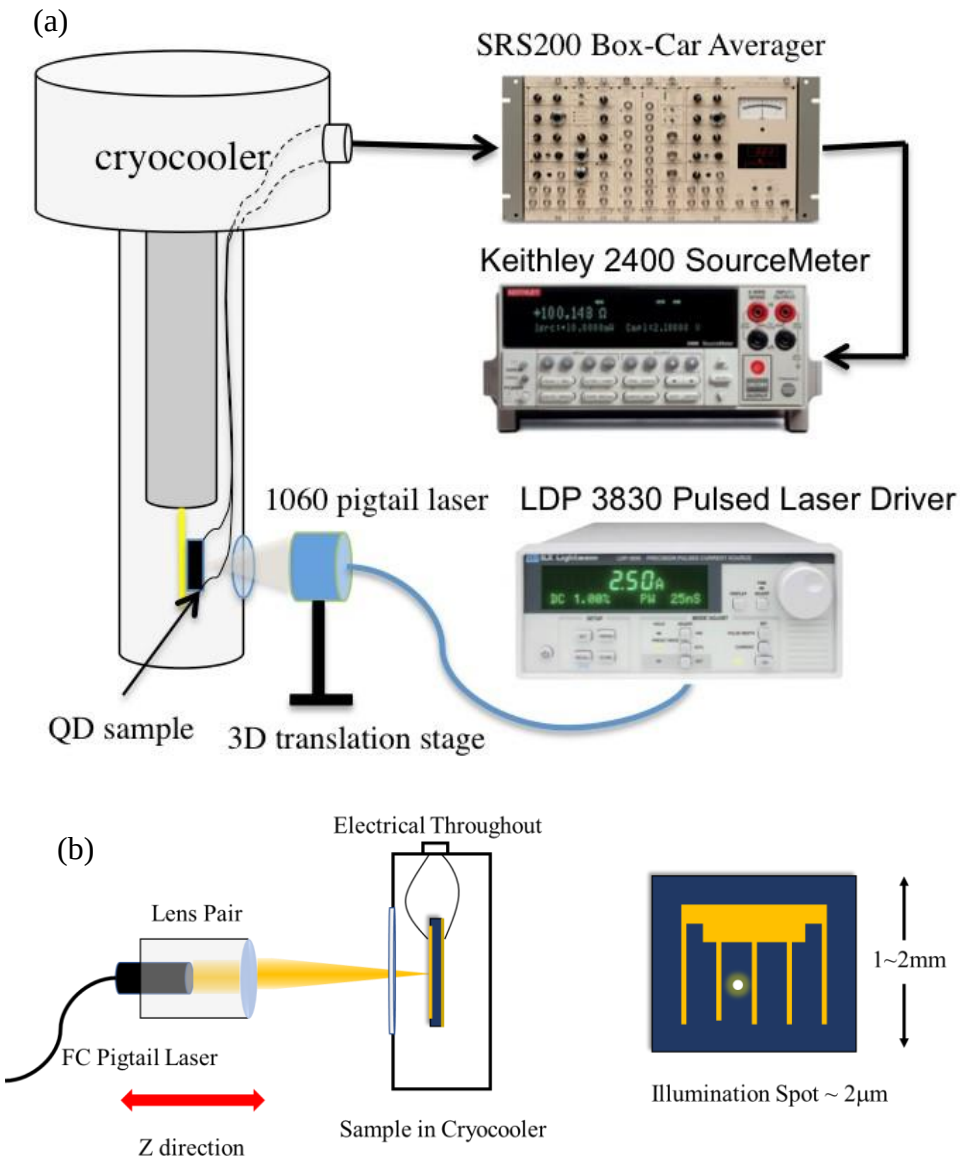

Figure 4.12 (a) The modified z-scan measurement system using a cryocooler system, (b) illustration of the z-scan technique that uses a 2 μm spot size on the QDs sample

Previously we have presented a model to explain the nonlinear optical interaction with QDs using an on-resonance z-scan measurement technique at room temperature. The photocurrent of the QDSC comes from both a background 2PA process and a saturated one-photon absorption process (1_{SAT}). The background 2PA process involves a first transition from a state in the valence band to a virtual state below the conduction band minimum and a second transition to a state in the conduction band as a hot carrier. The 1_{SAT} process involves one transition from a state in the VB to the GS of the QDs, and then the excited electron leaks to the CB through an extended Urbach tail [65] without a second photon absorption. We stress that the saturation effect cannot be neglected when the on-resonant excitation intensity is close to the QD saturation intensity. According to our model, the measured photocurrent can be expressed as:

$$i = i_{SAT} + i_{2PA} = a\pi I_s\big(w(z)\big)^2\left(\sqrt{\frac{I_0}{I_2}\left(\frac{w_0}{w(z)}\right)^2 + 1} - 1\right) + \frac{\pi}{4} b \frac{{z_0}^2 {I_0}^2 {w_0}^2}{{z_0}^2 + z^2} \qquad 4.18$$

In the above equation, a and b are proportionality constants between the generated photocurrent and the optical power on the sample, w(z), w_0 and z_0 are Gaussian beam parameters, I_s the saturation intensity which is required to excite half of QD population with an electron that occupies the QD ground state.

We selected a 1064nm (1.165 eV) laser to excite the QDSC in our on-resonance z-scan experiment, covering the temperature range from 293K to 170K. Here I have measured two quantum dot samples, one that was prepared in 2015 by Dr. Li, named QD2015, and another one that was recently fabricated in the early 2019 with the same solar cell structure as for the old sample, named QD2019.

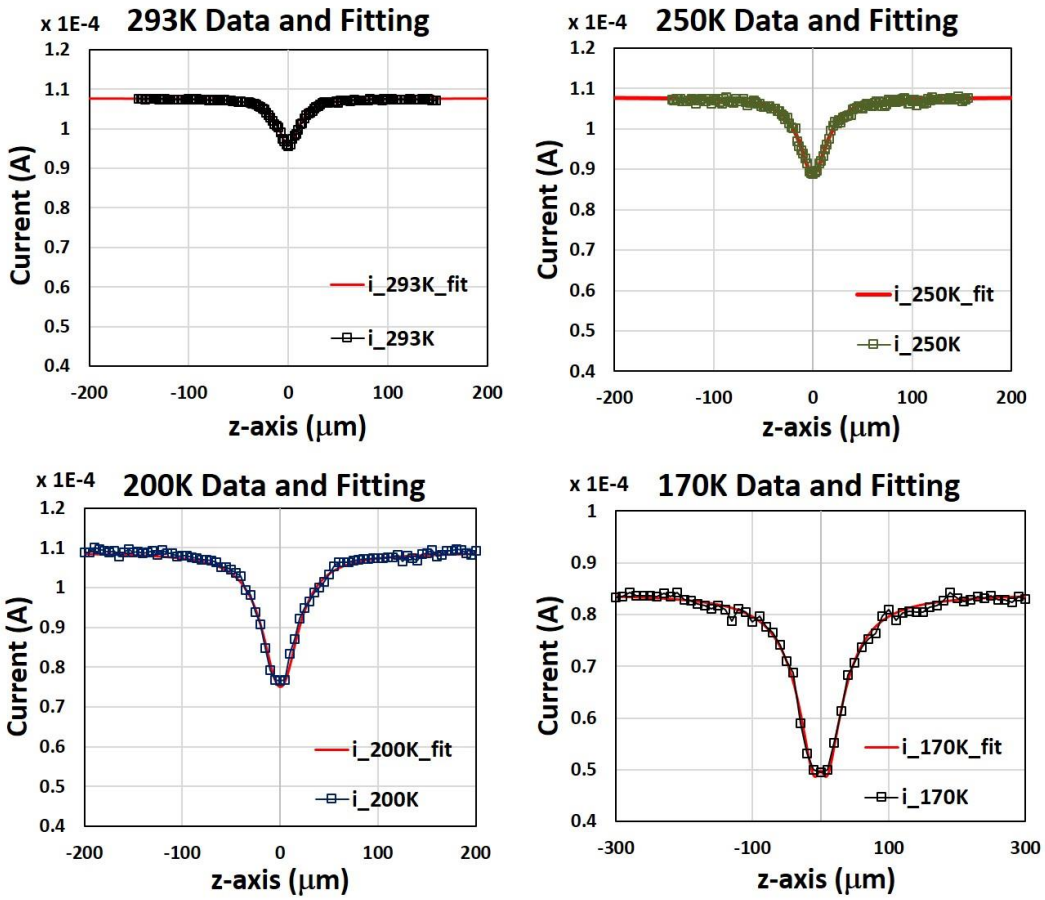

Figure 4.13 QD2015's photocurrent and the fitting curves in the z-scan measurements at 293K, 250K, 200K and 170K.

Figure 4.13 shows four photocurrent plots of the z-scan measurement at different temperatures for QD2015. Each plot shows both the experimental data and the fitting curve base on Equation 4.18. The photocurrent reading is a combined effect of 2PA photo-generation and absorption saturation based on an inhomogeneous broadened transition. The saturation intensity was obtained by fitting Equation 4.18 to the measured photocurrent along the z direction. The fitting curves perfectly match the experimental data, indicating the accuracy of our physical model at low temperatures.

The extracted fitting parameters are listed in Table 5. Superscript 1 denotes the fitting parameters of QD2015, superscript 2 denotes the fitting parameters of QD2019.

Table V
SUMMARY OF FITTING PARAMETERS

Temp (K)	a^1 (A/W)	b^1 ($A*cm^2/W^2$)	I_s^1 (mW/m^2)	a^2 (A/W)	b^2 ($A*cm^2/W^2$)	I_s^2 (mW/m^2)
170	8.57E-6	2.42E-6	0.0857	3.88E-06	5.13E-07	0.0381
180	9.92E-6	2.06E-6	0.131	4.45E-06	6.02E-07	0.0675
200	1.11E-5	1.39E-6	0.338	5.80E-06	5.94E-07	0.174
220	1.08E-5	8.82E-7	0.485	6.30E-06	6.02E-07	0.330
250	1.10E-5	9.65E-7	0.928	6.50E-06	4.54E-07	0.901
293	1.10E-5	1.86E-7	2.501	6.66E-06	1.05E-07	2.905

Superscript 1 denotes the fitting parameters of QD2015, superscript 2 denotes the fitting parameters of QD2019.

As the QD GS transition energy is close to the excitation laser energy at low temperature, we observed that the 1_{SAT} coefficient is slowly decreasing with temperature for both QD2015 and QD2019 samples, while the 2PA coefficient is enhanced rapidly when the temperature drops since the first transition virtual state is approaching the QD GS. The saturation intensity is an important parameter for describing the QDSC in a realistic model of the intermediate band solar cell. It indicates the light intensity that is required to excite half of the QD ground state with electrons, it can be expressed as:

$$I_s = \frac{4\pi^2 n^2 hc}{(T/T_1)\lambda^3}\Delta\nu \qquad 4.19$$

where $\Delta\nu$ is the FWHM of the homogeneous absorption profile and is given by $\Delta\nu = 1/\pi T_2$, where T_2 is the dephasing time, T_1 is the radiative lifetime, and T is the

quantum dot lifetime. Table 6 lists the temperature dependent quantum dot lifetime measured by Heitz, et al in 1999, the radiative lifetime measured by Harbord, et al in 2009 and the dephasing time data by Bayer, et al in 2002 [86-88], and the extracted dephasing time from our measured temperature dependent saturation intensities. We used the data from the references to extract the dephasing time at low temperature in QD2015 and QD2019 samples. It turns out the extracted dephasing times are decreasing with an increase of temperature, which is consistent with the decreasing trend in Bayer's measurement. However, the extracted T_2 values of QD2015 are ~ 3 times less than the T_2 data from Bayer's measurement in 2002 at each temperature region, while the extracted T_2 values of QD2019 are closer to the reference data at lower temperature. We assume it may due to the relatively smaller radiative lifetime in our quantum dot system since it's sandwiched between p-type GaAs and n-type GaAs, which provide effective charge extraction paths, as well as the different quantum dot densities compared with the self-assembled quantum dot sample that Bayer measured in 2002. The smaller quantum dot saturation intensity of QD2019 as compared to QD2015 at lower temperature region might indicate the enhanced role of surface state in the QD2015 sample as it ages, we believe that the freshly made QD sample has relatively longer QD lifetime as represented by T.

TABLE VI
EXTRACTED DEPHASING TIME

Temp (K)	T (s) (Ref 86)	T_1 (s) (Ref 87)	T_2 (s) (Ref 88)	T_2^1 (Extracted, s)	T_2^2 (Extracted, s)
170	1.58E-9	2.08E-9	1E-12	3.94E-13	8.87E-13
180	1.55E-9	2.15E-9	9E-13	2.72E-13	5.27E-13
200	1.44E-9	2.30E-9	6E-13	1.21E-13	2.36E-13
220	1.22E-9	2.65E-9	4E-13	1.16E-13	1.7E-13
250	7.46E-10	3.00E-9	3.2E-13	1.11E-13	1.15E-13
293	2.92E-10	3.10E-9	2E-13	1.09E-13	9.36E-14

Superscript 1 denotes the fitting parameters of QD2015, superscript 2 denotes the fitting parameters of QD2019.

In our previous report, we measured high Is at room temperature and evaluated the percentage of the photocurrent generated through the intermediate state compared to the VB to CB photocurrent to be 8 x 10^{-7}%, which is negligible and will not improve the efficiency of IBSC in a significant way [71]. We suggested that by going to cryogenic temperatures, one could reduce the Is of both transitions involved with the intermediate state. In this work, we demonstrate that I_s is appreciably reduced when the temperature is decreased. However, I_s is still as high as 3810 W/cm^2 at 170K, which is 38100 times larger than the unfocused sun intensity and 0.828 times the maximum concentrated sun intensity. This means that under one sun illumination at 170K, only around 1.05×10^{-4} $(= 4\text{x}0.1/3810)$ of the QD population is excited over a bandwidth corresponding to the inhomogeneous absorption line-width (we have previously observed a 4 times larger inhomogeneous line-width of the QD GS transition than the homogeneous line-width [65]). By assuming a similar saturation intensity for the second transition from the QD GS to the CB, and a similar inhomogeneous broadening coefficient, only 1.1×10^{-8} $(=(1.05 \times 10^{-4})^2)$ of the

QD population can be excited to the final CB, which is still negligible for improving the solar cell efficiency. From current results, we believe that the saturation intensity can be further reduced by reducing the temperature all the way down to liquid helium temperatures. I am planning to replace the 1064nm excitation laser source to 1015 nm laser to scan the lower temperature range with the same on-resonance z-scan set-up.

4.3.4 Thermal Effect in On-resonance Z-scan Measurement

Thermal effect of this quantum dot system under high-intensity excitation is observed at room temperature. The measured photocurrent responses cannot be explained by our established physical model. Figure 4.14 (a) shows the photocurrent response using a continuous wave (CW) laser source exciting the QD sample at room temperature (R.T.). The abnormal two-step broadening waveforms are observed when exciting the sample at high intensity (>45 mW), this kind of curve cannot be fitted with our physical model. We assume that the high laser intensity appreciably increases the temperature of the the quantum dot, introducing more fluctuation in the quantum dot sizes and more electron-phonon scattering, affecting the quantum dot absorption rate consequently. Modulating the laser with short pulses can appreciably reduce the thermal effect, Figure 4.14 (b) presents the photocurrent responses of QD sample excited by a 0.1% duty cycle (DC) pulsed laser source at R.T. No abnormal two-step broadening waveform is detected at high excitation intensity, and these photocurrent curves can be fitted with our 1_{SAT} and 2_{PA} physical model.

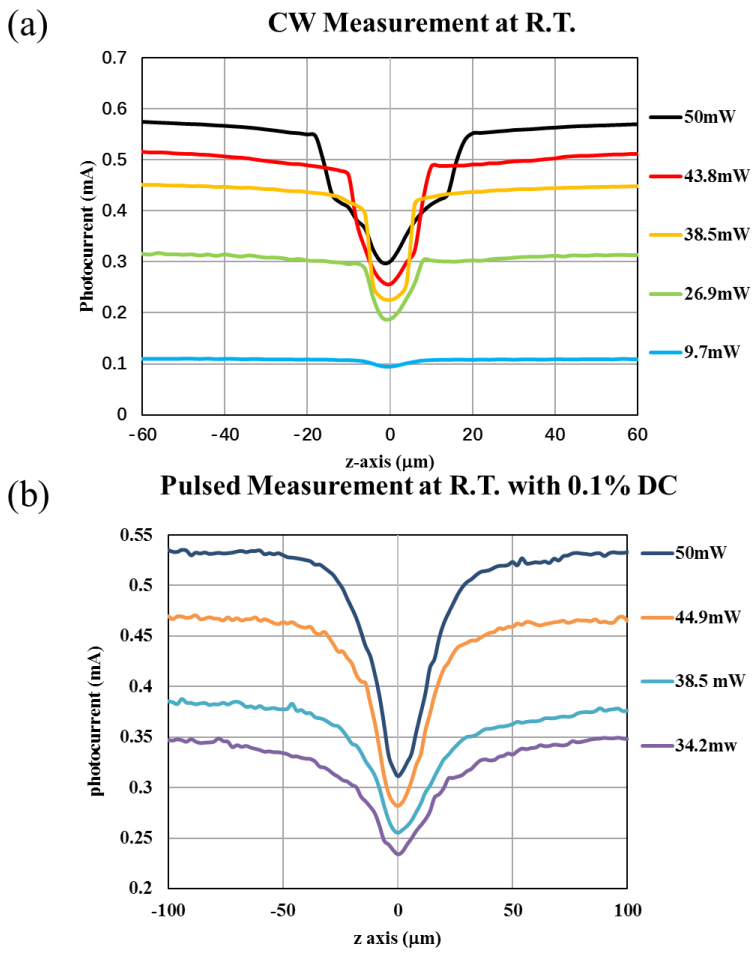

Figure 4.14 On-resonance z-scan photocurrent responses of quantum dot solar cell sample with (a) the continuous wave laser and (b) the 0.1% duty cycle pulsed laser at room temperature.

When the sample temperature is cooled down to cryogenic temperatures, the localized thermal effect in the QD region cannot be ignored in the low temperature z-scan measurement since the laser beam is focused to a small spot size (2 μm diameter) on the QD sample and since the specific heat of the sample also goes down. Even though the on-resonance laser source is modulated with 0.01% duty cycle pulses, the

thermal effect exists when varying the laser pulse width. To investigate the thermal effect in pulsed laser mode, I've fixed the laser power at 13.7 mW to avoid the potential thermal effect induced by high intensity excitation, and measured the photocurrent responses from R.T. to 170K with 75ns and 150ns excitation pulses. The extracted fitting parameters are listed in Table 7. Compared with the 1_{SAT} and 2PA parameters, they are close at each temperature range for 75ns and 150ns pulse measurements. The extracted saturation intensities are almost the same for both case above 220K, while the saturation intensities extracted from 75ns pulse measurement is about 0.8 times as that of 150ns pulse measurement when temperature is below 200K, which indicates that this on-resonance measurement is more sensitive to thermal effects at cryogenic temperatures, even the longer excitation pulses can introduce some measurable thermal effects. I must mention here I cannot apply shorter excitation pulses in this measurement to prove that the 75ns pulse measurement is free of thermal effect at cryogenic temperature, since the rise time of the quantum dot solar cell is about 50ns. Therefore in the future measurement at 8K with 1015nm laser, the main challenge will be to minimize thermal effects with limited excitation pulse width and duty cycle.

TABLE VII
FITTING PARAMETERS FOR THE 75NS AND 150NS PULSE EXCITATION MEASUREMENT

Temp (K)	a (75ns) (A/W)	b (75ns) ($A*cm^2/W^2$)	I_s (75ns) (mW/m^2)	a (150ns) (A/W)	b (150ns) ($A*cm^2/W^2$)	I_s (150ns) (mW/m^2)
170	3.88E-6	5.13E-7	0.0381	3.70E-06	7.50E-07	0.0500
180	4.45E-6	6.02E-7	0.0675	4.20E-06	8.00E-07	0.0800
200	5.80E-6	5.94E-7	0.174	5.10E-06	4.00E-07	0.220
220	6.30E-5	6.02E-7	0.330	5.70E-06	5.50E-07	0.330
250	6.50E-5	4.54E-7	0.901	6.00E-06	4.50E-07	0.900
293	6.66E-5	1.05E-7	2.905	6.52E-06	1.00E-07	3.000

4.4 Chapter Summary

In this chapter, I introduced the concept of the Intermediate band solar cell. The main physics of this concept is utilizing the intermediate band to absorb below-bandgap photons, generating extra photocurrent without sacrificing the open circuit voltage. The practical implementation of this concept is by using a quantum dot solar cell. I showed the basic fabrication procedure for implementing bulk GaAs solar cells. And then I demonstrated two main previous findings on our InAs/GaAs quantum dot solar cell. One is the existence of an extended Urbach tail into the quantum dot energy state region, and the derivation of this tail energy from the below-bandgap external quantum efficiency measurement. Another finding is the ultrahigh quantum dot saturation intensity at room temperature extracted from the non-linear photocurrent responses of on-resonance z-scan measurement, which results in extremely small transition rates between the inter-band states. By cooling down to cryogenic temperatures, the saturation intensities of both transitions involved with the intermediate state can be effectively reduced.

In this project, my work is to update the on-resonance z-scan measurement system with a closed-cycle liquid helium cryocooler system and measure the quantum dot saturation intensities at cryogenic temperatures. The assembly of the cryocooler system is described, and the operation procedure is demonstrated. I measured the photoluminescence of the InAs/GaAs QDSC to extract the quantum dot energy spectra at various temperatures from room temperature to 8K. I have modified the on-resonance z-scan measurement system with the cryocooler to investigate the optical saturation of the on-resonance first photon transition to the intermediate band in

InAs/GaAs QDs. The established physical model involved with background 2PA process and saturated 1PA process can still explain the photocurrent generation in the on-resonance experiments at low temperatures. We derived the QD saturation intensities from room temperature to 170K, and observed a saturation intensity 76 times smaller at 170K as compared to room temperature. The significant decrease of the saturation intensity is still impractically higher than one-sun intensity. The photocurrent generated from the QD ground state to the conduction band under one-sun illumination is negligible and will not improve the solar cell conversion efficiency. The thermal effect in this on-resonance measurement at cryogenic temperature range is investigated. Much smaller saturation intensity is expected to be observed when cooling to 8K with a 1015nm pulsed-laser excitation.

Chapter 5 Dissertation Summary

In the perovskite solar cell project, we have studied the material properties, solar cell structures and fabrication techniques for realizing perovskite solar cells and we have reviewed some state-of-art perovskite solar cells. We have proposed the sequential doping method to fabricate PTAA based perovskite solar cell with simple inverted planar structure without any complicated surface passivation techniques. Compared with conventional PEDOT:PSS, PTAA increases the electron-hole quasi-Fermi separation so that the open circuit voltage is remarkably improved. The sequential method provides an easier and more stable way to dope PTAA with F4-TCNQ in an orthogonal solvent base. The PTAA doping level is tunable with the doping solution concentration. It changes the PTAA film's sheet resistance and improves the solar cell's performance as a consequence. We have modified the inter-diffusion method for realizing perovskite thin film growth in a controllable solvent-assisted-annealing set-up. We can grow high quality perovskite crystals with grain sizes over 2 μm and thicknesses around 450 nm. The highest power conversion efficiency of 15.3% is obtained under AM1.5 irradiation. The measured photocurrent is consistent with the integrated photocurrent from the measured EQE data.

We have also considered the potential of realizing perovskite tandem solar cell. Currently people have successfully demonstrated high efficiency monolithic perovskite/Si tandem cell based on mixed-cation perovskite material. Our group has the capability to fabricate high efficiency CIGS solar cell and perovskite solar cell. We

proposed to implement both mechanically stacked and monolithic Perovskite/CIS tandem solar cells. Other application of perovskite material such as perovskite-based laser cavity was also investigated. Photoluminescence (PL) measurement of the perovskite thin film was performed and shows a strong spontaneous emission peak around 780 nm. We have also proposed the realization of a Fabry-Perot perovskite laser comprising of a gain medium of perovskite layer and a protecting layer of PMMA and a spacing layer of SiO_2 between a high reflectivity dielectric mirror and a silver metal mirror. A pulsed laser optical pumping configuration was used to minimize thermal effect in the gain material. Currently we did not observe the laser effect due to the insufficient optical gain inside the cavity. Pumping the cavity at cryogenic temperature may significantly enhance the photoluminescence and we may potentially observe the excitation peaks and lasing with the current cavity structure.

In the project of InAs/GaAs quantum dot solar cell, we introduced the concept of the intermediate band solar cell and the practical implementation as InAs/GaAs quantum dot solar cell. The main physics behind this concept utilizes the intermediate band to absorb below-bandgap photons, generating extra photocurrent without sacrificing the open circuit voltage. We previous discovered the existence of the extended Urbach tail into the quantum dot energy state region, and the ultrahigh quantum dot saturation intensity at room temperature, which explains the difficulty of implementing the IBSC concept in this quantum dot system at room temperature. By cooling down to cryogenic temperatures, the saturation intensities of both transitions involved with the intermediate state can be effectively reduced. In this case, we have modified the on-resonance z-scan measurement system that we previously used by adding a closed-

cycle liquid helium cryocooler system and we have measured the quantum dot saturation intensities at cryogenic temperatures. We have also measured the photoluminescence of the InAs/GaAs QDSC to extract the quantum dots energy spectra at various temperatures from room temperature to 8K. We have investigated the optical saturation of the on-resonance first photon transition to the intermediate band in InAs/GaAs QDs. The established physical model involved with a background 2PA process and a saturated 1PA process can still explain the photocurrent generation in the on-resonance experiments at low temperatures. We have derived the QD saturation intensities from room temperature to 170K, and have observed a decrease by a factor of 76 time of the saturation intensity at 170K. The significantly decreased saturation intensity is still impractically higher than the maximum concentrated sun intensity. The photocurrent generated from the QD ground state to the conduction band under one sun illumination is negligible and will not improve the solar cell conversion efficiency. We expected to observe much smaller saturation intensity when cooling down to 8K with a 1015 nm laser excitation.

Chapter 6 Appendices

A. The Assembly Procedure for the CoolPac System

The CoolPac is designed to provide a closed loop water: air cooling system for the ARS-4HW compressor. A pump in the CoolPac sends cooled water to the compressor through an external water line where it is circulated through the compressor, removing the heat. The heated water is returned to the CoolPac through another external water line and then enters the cooling coils. Heat is removed from the water as ambient air is forced through the cooling coils by an electric fan. The cooled water leaves the cooling coils, enters the pump inlet, and the process continues. An internal water reservoir is provided to collect any overflow water via a relief valve when the system warms up, and to return that water via a check valve when the system cools down.

Below I will provide the detail assembly procedure for the CoolPac system:

1. Unpack the equipment and inspect it for shipping damage
2. Position the CoolPac on the floor in the service corridor, near lab. Use a 50 feet long extended cable (FLEXTREME 10/3 Bulk Cable 50feet- SJOOW jacket, 30Amp, 300V,3 Wire) to connect with the compressor.
3. Connect a 3/8 in (9.53 mm) O.D. water tube from the water “Out” connection on the CoolPac to the water “In” connection on the compressor. Connect a 3/8 in (9.53 mm) O.D. water tube from the water “Out” connection on the compressor to the water “In” connection on the CoolPac. Since the CoolPac is in the service

corridor, make sure the water tube is long enough, suggested 50 feet long for each tube.

4. Disconnect the tube at the water “In” port on the CoolPac and connect a temporary tube about 6 ft (~ 2 m) long to this “In” port.

5. Make sure the CoolPac power cord is not plugged in. Remove the top cover from the CoolPac.

6. Regarding the algae inhibitor, prepare 4-gallon 50/50 propylene glycol mixed water.

7. See Figure 6.1. Remove the snap-fit cap from the reservoir. Use a funnel to carefully fill the reservoir ½ to ¾ full of mixed water. Replace the cap on the reservoir. Then close the shutoff valve in the tubing run from the reservoir to the pump.

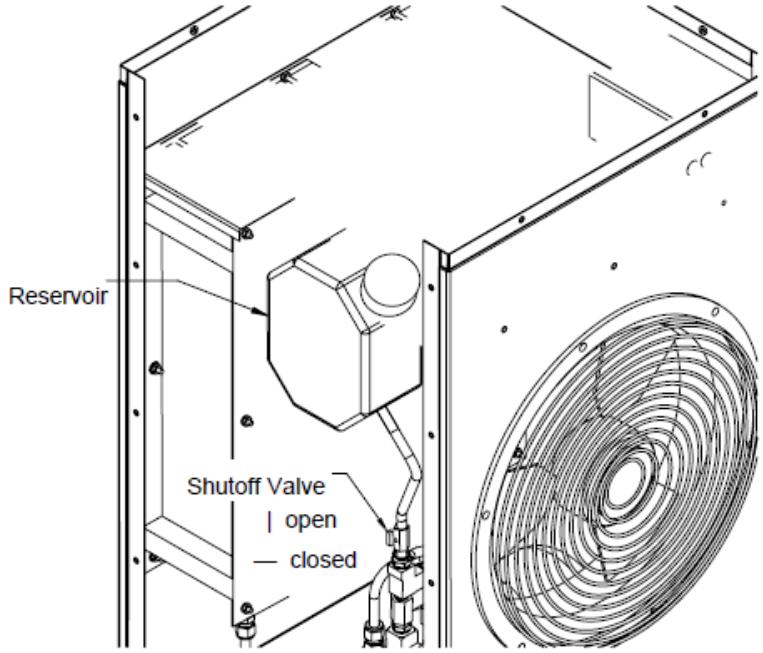

Figure 6.1 Inside look of the CoolPac

8. Fill a clean, 5-gallon bucket at least 1/2 full of mixed water. Elevate bucket (not on top of compressor or CoolPac) so the water level is above the CoolPac reservoir. See Figure 6.2. Put the free end of a temporary CoolPac "In" tube under the water in the bucket and hold the compressor "Out" tube over the surface of the water.

9. Install the CoolPac top cover, without screws at this time. Plug the CoolPac power cord into an electrical outlet. Do not plug in the compressor power cord into either the CoolPac or any other electrical outlet at this time.

10. Turn on the CoolPac. The compressor should not be running at this time. Water will be drawn into the CoolPac "In" port and air in the CoolPac and compressor will be expelled into the bucket from the compressor "Out" tube.

11. A steady stream of water coming out the compressor “Out” tube indicates all the air has been purged from the system. After the air is purged, put the open end of the compressor “Out” tube under the water in the bucket and continue to run the CoolPac for an additional few minutes.

12. If either tube comes out of the water during the final circulation period, repeat this filling procedure.

13. Turn off the CoolPac with the tubes still under water. Seal off the end of the compressor “Out” tube by placing the finger over the open end while keeping it under water. Disconnect the temporary hose from the CoolPac “In” port. Quickly connect the compressor “Out” tube to the CoolPac “In” port minimizing the loss of water from the system.

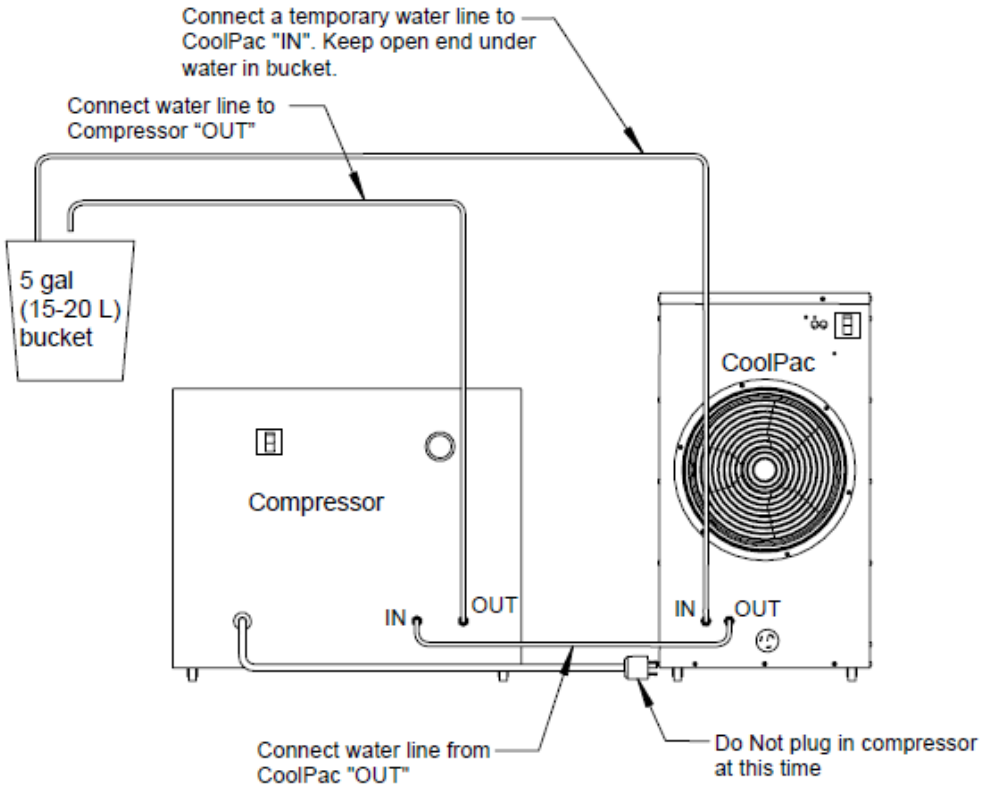

Figure 6.2 The illustration of adding cooling water into the CoolPac-Compressor dual system

14. Unplug the CoolPac from the electrical power.

15. Remove the top cover and check the level of the water in the reservoir. It should be about ½ to ¾ full of clean tap water. Open the shutoff valve between the reservoir and the pump.

16. Install the top cover with screws.

17. Make sure the CoolPac on-off switch is in the "OFF" position.

18. Plug the compressor power cord into the receptacle on the front of the CoolPac. Re-plug the CoolPac power cord into its electrical outlet.

19. Switch the compressor to “ON”. It will not start until the CoolPac is turned on. The compressor and CoolPac are now interlocked for operational safety.

B. Hot-point Probe Method

Our InAs/GaAs quantum dot solar cell sample is grown on an n-type doped GaAs wafer, and has a structure as shown in Figure 6.3. The wafer has a n-type doped backside and p-type doped front side. During our solar cell fabrication procedure, the first thing is to determine the backside of the wafer, i.e. the n-type doped side. There’s a simple way to distinguish the n-type and p-type semiconductor wafer by simply using a soldering iron and a multimeter, which is called the hot-point probe method.

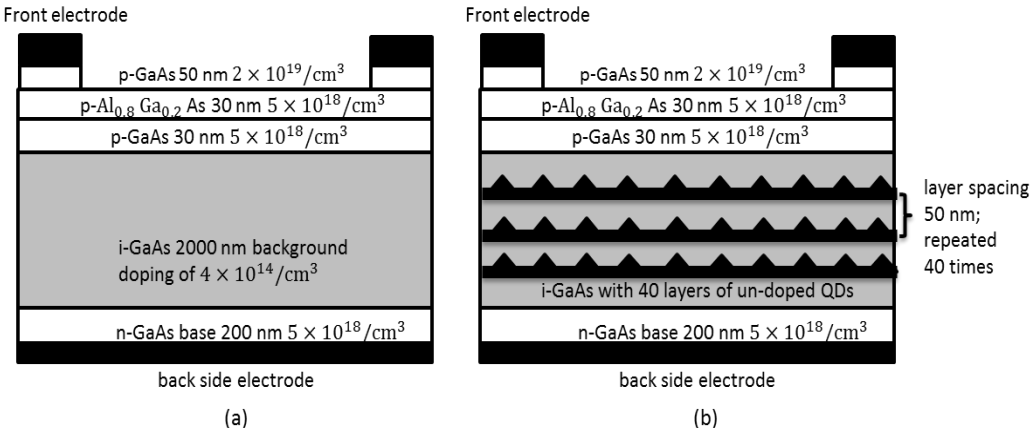

Figure 6.3 (a) Bulk GaAs solar cell structure diagram and (b) the InAs/GaAs quantum dots solar cell structure diagram.

This simple experiment is performed by contacting the wafer with a "hot" probe and a "cold" probe, and both probes are wired to a sensitive current meter. In our case, the “hot” probe is connected to the positive terminal of the meter while heated by a

soldering iron, and the “cold” probe is connected to the negative terminal. When applying the probes to n-type material one obtains a positive current reading on the meter, while the p-type material yields a negative current. The experimental set-up is shown in the figure below.

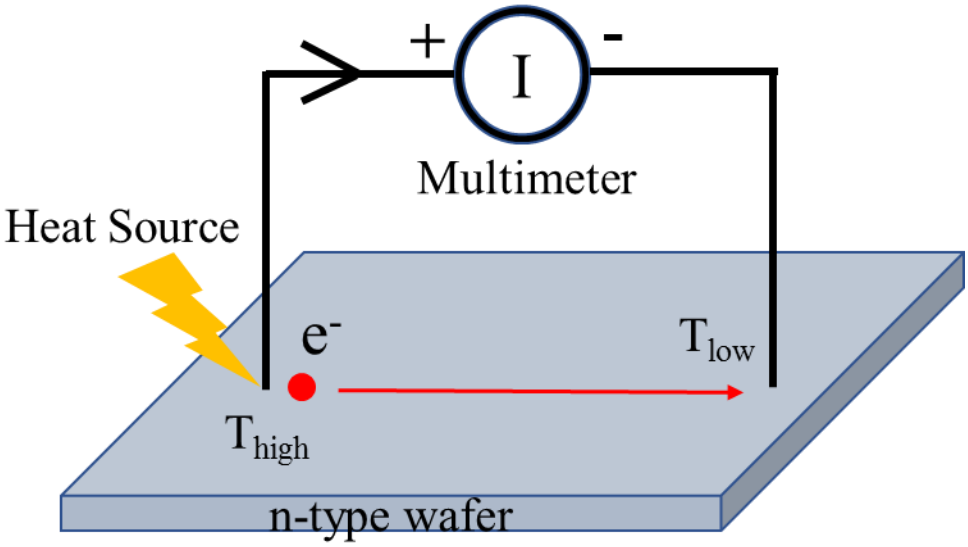

Figure 6.4 Experimental set-up of the "hot-probe" experiment.

If we try to explain it with a drift mechanism, the carriers within the semiconductor will move from the hot probe to the cold probe due to the build-in electrical potential. The band diagram in Figure 6. 5 shows a linear change of conduction band energy caused by the temperature variation. The effective density of states decreases with the temperature, results in a decrease of the conduction band energy at the low temperature end. This build-in electrical field will drift the electrons from the high temperature end to the low temperature end, and vice versa for the holes.

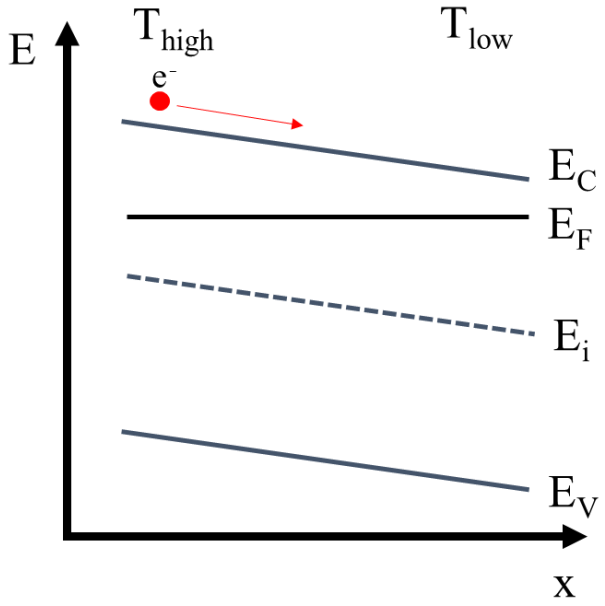

Figure 6.5 Energy band diagram corresponding to the "hot-probe" experiment

It may be more straightforward to understand it by the carrier diffusion mechanism. The heat source will cause the charge carriers (electrons in n-type semiconductor, and holes in p-type) to move away from the hot end. The heat from the hot probe creates an increased number of higher energy carriers that then diffuse from the contact point. Thus the multimeter will read a positive current or a voltage for an n-type wafer, and a negative reading for a p-type wafer.

This simple hot-point probe method is very effective to distinguish our quantum dot wafer, since the doping level is as high as $5x10^{18}/cm^3$ at both n-type side and p-type side, we can easily determine the doping type by reading the sign of voltage/current on the multimeter.

C. Simulation of Perovskite Laser Cavity

The design of a laser is not complicated, the key concepts are gain medium, pumping source and optical cavity. Ideally, a laser consists of a gain medium within an optical cavity. The gain medium will be energized by some other source optically or electrically to produce light, this process is called pumping. To enable stimulated emission by the gain medium, this requires a positive optical feedback mechanism. Typically the positive feedback is provided by the optical cavity, which is usually build of two mirrors between the gain medium. The light then bounces between the mirrors and pass through the gain medium, it will be amplified by stimulated emission. Based on the design of the optical cavity, a specific wavelength of the light is selected to escape the cavity and emitted as the laser light. Most practical lasers contain additional elements that affect the properties of the emitted light, such as the polarization, wavelength, and shape of the beam.

From the basic laser principles introduced above, the gain medium selection and optical cavity design are the main factors for realizing a good laser device. In our previous work on perovskite solar cell, the remarkable performance of solar cells can be attributed to the high absorption coefficient, the large carrier mobility, the long carrier lifetime and the low non-radiative recombination rate of the perovskite material. These physical properties are also ideal for the realization of an optically pumped laser. The low temperature solution-processed growth method for realizing good quality perovskite materials will dramatically lower the overall cost of laser fabrication. The tunable bandgap of perovskite materials allows the realization of a tunable laser. Recently, the perovskite materials have been used to demonstrate a relatively low laser

threshold by using an optical pumping [89-91] and have been used to realize efficient light-emitting diode [92].This raises the hope of soon being able to produce a solution-processed tunable diode laser. Based on our experience of growing high-quality perovskite materials, we are working at the realization of quasi-CW optically pumped perovskite-based lasers.

As mentioned at the very beginning, once an appropriate gain medium is selected, it is critical to properly design the optical cavity of the laser. The light with a specific wavelength will bounce, will be amplified and will eventually escape the cavity as a laser beam. The lasing wavelength is directly determined by the optical cavity. In our work, we are using a high reflecting multi-layer dielectric mirror and a parallel plate silver mirror to form a high finesse optical cavity. It follows the rules of the Fabry-Perot interferometer to select the resonance frequency or wavelength of the laser light.

Most Fabry-Perot interferometers are made of two identical dielectric mirrors. The symmetric Fabry-Perot interferometers will provide a high finesse and 100% transmission at specific wavelengths if the cavity losses can be neglected. Figure 6.6. shows a schematic drawing of an asymmetric Fabry-Perot interferometer, with mirror reflectivity R1 and R2, and a cavity spacing of d.

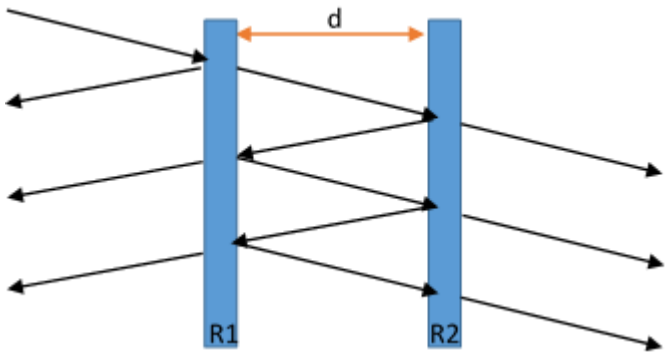

Figure 6.6 Schematic drawing of an asymmetric Fabry-Perot interferometer

For dielectric mirrors made of lossless materials, the intensity reflection coefficients and transmission coefficients can be written [75]

$$T_{FP} = \frac{(1-R_1)(1-R_2)}{(1-\sqrt{R_1R_2})^2 + 4\sqrt{R_1R_2}\sin^2(\phi)} \tag{6.1}$$

$$R_{FP} = \frac{(\sqrt{R_1}-\sqrt{R_2})^2 + 4\sqrt{R_1R_2}\sin^2(\phi)}{(1-\sqrt{R_1R_2})^2 + 4\sqrt{R_1R_2}\sin^2(\phi)} \tag{6.2}$$

where R1 and R2 are the mirror reflectivity, and the phase Φ is given by

$$2\Phi = \delta + \rho_1 + \rho_2 \tag{6.3}$$

$$\delta = \frac{4\pi nd}{\lambda} = 2kd \tag{6.4}$$

Here, ρ1 and ρ2 are the phase shift of the reflections from mirror 1 and 2, δ is the physical round-trip propagation phase shift inside the cavity. It is noticed that for lossless medium and mirrors, it can be easily shown that

$$T_{Fp} + R_{FP} = 1 \tag{6.5}$$

It turns out that for our application of perovskite laser, we have to consider the absorption in Fabry-Perot cavity due to the scattering loss in the cavity or due to the

mirror and material absorption in the mirror, and the gain medium between the mirrors which has high absorption coefficient at the desired wavelength region. Once the pumping power is above the threshold, stimulated emission will dominate, the gain in the medium will overcome the loss, and the amplified light will escape the cavity and form the laser light.

If we consider the gain coefficient as g and attenuation coefficient as α, the modified intensity transmission and reflection coefficients should be written as

$$T_{FP} = \frac{(1-R_1)(1-R_2)e^{-\alpha L_1 + gL_2}}{(1-\sqrt{R_1R_2}e^{-\alpha L_1 + gL_2})^2 + 4\sqrt{R_1R_2}e^{-\alpha L_1 + gL_2}\sin^2(\phi)} \quad 6.6$$

$$R_{FP} = \frac{(\sqrt{R_1} - \sqrt{R_2}e^{-\alpha L_1 + gL_2})^2 + 4\sqrt{R_1R_2}e^{-\alpha L_1 + gL_2}\sin^2(\phi)}{(1-\sqrt{R_1R_2}e^{-\alpha L_1 + gL_2})^2 + 4\sqrt{R_1R_2}e^{-\alpha L_1 + gL_2}\sin^2(\phi)} \quad 6.7$$

where L_1 is the length of the medium in which the intensity attenuation is present, L2 is the length of the gain medium.

In our proposed design, an optically pumped Fabry-Perot cavity is made up with the gain layer of the perovskite material, a spacing layer of PMMA and SiO_2 between a multi-layer dielectric mirror and the Ag metal mirror. From equation 6.6 and 6.7, we notice that the T_{FP} is a periodic function of Φ, which is a linear function of the wavenumber k (see equation 6.3 and 6.4). We built a simulation model based on the material's dispersive information and the equation 6.3 to equation 6.7 to predict the resonance peak of the Fabry-Perot cavity. The cavity consists of the perovskite film as the gain layer and PMMA and SiO_2 as the spacing layer. The wavelength dependent refractive indices and absorption coefficients of each layers are included in the simulation. For the two mirrors, the wavelength dependent reflective coefficients and

the phase shift of the Ag metal mirror and the light penetration depth of the multi-layer dielectric mirror are also taken into account [93]. To sum up all these information, we can locate the resonance peak of the Fabry-Perot cavity provided the thicknesses of perovskite, PMMA and SiO_2 layers are given.

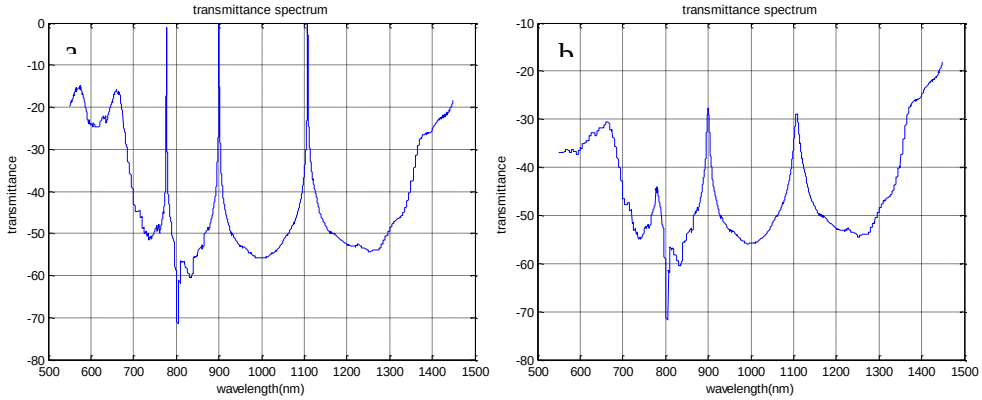

Figure 6.7 (a) Lossless and (b) lossy transmission spectrum of a Fabry-Perot cavity with 460 nm perovskite, 200 nm PMMA and 500 nm SiO_2

Figure 6.7 (a) shows the lossless transmission spectrum of a Fabry-Perot cavity with a 460 nm perovskite layer and a 200 nm PMMA and 500 nm SiO_2. The sharp resonance peaks are located at 777 nm, 900 nm and 1108 nm, and only the 777 nm peak falls into the photoluminescence region of the perovskite material $CH_3NH_3PbI_3$. Figure 6.7 (b) presents the lossy transmission spectrum of the same Fabry-Perot cavity. We can clearly see that the resonance peaks remain at the same position as the lossless case except for the dramatic reduction of its amplitude and the associated line-width broadening. The peak at 777 nm is greatly damped and broadened due to the large absorption coefficient of perovskite layer, i.e. high cavity loss. As the pumping power

is increased, the light emission will be dominated by the stimulated emission and the gain in the cavity will increase to compensate the loss and will lead to a sharp transmission peak again. We have introduced a Gaussian distributed gain coefficient which is correlated with the PL spectrum of the perovskite material (peak at 777 nm, FWHM as 50 nm) in the simulation model to account for the loss. Figure 6.8 (b) shows the transmission spectrum of a lossy Fabry-Perot cavity below and at threshold. The transmission peak at 777 nm is 0 dB loss with very narrow line-width as the gain increases to the threshold level, while the other two transmission peaks at 900 nm and 1108 nm remain the same since there's no gain at their wavelengths. These modified simulation results indicate that the transmitted laser light intensity will increase significantly and its line-width will be narrowed once the gain is close to or above the threshold.

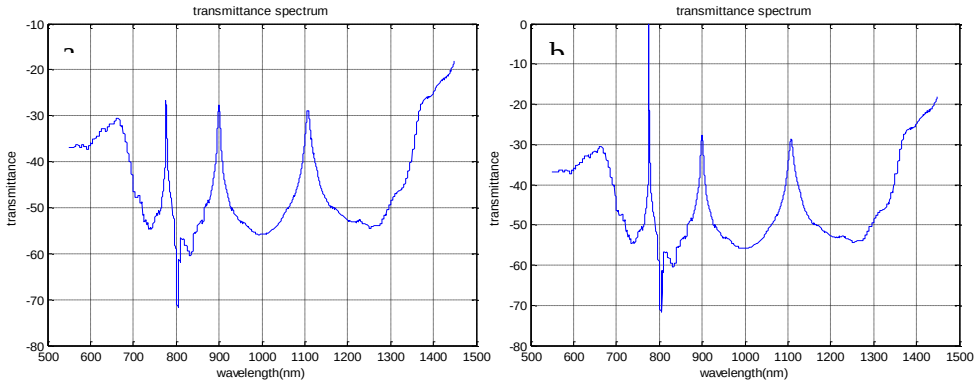

Figure 6.8 Transmission spectrum of the Fabry-Perot cavity when (a) below gain threshold and (b) at gain threshold

Bibliography

[1] *A. Kojima, K. Teshima, Y. Shirai and T. Miyasaka, "Organometal Halide Perovskites as Visible-Light Sensitizers for Photovoltaic Cells", Journal of the American Chemical Society, vol. 131, no. 17, pp. 6050-6051, 2009.*

[2] *NREL.gov, 2019. [Online]. Available:https://www.nrel.gov/pv/assets/pdfs/best-reserch-cell-efficiencies.20190327.pdf [Accessed: 11- Jan- 2019].*

[3] *Y. Sun, J. Peng, Y. Chen, Y. Yao and Z. Liang, "Triple-cation mixed-halide perovskites: towards efficient, annealing-free and air-stable solar cells enabled by Pb(SCN)2 additive", Scientific Reports, vol. 7, no. 1, 2017.*

[4] *G. Xing, N. Mathews, S. Sun, S. Lim, Y. Lam, M. Gratzel, S. Mhaisalkar and T. Sum, "Long-Range Balanced Electron- and Hole-Transport Lengths in Organic-Inorganic CH3NH3PbI3", Science, vol. 342, no. 6156, pp. 344-347, 2013.*

[5] *C. Motta, F. El-Mellouhi and S. Sanvito, "Charge carrier mobility in hybrid halide perovskites", Scientific Reports, vol. 5, no. 1, 2015.*

[6] *J. Noh, S. Im, J. Heo, T. Mandal and S. Seok, "Chemical Management for Colorful, Efficient, and Stable Inorganic–Organic Hybrid Nanostructured Solar Cells", Nano Letters, vol. 13, no. 4, pp. 1764-1769, 2013.*

[7] *N. K. Noel et al., "Lead-free organic–inorganic tin halide perovskites for photovoltaic applications," Energy Environ. Sci., vol. 7, no. 9, pp. 3061–3068, 2014.*

[8] *N. Jeon, J. Noh, Y. Kim, W. Yang, S. Ryu and S. Seok, "Solvent engineering for high-performance inorganic–organic hybrid perovskite solar cells", Nature Materials, vol. 13, no. 9, pp. 897-903, 2014.*

[9] *N. Jeon, J. Noh, W. Yang, Y. Kim, S. Ryu, J. Seo and S. Seok, "Compositional engineering of perovskite materials for high-performance solar cells", Nature, vol. 517, no. 7535, pp. 476-480, 2015.*

[10] *W. Yang, J. Noh, N. Jeon, Y. Kim, S. Ryu, J. Seo and S. Seok, "High-performance photovoltaic perovskite layers fabricated through intramolecular exchange", Science, vol. 348, no. 6240, pp. 1234-1237, 2015.*

[11] *W. Yang, B. Park, E. Jung, N. Jeon, Y. Kim, D. Lee, S. Shin, J. Seo, E. Kim, J. Noh and S. Seok, "Iodide management in formamidinium-lead-halide–based perovskite layers for efficient solar cells", Science, vol. 356, no. 6345, pp. 1376-1379, 2017.*

[12] *D. Luo, W. Yang, Z. Wang, A. Sadhanala, Q. Hu, R. Su, R. Shivanna, G. Trindade, J. Watts, Z. Xu, T. Liu, K. Chen, F. Ye, P. Wu, L. Zhao, J. Wu, Y. Tu, Y. Zhang, X. Yang, W. Zhang, R. Friend, Q. Gong, H. Snaith and R. Zhu, "Enhanced photovoltage for inverted planar heterojunction perovskite solar cells", Science, vol. 360, no. 6396, pp. 1442-1446, 2018.*

[13] *W. Chen, Y. Wu, Y. Yue, J. Liu, W. Zhang, X. Yang, H. Chen, E. Bi, I. Ashraful, M. Gratzel and L. Han, "Efficient and stable large-area perovskite solar cells with inorganic charge extraction layers", Science, vol. 350, no. 6263, pp. 944-948, 2015.*

[14] J. You, L. Meng, T. Song, T. Guo, Y. Yang, W. Chang, Z. Hong, H. Chen, H. Zhou, Q. Chen, Y. Liu, N. De Marco and Y. Yang, "Improved air stability of perovskite solar cells via solution-processed metal oxide transport layers", Nature Nanotechnology, vol. 11, no. 1, pp. 75-81, 2015.

[15] S. Ye, H. Rao, Z. Zhao, L. Zhang, H. Bao, W. Sun, Y. Li, F. Gu, J. Wang, Z. Liu, Z. Bian and C. Huang, "A Breakthrough Efficiency of 19.9% Obtained in Inverted Perovskite Solar Cells by Using an Efficient Trap State Passivator Cu(thiourea)I", Journal of the American Chemical Society, vol. 139, no. 22, pp. 7504-7512, 2017.

[16] J. Christians, R. Fung and P. Kamat, "An Inorganic Hole Conductor for Organo-Lead Halide Perovskite Solar Cells. Improved Hole Conductivity with Copper Iodide", Journal of the American Chemical Society, vol. 136, no. 2, pp. 758-764, 2013.

[17] W. Chen, Y. Zhou, L. Wang, Y. Wu, B. Tu, B. Yu, F. Liu, H. Tam, G. Wang, A. Djurišić, L. Huang and Z. He, "Molecule-Doped Nickel Oxide: Verified Charge Transfer and Planar Inverted Mixed Cation Perovskite Solar Cell", Advanced Materials, vol. 30, no. 20, p. 1800515, 2018.

[18] W. Chen, Y. Wu, J. Fan, A. Djurišić, F. Liu, H. Tam, A. Ng, C. Surya, W. Chan, D. Wang and Z. He, "Understanding the Doping Effect on NiO: Toward High-Performance Inverted Perovskite Solar Cells", Advanced Energy Materials, vol. 8, no. 19, p. 1703519, 2018.

[19] W. Chen, F. Liu, X. Feng, A. Djurišić, W. Chan and Z. He, "Cesium Doped NiOx as an Efficient Hole Extraction Layer for Inverted Planar Perovskite Solar Cells", 2019.

[20] J. Seo, S. Park, Y. Chan Kim, N. Jeon, J. Noh, S. Yoon and S. Seok, "Benefits of very thin PCBM and LiF layers for solution-processed p–i–n perovskite solar cells", Energy Environ. Sci., vol. 7, no. 8, pp. 2642-2646, 2014.

[21] W. Nie, H. Tsai, R. Asadpour, J. Blancon, A. Neukirch, G. Gupta, J. Crochet, M. Chhowalla, S. Tretiak, M. Alam, H. Wang and A. Mohite, "High-efficiency solution-processed perovskite solar cells with millimeter-scale grains", Science, vol. 347, no. 6221, pp. 522-525, 2015.

[22] J. You, Z. Hong, Y. Yang, Q. Chen, M. Cai, T. Song, C. Chen, S. Lu, Y. Liu, H. Zhou and Y. Yang, "Low-Temperature Solution-Processed Perovskite Solar Cells with High Efficiency and Flexibility", ACS Nano, vol. 8, no. 2, pp. 1674-1680, 2014.

[23] [9]S. Sun, T. Salim, N. Mathews, M. Duchamp, C. Boothroyd, G. Xing, T. Sum and Y. Lam, "The origin of high efficiency in low-temperature solution-processable bilayer organometal halide hybrid solar cells", Energy Environ. Sci., vol. 7, no. 1, pp. 399-407, 2014.

[24] P. Liang, C. Chueh, S. Williams and A. Jen, "Roles of Fullerene-Based Interlayers in Enhancing the Performance of Organometal Perovskite Thin-Film Solar Cells", Advanced Energy Materials, vol. 5, no. 10, p. 1402321, 2015.

[25] D. Zhao, M. Sexton, H. Park, G. Baure, J. Nino and F. So, "High-Efficiency Solution-Processed Planar Perovskite Solar Cells with a Polymer

Hole Transport Layer", Advanced Energy Materials, vol. 5, no. 6, p. n/a-n/a, 2015.

[26] O. Malinkiewicz, A. Yella, Y. Lee, G. Espallargas, M. Graetzel, M. Nazeeruddin and H. Bolink, "Perovskite solar cells employing organic charge-transport layers", Nature Photonics, vol. 8, no. 2, pp. 128-132, 2013.

[27] X. Xu, C. Ma, Y. Cheng, Y. Xie, X. Yi, B. Gautam, S. Chen, H. Li, C. Lee, F. So and S. Tsang, "Ultraviolet-ozone surface modification for non-wetting hole transport materials based inverted planar perovskite solar cells with efficiency exceeding 18%", Journal of Power Sources, vol. 360, pp. 157-165, 2017.

[28] C. Bi, Q. Wang, Y. Shao, Y. Yuan, Z. Xiao and J. Huang, "Non-wetting surface-driven high-aspect-ratio crystalline grain growth for efficient hybrid perovskite solar cells", Nature Communications, vol. 6, no. 1, 2015.

[29] Q. Wang, C. Bi and J. Huang, "Doped hole transport layer for efficiency enhancement in planar heterojunction organolead trihalide perovskite solar cells", Nano Energy, vol. 15, pp. 275-280, 2015.

[30] X. Zheng, B. Chen, J. Dai, Y. Fang, Y. Bai, Y. Lin, H. Wei, X. Zeng and J. Huang, "Defect passivation in hybrid perovskite solar cells using quaternary ammonium halide anions and cations", Nature Energy, vol. 2, no. 7, p. 17102, 2017.

[31] I. Jacobs, E. Aasen, J. Oliveira, T. Fonseca, J. Roehling, J. Li, G. Zhang, M. Augustine, M. Mascal and A. Moulé, "Comparison of solution-mixed and sequentially processed P3HT:F4TCNQ films: effect of doping-induced aggregation on film morphology", J. Mater. Chem. C, vol. 4, no. 16, pp. 3454-3466, 2016.

[32] Z. Xiao, C. Bi, Y. Shao, Q. Dong, Q. Wang, Y. Yuan, C. Wang, Y. Gao and J. Huang, "Efficient, high yield perovskite photovoltaic devices grown by interdiffusion of solution-processed precursor stacking layers", Energy Environ. Sci., vol. 7, no. 8, pp. 2619-2623, 2014.

[33] NREL.gov, 2019. [Online]. Available: https://www.nrel.gov/pv/assets/pdfs/pv-efficiency-chart.20190103.pdf. [Accessed: 17- April- 2019]

[34] W. Shockley and H. Queisser, "Detailed Balance Limit of Efficiency of p‐n Junction Solar Cells", Journal of Applied Physics, vol. 32, no. 3, pp. 510-519, 1961.

[35] A. Luque and A. Martí, "Increasing the Efficiency of Ideal Solar Cells by Photon Induced Transitions at Intermediate Levels", Physical Review Letters, vol. 78, no. 26, pp. 5014-5017, 1997.

[36] A. Luque and A. MartÃ, "The Intermediate Band Solar Cell: Progress Toward the Realization of an Attractive Concept", Advanced Materials, vol. 22, no. 2, pp. 160-174, 2010.

[37] A. Luque, A. Martí and C. Stanley, "Understanding intermediate-band solar cells", Nature Photonics, vol. 6, no. 3, pp. 146-152, 2012.

[38] Y. Okada, N. Ekins-Daukes, T. Kita, R. Tamaki, M. Yoshida, A. Pusch, O. Hess, C. Phillips, D. Farrell, K. Yoshida, N. Ahsan, Y. Shoji, T. Sogabe

and J. Guillemoles, "Intermediate band solar cells: Recent progress and future directions", Applied Physics Reviews, vol. 2, no. 2, p. 021302, 2015.

[39] K. Tanabe, D. Guimard, D. Bordel and Y. Arakawa, "High-efficiency InAs/GaAs quantum dot solar cells by metalorganic chemical vapor deposition", Applied Physics Letters, vol. 100, no. 19, p. 193905, 2012.

[40] A. Martí, E. Antolín, C. Stanley, C. Farmer, N. López, P. Díaz, E. Cánovas, P. Linares and A. Luque, "Production of Photocurrent due to Intermediate-to-Conduction-Band Transitions: A Demonstration of a Key Operating Principle of the Intermediate-Band Solar Cell", Physical Review Letters, vol. 97, no. 24, 2006.

[41] P. Gao, M. Grätzel, and M. K. Nazeeruddin, "Organohalide lead perovskites for photovoltaic applications," Energy Environ. Sci., Jun. 2014.

[42] B. Suarez, V. Gonzalez-Pedro, T. S. Ripolles, R. S. Sanchez, L. Otero, and I. Mora-Sero, "Recombination Study of Combined Halides (Cl, Br, I) Perovskite Solar Cells," J. Phys. Chem. Lett., vol. 5, no. 10, pp. 1628–1635, May 2014.

[43] J. H. Noh, S. H. Im, J. H. Heo, T. N. Mandal, and S. I. Seok, "Chemical Management for Colorful, Efficient, and Stable Inorganic–Organic Hybrid Nanostructured Solar Cells," Nano Lett., vol. 13, no. 4, pp. 1764–1769, Apr. 2013.

[44] T. Baikie, Y. Fang, J. M. Kadro, M. Schreyer, F. Wei, S. G. Mhaisalkar, M. Graetzel, and T. J. White, "Synthesis and crystal chemistry of the hybrid perovskite (CH3NH3)PbI3 for solid-state sensitised solar cell applications," J. Mater. Chem. A, vol. 1, no. 18, pp. 5628–5641, Apr. 2013.

[45] F. Deschler, M. Price, S. Pathak, L. E. Klintberg, D.-D. Jarausch, R. Higler, S. Hüttner, T. Leijtens, S. D. Stranks, H. J. Snaith, M. Atatüre, R. T. Phillips, and R. H. Friend, "High Photoluminescence Efficiency and Optically Pumped Lasing in Solution-Processed Mixed Halide Perovskite Semiconductors," J. Phys. Chem. Lett., vol. 5, no. 8, pp. 1421–1426, Apr. 2014.

[46] G. Xing, N. Mathews, S. Sun, S. S. Lim, Y. M. Lam, M. Grätzel, S. Mhaisalkar, and T. C. Sum, "Long-Range Balanced Electron- and Hole-Transport Lengths in Organic-Inorganic CH3NH3PbI3," Science, vol. 342, no. 6156, pp. 344–347, Oct. 2013.

[47] S. D. Stranks, G. E. Eperon, G. Grancini, C. Menelaou, M. J. P. Alcocer, T. Leijtens, L. M. Herz, A. Petrozza, and H. J. Snaith, "Electron-Hole Diffusion Lengths Exceeding 1 Micrometer in an Organometal Trihalide Perovskite Absorber," Science, vol. 342, no. 6156, pp. 341–344, Oct. 2013.

[48] V. Gonzalez-Pedro, E. J. Juarez-Perez, W.-S. Arsyad, E. M. Barea, F. Fabregat-Santiago, I. Mora-Sero, and J. Bisquert, "General Working Principles of CH3NH3PbX3 Perovskite Solar Cells," Nano Lett., vol. 14, no. 2, pp. 888–893, Feb. 2014.

[49] T. C. Sum and N. Mathews, "Advancements in perovskite solar cells: photophysics behind the photovoltaics," Energy Environ. Sci., Jun. 2014.

[50] S. De Wolf, J. Holovsky, S.-J. Moon, P. Löper, B. Niesen, M. Ledinsky, F.-J. Haug, J.-H. Yum, and C. Ballif, "Organometallic Halide Perovskites: Sharp Optical Absorption Edge and Its Relation to Photovoltaic Performance," J. Phys. Chem. Lett., vol. 5, no. 6, pp. 1035–1039, Mar. 2014.

[51] Y. Yao, W. Hsu, M. Dagenais "High Efficiency Perovskite Solar Cells by a Modified Low-Temperature Solution Process Inter-Diffusion Method", 44th IEEE Photovoltaic Specialist Conference, 2017.

[52] W. Yin, L. Pan, T. Yang and Y. Liang, "Recent Advances in Interface Engineering for Planar Heterojunction Perovskite Solar Cells", Molecules, vol. 21, no. 7, p. 837, 2016.

[53] Y. Yuan and J. Huang, "Ion Migration in Organometal Trihalide Perovskite and Its Impact on Photovoltaic Efficiency and Stability," Acc. Chem. Res., vol. 49, no. 2, pp. 286–293, Feb. 2016.

[54] K. Miyano, M. Yanagida, N. Tripathi, and Y. Shirai, "Hysteresis, Stability, and Ion Migration in Lead Halide Perovskite Photovoltaics," J. Phys. Chem. Lett., vol. 7, no. 12, pp. 2240–2245, Jun. 2016.

[55] J. Xu et al., "Perovskite-fullerene hybrid materials suppress hysteresis in planar diodes," Nat. Commun., vol. 6, p. 7081, May 2015

[56] Y.M. Yang, Q. Chen, Y.T. Hsieh, T.B. Song, N.D. Marco, H. Zhou, Y. Y ang, ACS Nano, 9 (2015), pp. 7714-7721

[57] L. Kranz, A. Abate, T. Feurer, F. Fu, E. Avancini, J. Löckinger, P. Rei nhard, S.M. Zakeeruddin, M. Grätzel, S. Buecheler, J. Phys. Chem. Lett., 6 (2017), pp. 2676-2681

[58] G.E. Eperon, T. Leijtens, K.A. Bush, R. Prasanna, T. Green, J.T.W. Wa ng, D.P. McMeekin, G. Volonakis, R.L. Milot, R. MayScience, 354 (2016), pp. 861-865

[59] Z. Yu, M. Leilaeioun, Z. Holman, Nat. Energy, 1 (2016), p. 16137

[60] M. Monteiro Lunardi, W.Y.H.B. Anita, J.P. Alvarez-Gaitan, S. Moore, R.Corkish, Prog. Photovolt. Res. Appl., 25 (2017), pp. 679-695

[61] Z. Qiu, Chen, B. Cao and H. Zhou, "Monolithic perovskite/Si tandem solar cells exceeding 22% efficiency via optimizing top cell absorber", Nano Energy, vol. 53, pp. 798-807, 2018.

[62] K. Bush, H. Snaith, and M. McGehee, "23.6%-efficient monolithic perovskite/silicon tandem solar cells with improved stability", Nature Energy, vol. 2, no. 4, 2017.

[63] F. Deschler et al., "High Photoluminescence Efficiency and Optically Pumped Lasing in Solution-Processed Mixed Halide Perovskite Semiconductors," J. Phys. Chem. Lett., vol. 5, no. 8, pp. 1421–1426, Apr. 2014

[64] J. T. Sullivan, C. B. Simmons, T. Buonassisi, and J. J. Krich, "Targeted Search for Effective Intermediate Band Solar Cell Materials," IEEE J. Photovolt., vol. 5, no. 1, pp. 212–218, Jan. 2015.

[65] T. Li and M. Dagenais, "Below-bandgap absorption in InAs/GaAs self-assembled quantum dot solar cells," Prog. Photovolt. Res. Appl., vol. 23, no. 8, pp. 997–1002, Aug. 2015.

[66] T. Li, R. E. Bartolo, and M. Dagenais, "Challenges to the concept of an intermediate band in InAs/GaAs quantum dot solar cells," Appl. Phys. Lett., vol. 103, no. 14, p. 141113, Sep. 2013.

[67] Urbach, F., 1953. The Long-Wavelength Edge of Photographic Sensitivity and of the Electronic Absorption of Solids. Phys. Rev. 92, 1324–1324. doi:10.1103/PhysRev.92.1324

[68] Pankove, J.I., 1975. Transitions between band tails, in: Optical Processes in Semiconductors. Dover, New York, pp. 43–46.

[69] Greeff, C.W., Glyde, H.R., 1995a. Anomalous Urbach tail in GaAs. Phys. Rev. B 51, 1778–1783. doi:10.1103/PhysRevB.51.1778

[70] Johnson, S.R., Tiedje, T., 1995. Temperature dependence of the Urbach edge in GaAs. J. Appl. Phys. 78, 5609–5613. doi:doi:10.1063/1.359683

[71] T. Li and M. Dagenais, "High saturation intensity in InAs/GaAs quantum dot solar cells and impact on the realization of the intermediate band concept at room-temperature," Appl. Phys. Lett., vol. 110, no. 6, p. 061107, Feb. 2017.

[72] M. Sheik-Bahae, A. A. Said, T. H. Wei, D. J. Hagan, and E. W. V. Stryland, "Sensitive measurement of optical nonlinearities using a single beam," IEEE J. Quantum Electron., vol. 26, no. 4, pp. 760–769, Apr. 1990.

[73] P. Borri et al., "Ultralong dephasing time in InGaAs quantum dots," Phys. Rev. Lett., vol. 87, no. 15, p. 157401, Oct. 2001.

[74] M. Bayer and A. Forchel, "Temperature dependence of the exciton homogeneous linewidth in In0.60Ga0.40As/GaAs self-assembled quantum dots," Phys. Rev. B, vol. 65, p. 041308, Jan. 2002.

[75] A. Yariv and P. Yeh, Photonics: Optical Electronics in Modern Communications, 6 edition. New York: Oxford University Press, 2006.

[76] T. Li and M. Dagenais, "Non-resonant below-bandgap two-photon absorption in quantum dot solar cells," Appl. Phys. Lett., vol. 106, no. 17, p. 171101, Apr. 2015

[77] E. Harbord, P. Spencer, E. Clarke, and R. Murray, "The influence of size distribution on the luminescence decay from excited states of InAs/GaAs self-assembled quantum dots," J. Appl. Phys., vol. 105, no. 3, p. 033507, Feb. 2009.

[78] C. Bardot, M. Schwab, M. Bayer, S. Fafard, Z. Wasilewski, and P. Hawrylak, "Exciton lifetime in InAs/GaAs quantum dot molecules," Phys. Rev. B, vol. 72, no. 3, Jul. 2005.

[79] Y. Okada et al., "Intermediate band solar cells: Recent progress and future directions," Appl. Phys. Rev., vol. 2, no. 2, p. 021302, Apr. 2015.

[80] D. G. Sellers, E. Y. Chen, S. J. Polly, S. M. Hubbard, and M. F. Doty, "Effect of doping on room temperature carrier escape mechanisms in InAs/GaAs quantum dot p-i-n junction photovoltaic cells," J. Appl. Phys., vol. 119, no. 19, p. 194301, May 2016.

[81] F. Kadlec, H. Nemec, and P. Kuzel, "Optical two-photon absorption in GaAs measured by optical pump-terahertz probe spectroscopy," in Infrared and Millimeter Waves, Conference Digest of the 2004 Joint 29th International Conference on 2004 and 12th International Conference on Terahertz Electronics, 2004., 2004, pp. 497–498.

[82] G. C. Valley, T. F. Boggess, J. Dubard, and A. L. Smirl, "Picosecond pump‐probe technique to measure deep‐level, free‐carrier, and two photon cross sections in GaAs," J. Appl. Phys., vol. 66, no. 6, pp. 2407–2413, Sep. 1989.

[83] S. Sauvage et al., "Saturation of intraband absorption and electron relaxation time in n-doped InAs/GaAs self-assembled quantum dots," Appl. Phys. Lett., vol. 73, no. 26, pp. 3818–3821, Dec. 1998.

[84] A. Tierno, T. Ackemann, C. G. Leburn, and C. T. A. Brown, "Saturation of absorption and gain in a quantum dot diode with continuous-wave driving," Appl. Phys. Lett., vol. 97, no. 23, p. 231104, Dec. 2010.

[85] Dai Y, Fan J, Chen Y, Lin R, Lee S and Lin H 1997 Temperature dependence of photoluminescence spectra in InAs/GaAs quantum dot superlattices with large thicknesses J. Appl. Phys. 82 4489–92

[86] R. Heitz, D. Bimberg, "Temperature dependent optical properties of self-organized InAs/GaAs quantum dots", Journal of Electronic Materials, vol. 28, no. 5, pp. 520-527, 1999.

[87] E. Harbord, P. Spencer, E. Clarke and R. Murray, "Radiative lifetimes in undoped and p-doped InAs/GaAs quantum dots", Physical Review B, vol. 80, no. 19, 2009.

[88] M. Bayer and A. Forchel, "Temperature dependence of the exciton homogeneous linewidth in $In_{0.60}Ga_{0.40}As$/GaAs self-assembled quantum dots", Physical Review B, vol. 65, no. 4, 2002.

[89] F. Deschler et al., "High Photoluminescence Efficiency and Optically Pumped Lasing in Solution-Processed Mixed Halide Perovskite Semiconductors," J. Phys. Chem. Lett., vol. 5, no. 8, pp. 1421–1426, Apr. 2014.

[90] H. Zhu et al., "Lead halide perovskite nanowire lasers with low lasing thresholds and high- quality factors," Nat. Mater., vol. 14, no. 6, pp. 636–642, Jun. 2015.

[91] Y. Jia, R. A. Kerner, A. J. Grede, A. N. Brigeman, B. P. Rand, and N. C. Giebink, "Diode-Pumped Organo-Lead Halide Perovskite Lasing in a Metal-Clad Distributed Feedback Resonator," Nano Lett., vol. 16, no. 7, pp. 4624–4629, Jul. 2016.

[92] H. Cho et al., "Overcoming the electroluminescence efficiency limitations of perovskite light-emitting diodes," Science, vol. 350, no. 6265, pp. 1222–1225, Dec. 2015.

[93] "RefractiveIndex.INFO - Refractive index database." [Online]. Available: https://refractiveindex.info/. [Accessed: 18-Jul-2017].